Novel inverse opal based nanostructures using atomic layer deposition for photoelectrochemical cell applications

Siva Krishna Karuturi

2012

Siva Krishna Karuturi. (2012). Novel inverse opal based nanostructures using atomic layer deposition for photoelectrochemical cell applications. Doctoral thesis, Nanyang Technological University, Singapore.

https://hdl.handle.net/10356/51033

https://doi.org/10.32657/10356/51033

NOVEL INVERSE OPAL BASED NANOSTRUCTURES USING ATOMIC LAYER DEPOSITION FOR PHOTOELECTROCHEMICAL CELL APPLICATIONS

A thesis submitted to the Nanyang Technological University in fulfillment of the requirement for the degree of Doctor of Philosophy in Engineering

Submitted by:

Siva Krishna Karuturi

Under the supervision of

Assoc. Prof. Alfred Tok Iing Yoong

School of Materials Science & Engineering
Nanyang Technological University

August 2012

NANYANG TECHNOLOGICAL UNIVERSITY

School of Materials Science & Engineering
Nanyang Technological University
Singapore

ACKNOWLEDGEMENT

PhD study was a long journey which I could not have finished without the support of a large number of unbelievable people. With great pleasure and great sense of satisfaction, I take this opportunity to express my sincere thanks to my supervisor Assoc. Prof. Alfred Tok Iing Yoong, for his invaluable guidance and constant encouragement at each and every step of my PhD research. I am very grateful to him for allowing me to explore the new areas of scientific research with autonomy and excitement.

My sincere thanks goes to Asst. Prof. Fan Hongjin and Dr. Su Liap Tat who have guided and trained me to make my PhD research a fruitful experience. I would like to thank my TAC members, Assoc. Prof. Lam Yen Ming and Assoc. Prof. Dong Zhili for their invaluable suggestions. I would like to express my gratitude to Asst. Prof. Zhao Yang, Assoc. Prof. Nazir P. Kherani, Dr. Lijun Liu, Dr. Derrick Fam and Dr. Chuan Wei for sharing their knowledge and guiding me.

I would especially like to thank my group mates and friends, Lin Meng Fang, Vanessa Chong, Jingshan Luo, Kishan Gorityala, Rami Naidu, Oleksander Malyi, Seenuvasan and other friends from whom I have learnt a great deal, not only about research, also about working together. I appreciate all the technical and academic staff of MSE for their kind assistance and help. I would like to thank the School of Material Science and Engineering, Ministry of Education (MoE, Singapore), for providing me the financial support.

Finally, my deepest gratitude goes to my parents and my brother to whom I owe every success and achievements of my life. Their constant support and encouragement at every phase of my life has brought me here today.

Siva Krishna

Table of Contents

List of Figures

List of Tables

List of Publications

Journal papers

1. **Siva Krishna Karuturi**, Lijun Liu, Liap Tat Su, Yang Zhao, Hong Jin Fan, Xiaochen Ge, Sailing He and Alfred Tok Iing Yoong*, "*Kinetics of Stop-Flow Atomic Layer Deposition for High Aspect Ratio Template Filling through Photonic Band Gap Measurements*", The Journal of Physical Chemistry C 2010, 114, 14843-14848.
2. **Siva Krishna Karuturi,** Chuanwei Cheng, Lijun Liu, Jinping Liu, Hongxing Li, Liap Tat Su, Alfred Iing Yoong Tok* and Hong Jin Fan* "*Quantum dots sensitized TiO_2 inverse opal for photoelectrochemical water splitting*", Small 2012, 8 (1), 37-42.
3. **Siva Krishna Karuturi**, Chuanwei Cheng, Lijun Liu, Liap Tat Su and Hong Jin Fan*, Alfred Iing Yoong Tok*, "*Inverse Opals Coupled with Nanowires as Photoelectrochemical Anode*", Nano Energy 2012, 1(2), 322.
4. **Siva Krishna Karuturi**, Jingshan Luo, Chuanwei Cheng, Lijun Liu, Liap Tat Su, Hong Jin Fan* and Alfred Iing Yoong Tok*, "*Three-dimensional Ordered Hierarchical Nanobushes Photoanode for Highly Efficient Photoelectrochemical Cells*", Advanced Materials (DOI: 10.1002/adma.201104428) 2012, accepted.
5. **Siva Krishna Karuturi,** Lijun Liu, Alongkarn Chutinan, Liap Tat Su, Taw Kuei Chan, Thomas Osipowicz, Nazir P. Kherani,* Alfred Iing Yoong Tok*, "*Gradient inverse opal photonic crystals via spatially controlled template replication of self-assembled opals*", Nanoscale 2011, 3, 4951-4954.
6. **Siva Krishna Karuturi**, Jingshan Luo, Lijun Liu, Liap Tat Su, Alfred Iing Yoong Tok, and Hong Jin Fan*,"*Homogeneous Photosensitization of Complex TiO_2 Nanostructures for Efficient Solar Energy Conversion*", Scientific Reports 2012, 2, 451.
7. Lijun Liu, **Siva Krishna Karuturi**, Liap Tat Su and Alfred Iing Yoong Tok*, "*TiO_2 inverse-opal electrode fabricated by atomic layer deposition for dye-sensitized solar cell applications*", Energy and Environmental Science 2011, 4, 209-215.

8. Lijun Liu, **Siva Krishna Karuturi**, Liap Tat Su and Alfred Iing Yoong Tok "*Electrochromic Photonic Crystals with Versatile Color Tunability*" Electrochemistry Communications 2011, 11, 1163.
9. Liap Tat Su, Jun Ye, **Siva Krishna Karuturi**, Lijun Liu, Yang Zhao, Jun Guo and Alfred I. Y. Tok*, "*High index, reactive facets controlled synthesis of one-dimensional single crystalline rare earth hydroxide nanobelts"*, CrystEngComm 2011, 13, 5367.
10. Monan Liu, Xianglin Li, **Siva Krishna Karuturi**, Alfred Iing Yoong Tok, Hong Jin Fan*, "*Atomic Layer Deposition for Nanofabrication and Interface Engineering*", Nanoscale 2012, 4(5), 1522.
11. **Siva Krishna Karuturi**, Liap Tat Su, Jingshan Luo, Lijun Liu, Xinfeng Liu, Jun Guo, Tze Chien Sum, Renren Deng, Hong Jin Fan, Xiaogang Liu*, Alfred Iing Yoong Tok*, *"Photon Upconversion in Heteronanostructured Photoanodes for Enhanced Near-Infrared Light Harvesting",* Advanced Materials 2012, accepted.

International conference presentations

1. "*Synthesis and Characterization of TiO_2 Inverse Opals for Solar Cell Applications"* Compound Semiconductor Photonics: Materials, Devices and Integration, **ICMAT 2009, Singapore**.
2. "*Investigation of Atomic Layer Deposition on High Aspect Ratio Surfaces Using Photonic Crystals*" **ALD2010,** 10th International Conference on Atomic Layer Deposition, **South Korea**.
3. *"Photoelectrochemical performance of TiO_2 inverse Opal electrodes by atomic layer deposition"* **Asianano 2010, Japan**.
4. *"Three-dimensional Photonic Crystal Optical Geometry for Enhanced Power Conversion Efficiency of Solar Cells"* Photovoltaic Materials and Devices, International Conference on Materials for Advanced Technologies, **ICMAT 2011, Singapore.**

Patents

1. "*Gradient atomic layer deposition in nanoporous materials*", Siva Krishna Karuturi, Lijun Liu, Liap Tat Su and Alfred Iing Yoong Tok, US provisional patent 61/450,724.
2. "*Electrochromic photonic crystals with versatile color tunability*", Lijun Liu, Siva Krishna Karuturi, Liap Tat Su and Alfred Tok Iing Yoong, US provisional patent 61/571, 150.

ABSTRACT

Three-dimensional (3D) inverse opal (IO) photonic crystals are potential candidate materials for nanostructured photoanode to realize highly efficient photoelectrochemical (PEC) solar energy harvesting. IO nanostructure possesses several beneficial characteristics for light harvesting such as direct electron transport paths for longer electron diffusion lengths, highly percolated pore structure for close interfacial contacts with the electrolyte, light trapping to improve photon absorptions and high surface area for greater photosensitizer loading. This thesis focuses on the design and fabrication of IO based nanostructures using atomic layer deposition (ALD) and investigation of PEC hydrogen generation using the IO nanostructures as photoanode of a PEC cell. Manly, detailed studies are performed to evaluate the optical and PEC performances of the IO based nanostructures and establish the key parameters which enable efficient PEC solar energy harvesting.

TiO_2 IO nanostructures are developed by controlled infiltrations of self-assembled polystyrene opal templates using ALD method. ALD infiltration kinetics is investigated using stop-flow process in comparison with conventional continuous flow (pulse-purge) process. The deposition in opal templates is found to be limited by the Knudsen flow of precursor gases into the nanostructure templates. Stop-flow process is shown to enable the controlled filling of high aspect ratio opal templates with filling fractions close to theoretical maximum and deposition cycle time one order magnitude lower than continuous-flow process. As fabricated TiO_2 IO samples using stop-flow ALD are

photosensitized with CdS quantum dots and applied as a photoanode for visible light driven PEC hydrogen generation. It is observed that TiO_2 IO photoanodes possess fast photoresponse and efficient charge transfer properties. Photocurrent density and IPCE maxima are found to increase with decreasing pore size due to the increase in quantum dots loading.

Bilayer photoanodes based on optically and electrically coupled ZnO nanowires with TiO_2 IO are developed using ALD to improve photon absorptions and light harvesting efficiency through photonic crystal light manipulations. Results have revealed that the bilayer nanoarchitectures contribute to the improved light harvesting through Bragg diffractions and slow light. Nevertheless, surface area shortage is observed to be the main limitation for PEC performance of these photoanodes. In order to address the surface area requirement, we have designed 3D ordered nanobushes by hierarchically integrating dense networks of ZnO nanowires with TiO_2 IO. Tuning the diameter of the IO shells is shown to promote high diffuse scattering. A comparative PEC performance investigation has demonstrated the promise of the nanobushes photoanode for highly efficient PEC solar energy harvesting as supported by greatly improved specific surface area and strong light scattering.

Chapter 1

Introduction

1.1 Background and Motivation

Current global energy demand is estimated to be around 13 TW, which is ever growing. Scarcity of energy supplies may begin as early as 2050 as majority of the present resources are non-renewable.[1] Solar energy is a constant renewable source available in many areas across the world. The solar power reaching the earth from the sun is 1.76×10^5 TW.[2] From this, at least 600 TW reaches the earth in places where it is feasible for collection. Solar energy harvesting technologies with low costs and high efficiencies can strongly influence the global spread of solar power as the main stream energy source. Although commercially available single crystal silicon photovoltaics provide ~15% conversion efficiency, they suffer from high manufacturing costs.[3] Development of clean energy solutions is of significant interest to address the increasing concerns over the global energy shortage and greenhouse effect from CO_2 emissions. Therefore, new approaches are needed to harvest solar photons efficiently to meet the clean energy demands in the future.

Photoelectrochemical (PEC) cells have attracted worldwide attention as cheap alternative to conventional photovoltaic devices for solar energy conversion and storage.[4] PEC solar hydrogen generation from water provides a promising solution to address the above mentioned concerns simultaneously by collecting and converting the solar energy

into the clean chemical fuel.[5] Critical to the light harvesting efficiency of a PEC cell is a nanostructured photoanode where the incident photons are captured, electron hole pairs are generated and the subsequent electron transfer takes place.[6] Nanostructured materials of wide bandgap semiconductor oxides such as ZnO and TiO_2 are very attractive because of their high electron mobility, good photoactivity and low cost. However, their large bandgap limits the portion of absorbable solar light. Tremendous effort has been paid in the last decade to improve the PEC hydrogen generation efficiency. In general, visible light absorption is enhanced by sensitizing with narrow bandgap semiconductor quantum dots (QDs) like CdS, CdSe, PbS etc.[7] In spite of the remarkable progress to address the functional limitations of the material systems, effective nanoarchitecture of the photoanode materials has yet to be realized for efficient light harvesting.

Purpose designed nanoarchitecture of the photoanode possessing high surface area, efficient electron transportation as well as reduced carrier diffusion length and charge recombination losses is highly essential to the performance. In particular, three dimensional (3D) inverse opal (IO) nanostructure, which is an inverse shell structure of face-centered-cubic (fcc) self-assembled opal, provides direct electron transport paths, very high specific surface area and interconnected pore structure with high porosity (~74%). Moreover, the periodical IO photonic crystal provides additional avenues to improve the light-matter interactions by controlling the propagation of light via photonic bandgap effect. Accordingly, IO nanostructure is anticipated to be an ideal electrode design for PEC energy harvesting applications. In fact, a nature leaf has 3D hierarchical structures which favor the multiple scatting and absorbance of light, thus providing strong light harvesting for photosynthesis.[8] Nevertheless, in practice, PEC performance of IO based nanostructures

has been mainly limited by the complexity of the fabrication of IO nanostructures. Atomic layer deposition (ALD) has evolved as a unique tool for nanotechnology for the films depositions with atomic level control, 3D conformality and homogeneity.[9] Thus, the nanoscopic control of the fabrication of 3D IO based nanostructures using ALD could lead to the development of high performance nanostructured PEC photoanode.

1.2 Research Objectives and Scope

The main research objective of the present work is to investigate PEC performance of semiconductor oxide IO based nanostructures by exploring the nanostructure design strategies developed using ALD for improved light harvesting. The scope of this research work is categorized as follows.

- To setup self-made ALD and investigate the kinetic mechanism of controlled opal infiltration.
- To develop high quality IO nanostructures using ALD for PEC cell applications.
- To study the PEC performance of inverse opal based nanostructures fabricated by ALD as photoanode by photosensitizing with CdS QDs for visible light driven PEC hydrogen generation.
- To establish the key parameters that contribute to the efficient PEC light harvesting efficiency of IO based nanostructures by investigating their optical, microstructural, and PEC properties.
- To develop IO based nanostructures for highly efficient PEC solar energy harvesting.

1.3 Organization of the Thesis

Chapter 2 presents literature review on PEC cells and nanostructured photoanodes. Other topics such as; IO photonic crystals, ALD are also discussed. This chapter also identifies the current status and problems in these topics.

Chapter 3 provides detailed description of the experimental methods used in the project. Mainly, the methodology used for the fabrication of nanostructured IO photoanodes and PEC performance measurements is described. Experimental details are also presented for microstructural and optical characterizations.

Chapter 4 covers the investigation of ALD kinetics to obtain controlled infilling of self-assembled opals. Systematic investigation of the effect of various kinetic parameters on the deposition uniformity of TiO_2 is presented based on infiltration in porous framework of self-assembled opal photonic crystals. Characterization of the depth profiles of infiltrated opals using photonic bandgap characterizations is also presented.

Chapter 5 deals with the study of PEC hydrogen generation performance of CdS QDs sensitized TiO_2 IO photoanodes. Effect of pore size variation of inverse opal on PEC performance is also discussed.

Chapter 6 introduces the design of bilayer nanostructure photoanodes by coupling TiO_2 inverse opal photonic crystal with 1D ZnO nanowires in order to improve the light harvesting efficiency through mirrors reflections and light localization within the photoanode. This chapter describes the fabrication, optical, microstructural and PEC performance of bilayer nanostructures.

Chapter 7 presents the fabrication strategy to hierarchically integrate dense networks of ZnO nanowires with TiO_2 inverse opals to develop 3D ordered nanobushes. Improved PEC energy harvesting efficiency of nanobushes-CdS photoanode is also demonstrated by investigating optical and PEC properties.

Chapter 8 concludes the thesis and lists the recommendations for future directions.

1.4 Major Contributions of the Thesis

The main contributions from in this research work are summarized as follows;

1. Controlled and conformal infilling of opal templates (high aspect ratio substrates) with high filling fractions was achieved using stop-flow ALD for fabrication of high quality IO based nanostructures for PEC applications.
2. Structural integration of ZnO nanowire with TiO_2 inverse opals was achieved by selectively confining ZnO seed film and the subsequent growth of ZnO nanowires on nanostructured surfaces using ALD. This enabled the fabrication of two novel nanoarchitectures for photoanode applications, namely bilayer nanostructures and nanobushes.
3. IO based nanostructures were investigated for visible PEC hydrogen generation by sensitizing with CdS QDs. Contribution of optical and microstructural properties of the IO nanostructures to light harvesting efficiency has been studied.
4. This work demonstrated inverse opal based nanostructures developed using ALD as a promising nanostructured material platform for PEC solar energy harvesting.

Chapter 2

Literature Review

In this chapter, an introduction to photoelectrochemical (PEC) solar cells, water splitting and nanostructured photoanode is presented. Further, recent progress in the fabrication of inverse opal (IO) nanostructures and their applications for solar energy harvesting is presented. Finally, this chapter introduces atomic layer deposition (ALD) as a conformal template filling technique to develop high quality IO based nanostructures for PEC applications.

2.1 Photoelectrochemical Solar Energy Harvesting

Increasing awareness of the limited energy resources on earth has driven many investigations to search for alternative means of renewable energy supply. Solar energy is one of the most important and abundant sources of clean energy. However, the efficiency of the current solar cell technologies is still lower than the existing fossil and nuclear sources technologies. Although commercially available single crystal silicon photovoltaics provide ~15% conversion efficiency, they suffer from high manufacturing costs. Hence, novel materials-based solutions are needed to develop cheaper, smaller and more efficient solar energy technologies.[10-12] In this direction, a greater interest has been spread among the scientific community in recent years to develop liquid junction PEC cells for converting light into either electricity or chemical fuel using cheaper fabrication methods (expensive,

high vacuum and high temperature processes used for the traditional devices can be eliminated).[4-6, 13, 14]

2.1.1 Introduction to photoelectrochemical cells: A simple schematic illustration of the liquid junction PEC solar cells is shown in Figure 2.1. It consists of a semiconductor nanostructured photoactive electrode (photoanode) that absorbs and converts solar photons into electricity.[6, 15] Unlike traditional photovoltaic devices that employ the solid state junction between two different semiconductor materials to generate electron-hole pairs, PEC cells employ a liquid-junction between a photoanode and a cathode. The redox electrolyte acting as a liquid junction between the two electrodes regenerates the cell by ensuring the ionic conduction between the electrodes.

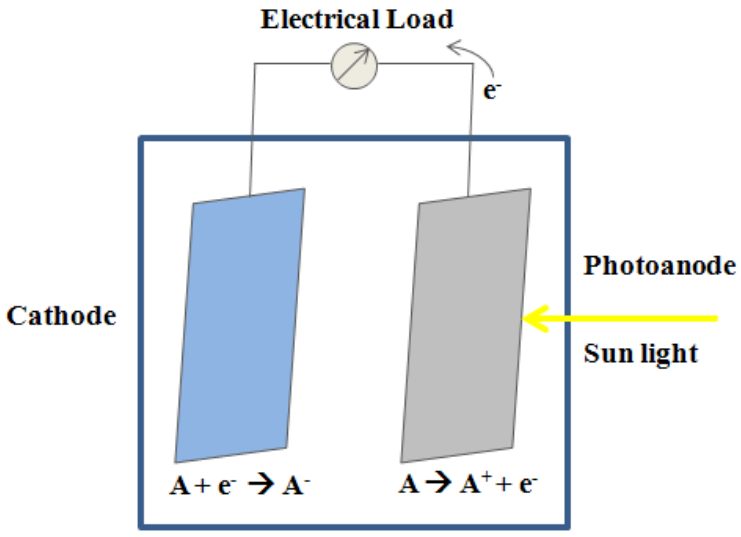

Figure 2.1 *Schematic representation of the regenerative photoelectrochemical cell for solar light conversion into electricity.*

Two types of PEC solar cells, namely, dye sensitized solar cells (DSCs) and semiconductor quantum dots sensitized solar cells (QDSSCs), have been the main focus of

the PEC solar energy harvesting research. Dye-sensitized solar cells (DSCs) have been proven to be a credible low-cost alternative to the conventional photovoltaics.[16] However, although the power conversion efficiency of the champion cell has reached above 10%, it is still quite low for widespread usage.[4] In order to make it competent with other types of solar cells, much effort has to be taken place to improve its power conversion efficiency significantly. This requires numerous approaches such as developing new organic sensitizers for enhanced light absorptions, alternative redox couples for increased V_{OC}, novel device structures for eventually much improved device efficiency etc.[17, 18]

On the other hand, QDSSCs have recently attracted significant attention worldwide due to their strong photoresponse in the visible light spectrum. The absorption wavelengths and bandgap properties of the QDs can be easily tuned by means of controlling the size of QDs. In addition, QDs offer new avenues to improve the power conversion efficiency above the Shockley and Queisser limit of 32% for silicon based solar cells by generating multiple charge carriers through hot electrons.[19] Several QDs nanocrystals such as CdS, CdSe, PbS, and PbSe have been applied as photosensitizers with maximum power conversion efficiencies of up to ~5% reported so far.[20-22]

2.1.2 Hydrogen generation by photoelectrochemical water splitting: PEC solar light driven water splitting technique holds great promise to address both the energy and environmental issues simultaneously, by splitting H_2O molecules to generate O_2 and H_2, tantamount to storing the photon energy in the chemical bond of H_2.[23-25] Hydrogen is a promising energy carrier with advantages of high energy density (143 kJ kg^{-1}) and clean combustion as represented by equation 2.1.

$$2H_2(g) + O_2(g) \rightarrow 2H_2O \quad \Delta H_c = 572\,KJ\,mol^{-1}. \qquad (2.1)$$

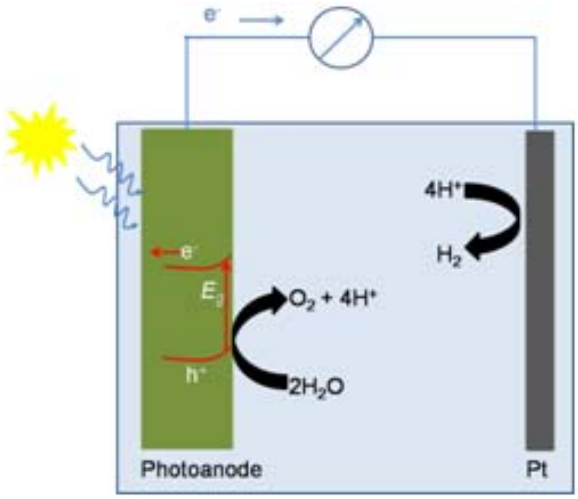

Figure 2.2 *Schematic representation of the non-regenerative photoelectrochemical cell for water splitting.*

PEC water splitting was inspired from the chemistry of nature photosynthesis in which a combination of light harvesting, photoinduced charge separation and catalysis captures solar energy and split water into oxygen and "hydrogen" (in the form of reducing equivalents). Thus the invention of efficient, cost effective artificial materials systems under the guidance of the key steps of natural photosynthesis would be a major step towards efficient solar energy harvesting. In 1972, Fujishma and Honda pioneered an artificial analogue to photosynthetic water splitting with UV light, using the semiconductor TiO_2 to absorb photons, separate charges and catalyze water oxidation to generate O_2.[25] Electrons were pumped to a Pt counter electrode, which reduced protons to generate H_2, as schematically illustrated in Figure 2.2. After their pioneering work, tremendous efforts have been carried out to develop new materials and approaches showing improved solar water splitting efficiency.[26-29] These efforts include: 1. Band gap engineering by doping

with various elements (N, C, S, Fe^{3+}, Nb^{2+}); 2. Assembly of photocatalyst/electrocatalyst onto semiconductors 3. Use of nanostructured materials to improve the electron transport properties and minimize the carrier diffusion distance; 4. Sensitization with narrow bandgap materials such as CdS, CdSe, CdTe, PbS to enhance the visible harvesting etc. However, after nearly four decades of research, the relatively low efficiency of water splitting still hinders the practical applications of PEC water splitting. Most of the previous research work focused mainly on the functional limitations of photosynthesis and overlooked the effect of nanoarchitecture of the photoanode.

2.1.3 Nanostructured photoanode: Crucial to the light harvesting and conversion efficiency of a PEC cell is a nanostructured photoanode where the incident photons are captured, electron hole pairs are generated and the subsequent electron transfer takes place.[4, 6] To realize highly efficient PEC cells, nanostructured photoanode should possess adequate specific surface area to permit higher photosensitizer loading (in the case of TiO_2), direct electron transport pathways for longer electron diffusion length and light scattering to promote the light harvesting ability by confining the light within the cell. Recently, nanostructured materials of wide bandgap semiconductor oxides such as ZnO and TiO_2 have received great attention as high-performance photoanodes for PEC cells because of their high electron mobility, good photoactivity and low cost.[7, 30-33] In particular, much work has been devoted to 1D nanostructures such as nanowires and nanotubes as they possess several advantages such as direct electron transport pathways, reduced carrier diffusion length and diminished charge recombination during the interparticle percolation which occurs in random nanoparticle networks of conventional nanoparticle electrodes.[34-40]

Nevertheless, the insufficient surface area of the 1D structures in comparison to the nanoparticle electrodes restricts the overall energy conversion efficiency. Nanoparticle films provide very high surface area to effect the higher sensitizer loading, but they lack direct electrical contacts and light scattering ability.[33, 41] Thus judicious tailoring of the morphology of such nanostructured photoanodes is central to the further development of efficient energy conversion.[42-45] In conjunction with these efforts, 3D IO nanostructures possessing highly ordered interconnected shells, high porosity (~75%) and photonic crystal light localization have been shown promising in photovoltaics and PEC cells.[17, 46-52] The highest PEC solar cell efficiencies of 3.47% and 2.7% have been reported for dye-sensitized and QDs sensitized unmodified TiO_2 IO photoanodes, respectively.[46, 49]

2.2 Inverse Opal Photonic Crystals

Photonic crystals are the periodic dielectric structures that prohibit the flow of light in certain wavelengths called photonic bandgaps. Eli Yablonovich first suggested the possibility of inhibition of spontaneous emission in photonic bandgaps of 3D periodic dielectric structures.[53] Sajeev John reported the mechanism for strong localization and confinement of photons in certain disordered dielectric superlattices.[54] Subsequently, by the use of well-understood theory developed in solid state physics on electronic properties of materials and X-ray diffraction theory of atomic crystals with Maxwell's equations for the propagation of electromagnetic waves, the field of photonic crystals has seen a great progress theoretically and experimentally.[55]

IO structures are 3D photonic crystals that possess photonic bandgaps in the (111) direction and offer tremendous potential for controlling the propagation of light and localization of photons involved in photochemical reactions. IO photonic crystals provide the ability to trap, reflect, and slow the light, and thus an infrastructure to enhance the light-matter interaction through optical coupling.[53, 54] In addition, IO structure has attracted attention as effective nanostructured photoanode material whose high surface area and 3D interconnected macroporous skeleton are believed to be beneficial for higher sensitizer (dye or QDs) loading, and faster electron transport.[46, 47]

Several groups have prepared TiO_2 IO structures and applied as a photoanode for DSCs.[46, 56, 57] Figure 2.3 shows the schematic illustration of fabrication of IO nanostructures and incorporation in DSCs. First, opal films are fabricated using a bottom-up approach that makes use of self-assembly of monodispersed polystyrene (PS) spheres with submicron particles sizes to grow a 3D structure.[58] After the growth of the 3D opal crystals, a high dielectric material such as TiO_2 is then infiltrated into the void spaces between the spheres by some chemical or physical deposition methods, followed by removal of the spheres through chemical etching or burnout, thus creating an inverted opal.

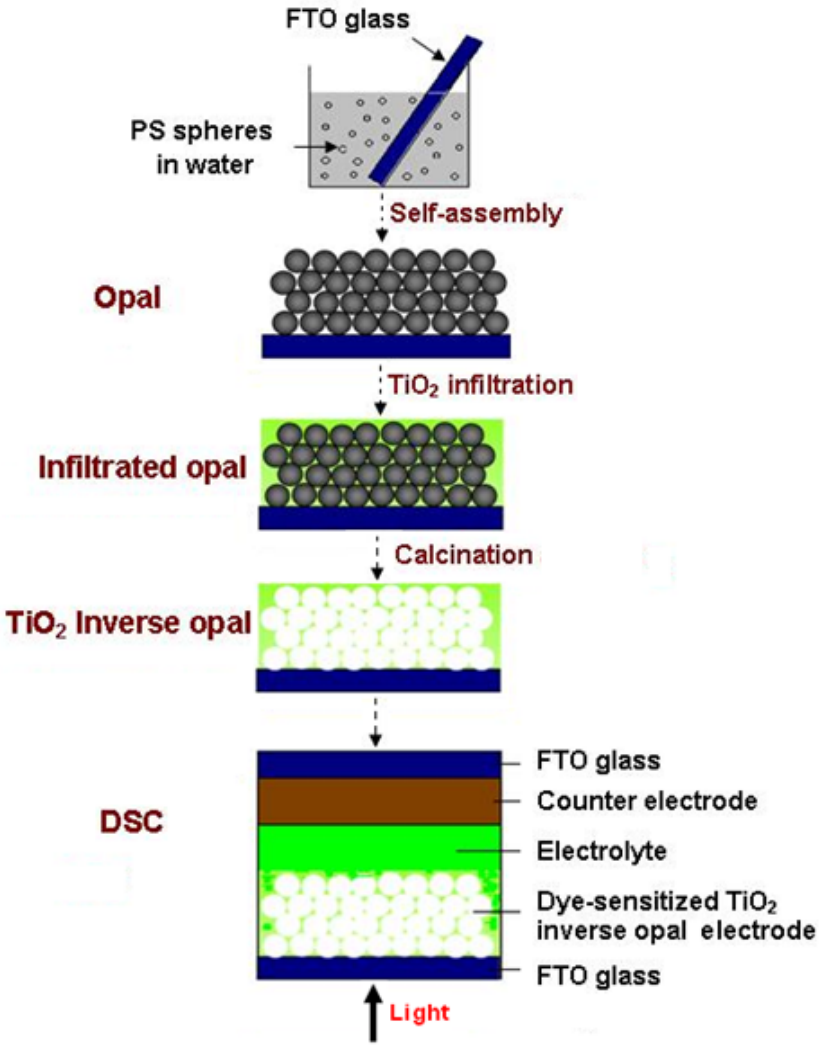

Figure 2.3 *Schematic illustration of fabrication of TiO_2 inverse opal photoanode for dye sensitized solar cell applications (here, the thicknesses of FTO glass, Pt coating on counter electrode and TiO_2 inverse opal films are ~2 mm, ~5 nm, and ~10 μm, respectively).*

The mechanism of performance enhancement of DSCs using IO structures has been extensively analyzed by Mihi and Míguez et al.[59-61] While the light harvesting could in theory be improved greatly, the power conversion efficiency in practice has been quite low owing to great complexity of the fabrication of IO nanostructures. In all the previous works, sol-gel TiO_2 infiltration has been used to fabricate IO nanostructures for DSC

applications. For IO photonic crystals operating in the UV-Vis, the sphere size is ~200-500nm, and void space between the spheres is very small (<40nm), making it difficult to achieve full infiltration of the opal template. Hence, a low infilling, high weight loss and crack formation after burn out of infiltrated opal template resulted in very low power conversion efficiency of DSC.

On the other hand, IO photonic crystals have been shown promising as optical components for energy applications by allowing light of certain energy range (photonic bandgaps) to be reflected back through coherent Bragg diffraction,[62, 63] light with frequencies overlapped with the edges of the photonic bands to travel at strongly reduced group velocity,[64, 65] as well as light to be trapped through surface resonant modes and multiple scattering in disordered regions.[66, 67] Utilizing such optical amplifications, some work has been devoted in the past few years to TiO_2 nanoparticle film/ IO photonic crystal bilayer nanostructures to enhance the light harvesting of dye-sensitized solar cells.[17, 48, 62, 68-70] In spite of the potential dual benefits of IO structure in a bilayer nanoarchitecture, i.e. photonic crystal and intrinsic photoanode contribution, of TiO_2 IO structures, it is still a great challenge to integrate TiO_2 IO with other nanostructure films with robust electrical contacts and strong optical coupling.

2.3 Atomic Layer Deposition

2.3.1 Introduction to ALD: ALD, pioneered by Toumo Suntola in the 1970s, is a modified chemical vapor deposition process that is used to deposit monolayer films.[71] The process was originally called atomic layer epitaxy (ALE) due to the epitaxial nature of the growth. The term 'ALD' is generally used to describe the film depositions where the film

growth does not necessarily follow the structure of the substrate. ALD is also referred to as atomic layer chemical vapor deposition (ALCVD), molecular layering, and molecular layer epitaxy in the literature.

ALD is a gas-phase thin film growth method allowing thickness control at atomic level and with high uniformity. ALD is based on sequential self-limiting reactions between gas-phase precursor molecules and a solid substrate surface, i.e., the precursor reacts with the target substrate until all available surface reaction sites are consumed. The ALD deposition proceeds through conformal and saturative growth steps resulting in a constant increase of thickness in each step. A schematic illustration of ALD process is shown in Figure 2.4. First, a metal precursor is pulsed into the deposition chamber where it chemisorbs on the surface of the substrate. Next, the deposition chamber is purged with neutral gas such as nitrogen to remove excess precursor left in the gas phase as well as physisorbed reactant gases. Subsequently, the nonmetal precursor is pulsed into the chamber. The nonmetal precursor chemisorbs on the surface by reacting with the metal layer forming a molecular thin film. This is followed by another neutral gas purge step to remove excessive non metallic precursor as well as the gaseous byproducts. Films depositions can be controlled at one atomic layer at a time due to the sequential chemisorption of the reactants in a self-controlling manner.

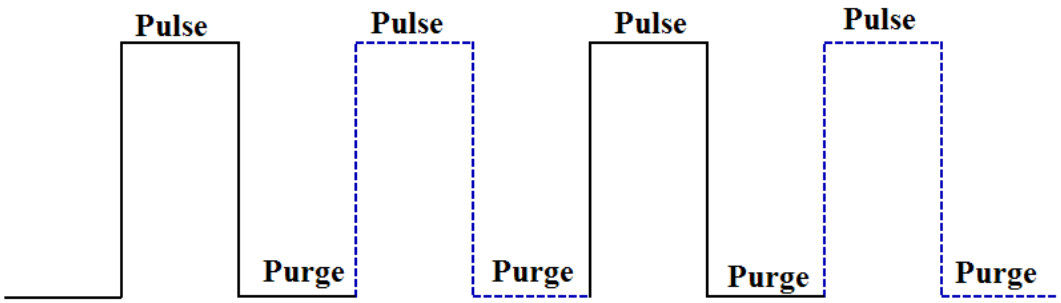

Figure 2.4 *Schematic representation of atomic layer deposition process sequence.*

2.3.2 Applications of ALD in nanotechnology: Unlike chemical vapor deposition, ALD prevents the precursors meeting each other by introducing them into the reaction chamber in sequential steps, thus eliminating gas phase reactions and allowing atomic layer-by-layer deposition with nearly 100% step coverage. Hence, the deposition thickness on even high aspect ratio substrates can be precisely controlled by setting the ALD cycles. Because of these merits, ALD is becoming an important tool in semiconductor industry for the deposition of high-*k* oxides (e.g., HfO_2 and Al_2O_3), diffusion barriers, and 3D trench capacitors.[9] Recently ALD has been employed to tailor physical properties of nanomaterials (e.g., strengthening of spider silk,[72] addition of photocatalytic effect to magnetic materials[73]) and for nanofabrications of complex nanostructures by coating on templates (e.g., hollow particles,[74] tubes,[75, 76] peapods,[77] and compound wires via interfacial solid state reactions[78-82]).

Essentially due to its relatively low process temperature (e.g., ~50°C for Al_2O_3, TiO_2 and ZnO) and 3D conformity at angstrom level, ALD is becoming a powerful tool for surface engineering of high surface area nanostructures that are being studied for energy application in PEC cells, battery, photovoltaics, and photocatalyst. Film depositions are realized for complex non-planar topographies. ALD method has been used to develop

several functional nanostructures such as nanowires, nanodots, nanobowls, nanotubes, 2D and 3D photonic crystals.[83-86]

2.3.3 ALD for inverse opal fabrication: Fabrication of high quality inverse opals for PEC photoanode application requires highly precise infiltration of dielectric materials with uniform thicknesses all the way till the substrate surface. Several methods have been used to create IO structures such as hydrolysis of sol-gel precursors, polymerization of liquid monomers, electrochemical deposition, nanocrystal infiltration and chemical vapor deposition. Most of these methods yielded fillings of less than 50%.[87, 88] Recently, ALD has been shown as a potential technique to achieve 100% infiltration due to its conformal nature of deposition.[89-91] Nevertheless, understanding of the depth controlled infiltration towards a precise control of IO nanostructure fabrication is missing.

ALD in extremely complicated surfaces is more difficult than that over flat surfaces; in the former case, a non uniform degree of saturation in the nanostructures is generally produced, leading to a thickness gradient from the top surface to the bottom. Due to the difficulty of direct access to the deeper surfaces during or after the deposition, understanding the mechanism and control of ALD in high aspect ratio substrates have been a complicated research problem. Attempts have been made to establish the deposition kinetics in 3D surfaces.[92-96] However, for these investigations, there are a few shortcomings such as effective quantitative descriptions for ALD processes with respect to aspect ratios to identify the limitations and advantages of ALD processes for nanostructure fabrication.

Understanding the mechanism and control of ALD in high aspect ratio (AR) substrates is not straightforward due to the difficulty of direct access to the deeper surfaces during or after the deposition. The George group used in-situ conductance measurements and ex-situ

electron probe microscopy for mesoporous tubular membranes and anodic alumina respectively to investigate the high aspect ratio deposition kinetics.[94, 97] The Gordon group proposed a simple and effective model based on Knudsen molecular flow to establish the kinetic requirements of ALD with respect to the structural parameters of the nanostructures.[98] They recently performed ex-situ Rutherford backscattering spectrometry for the depth profile analysis of silica aerogel monoliths in order to explore the mechanism of deposition in ultra high AR nanoporous solids.[92] However, all the previous studies using high aspect ratio templates focused only on coating of few nanometers to modify the original surfaces. Highly precise filling can significantly improve the robustness, reliability and provide great control over the functional properties of nanostructures. Replication of high aspect ratio templates with complete filling necessitates stringent kinetic requirements due to the continual increase in aspect ratio (or shrinkage of pore opening) with the progress of deposition.

2.4 Summary

3D IO nanostructures possessing highly ordered interconnected shells, high porosity and photonic crystal light localization were shown as a promising candidate materials for nanostructured photoanode of PEC cells. In previous works, the performance of IO photoanodes has been limited by the great complexity of its fabrication. ALD has the potential to develop high quality IO structures for PEC applications by achieving 100% infiltration of the opal templates due to its conformal nature of deposition. Nevertheless, ALD infilling of high aspect ratio templates such as self-assembled opals is very

challenging. A non-uniform degree of infiltration of the nanostructures is generally produced, which is detrimental to the electron transport properties of the as-fabricated IO nanostructures. In addition, detailed studies to understand of the PEC performance of IO nanostructures is critical to identify the parameters that contribute the light harvesting and to develop the nanoarchitecture design strategies based on IO for efficient PEC light harvesting.

Therefore, this project focuses on the following issues towards developing IO based nanostructured photoanode for highly efficient PEC cells.

- Investigation of ALD infilling kinetics for better understanding of the controlled infiltration of the opal templates to develop IO structures for PEC applications.
- Fundamental studies to understand the PEC performance of the IO based nanostructures developed using ALD method.
- Design of the IO based nanostructures towards fulfilling the requirements of an ideal nanostructured photoanode for efficient PEC cells.

Chapter 3

Experimental Methods

In this chapter, description of the experimental methodology used for the fabrication of nanostructured photoanodes and photoelectrochemical (PEC) performance measurements is presented briefly. The typical experimental steps involved are as follows;

- Fabrication of nanostructured photoanodes.
- Morphological and microstructural characterization of nanostructures including X-ray diffraction, transmission electron microscopy and field emission scanning electron microscopy.
- Optical characterizations including specular reflectance, transmittance and diffuse reflectance.
- PEC performance measurements such as photocurrent density (I-V characteristics), photocurrent stability (I-t measurements) and incident-photon-to-electron conversion efficiency (IPCE).

3.1 Fabrication of Nanostructures

IO photonic crystals with the desired photonic bandgap positions can be fabricated using a "bottom-up" approach that makes use of self-assembly method to grow a three-dimensional (3D) structure based on polystyrene spherical building blocks. Monodispersed colloidal polystyrene spheres with submicron particles sizes are first used to create opal

templates using self-assembly in face centered cubic lattice structure that can be subsequently utilized as a template for making IO photonic crystals. Several techniques have been used to form this template, ranging from natural sedimentation to forced sedimentation.[58] After the growth of the self-assembled opal films, a high dielectric material such as TiO_2 is then infiltrated into the void spaces between the spheres using chemical or physical deposition methods, followed by the removal of the spheres using chemical etching or burnout, thus creating an IO structure as illustrated schematically in the Figure 3.1.

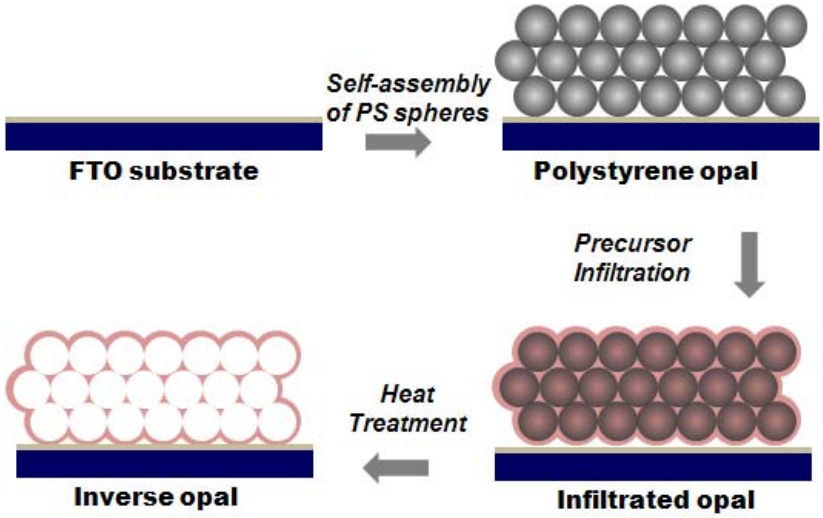

Figure 3.1 *Schematic representation of fabrication of inverse opal photonic crystals.*

3.1.1 Self-assembly of polystyrene particles: Carboxyl-modified, monodispersed polystyrene particles of 10% solid content and desired diameters are bought from Duke scientific corporation for opal template preparation. Opal synthesis is carried out using vertical convective self-assembly technique.[99] Fluorine doped Tin Oxide (FTO) coated glass was used as a conductive substrate on which the opal self-assembly was carried out. Substrate was dipped into a vial containing a suspension of monodispersed polystyrene

colloidal spheres of controlled concentration, followed by resting the vial in the oven at 90 ^{o}C. Solvent evaporates slowly overnight at controlled temperature environment. As the evaporation of the liquid occurs, meniscus seize down along the substrate surface and the capillary forces in the meniscus draws the spheres from the suspension to self-assemble into face centered cubic (*fcc*) structure on the substrate surface. Schematic process of the self-assembly is illustrated in Figure 3.2.

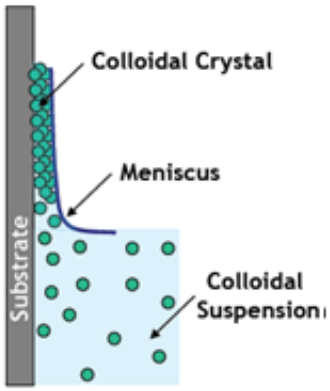

Figure 3.2 *Schematic representation of the growth process of self-assembled polystyrene opals.*

3.1.2 Atomic layer deposition infiltration of opals: Custom-designed viscous-flow reactor type of atomic layer deposition (ALD) as shown in Figure 3.3 was setup for this work as described in the litearature.[100] Titanium tetrachloride with 99.999% purity purchased from Sigma Aldrich and deionized water were used as precursors for TiO_2 deposition.[101] Carrier gas precursor flow rates of 4:1 and 8:1 are used for H_2O and $TiCl_4$. For ZnO deposition, diethyl zinc (DEZ, 99.99%, Sigma Aldrich) and H_2O were used as the Zn and O precursors, respectively. Deposition is carried out at a constant temperature of 70^{o}C. In this work, the polystyrene opal templates are infiltrated with ALD of TiO_2 and modified with ZnO ALD.

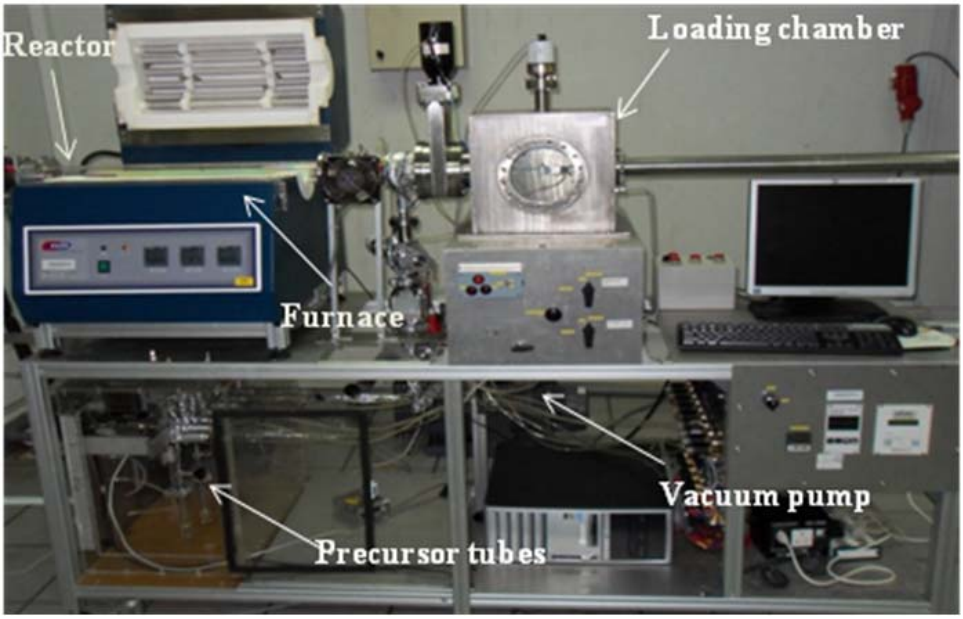

Figure 3.3 *Self-made atomic layer deposition system.*

3.1.3 Heat treatment and etching: Infiltrated opal samples are heat treated at 450 ^{o}C in a box furnace in the presence of air to decompose and burn away the PS spheres template, there by transforming the infiltrated opal to TiO_2 inverse opal photonic crystal subsequqntly crystallizing amorphous TiO_2. Reactive ion etching (RIE, NSC ES371) was used to etch the top surface and open up pores.

3.1.4 Solution growth of ZnO nanowires: A standard solution growth method was used to grow ZnO nanowires.[102] The substrate was immersed into an autoclave filled with 35 mL aqueous solution of equimolar hexamethylenetetramine ($C_6H_{12}N_4$) and zinc nitrate ($Zn(NO_3)_26H_2O$) (0.02M). The reaction was conducted at 95 ^{o}C for controlled growth time. After the synthesis reaction, the substrate was recovered from the solution, dipped into deionized water and dried with nitrogen gas.

3.1.5 CdS quantum dots sensitization: Nanostructured films on FTO substrates were photosensitized with CdS quantum dots (QDs) using a modified method of previously reported SILAR route.[12] In a typical process carried out in the glove box, the substrates of the nanostructured films were placed in a solution of 50 mM cadmium acetate tetrahydrate ($Cd(Ac)_2.2H_2O$, Alfa Aesar 98%) in ethanol for 1 min, which allows the adsorption of Cd^{2+} onto the internal surface of the nanostructures. The nanostructured films were then dried using a gentle stream of nitrogen gas. Subsequently, the dried electrodes were dipped into a solution containing 50 mM sodium sulfide nonahydrate (Na_2S, Alfa Aesar 98%) in methanol for 1 min, which allows the reaction of pre-adsorbed Cd^{2+} with S^{2-} to form the desired CdS film on the internal surface. Finally, the electrodes were rinsed in deionized water for 1 min to remove the excessive ions and dried in the gentle stream of N_2 gas. This procedure was repeated for ten times in order to get desirable thickness of CdS QDs. To further improve the crystallinity of CdS QDs film, the resulting sensitized substrates were annealed in an argon protective atmosphere at 400 °C for 30 min.

3.2 Micro-Structural and Optical Characterizations

The morphology and microstructures of the nanostructured films were examined using a JEM 2100F transmission electron microscope (TEM) and a JEOL JSM-7600F field emission scanning electron microscopy (FESEM). The X-ray diffraction (XRD) patterns were recorded using Shimadzu thin film XRD equipment using Cu Kα radiation. The diffused reflection spectra measurements were taken using Zolix Solar Cell QE/IPCE apparatus furnished with an integrating sphere and a silicon diode detector.

UV-Vis-NIR Cary 5000 spectrophotometer (Varian Inc.) was used to measure specular reflectance and transmittance data. Reflectivity measurements are carried at an incident angle of 20^{o}. Transmittance measurements were carried out at zero degree incident angle to the normal. Refractive index values for TiO_2 films were obtained from specular reflectivity and spectral ellipsometry measurements.

3.3 Photoelectrochemical Performance Measurements

The PEC performance measurements were carried out in three electrodes configuration, where Ag/AgCl in saturated KCl, Pt foil and the as fabricated nanostructures on FTO substrates were used as the reference electrode, counter electrode and working electrode, respectively. A mixed solution of 0.35 M Na_2SO_3 and 0.25 M Na_2S was used as electrolyte. The photoresponse measurements were performed under chopped irradiation from a 150W Xe lamp (Sciencetech SS150) with an AM1.5 G filter. The instrument was calibrated with a standard Si solar cell to simulate AM1.5 illumination (100 mW/cm^2). Photocurrent stability tests were conducted by measuring the photocurrent produced under chopped light irradiation (light/dark cycles of 50 s) at a fixed bias of 0.5 V vs Ag/AgCl. A specially designed IPCE system for solar cells (Zolix Solar cell Scan100) in two electrodes configuration was used to measure the incident-photon-to-electron conversion efficiency in wavelengths ranging from 300 to 700 nm. The bias voltage input for IPCE measurement in two electrode setup was chosen as the bias at which photocurrent density level in the two electrode setup is equivalent to that in three electrode system at 0 V bias. A monochromator equipped with gratings and a 150 W Xe lamp were used to produce monochromatic beam. The intensity of the incident light was calibrated using a standard

silicon photodiode. Electrochemical impedance spectra (EIS) were evaluated using Potentiostat (CHI760 D, CH instrument) under AM 1.5 illumination in a frequency range of 10^{-1} to 10^{5} Hz with an applied bias of open-circuit voltage and 5 mV amplitude.

Chapter 4

Controlled Infilling of Self-Assembled Opal Templates using ALD

4.1 Introduction

This chapter has been reproduced with permission from the journal paper "*J. Phys. Chem. C* **2010**, *114*, 14843-14848",[103] by Karuturi, S. K *et al.*; Copyright: American Chemical Society.

In this chapter, study of atomic layer deposition (ALD) kinetics to obtain controlled infilling of self-assembled opals is presented. As discussed in the literature review in chapter 2, controlled template infilling lowers the shrinkage induced cracks and improves the interfacial contact with the substrate which is anticipated to greatly benefit the electron transport properties of the inverse opal (IO) nanostructures for photoelectrochemical cell applications. With increasing attention of ALD coatings in extremely complicated surfaces with high aspect ratios (AR) ($\geq 10^3$), there is a great need for understanding the deposition kinetics to develop defect-free nanostructures towards applications in various disciplines. Highly precise infilling can greatly improve the reliability, robustness and provide control over the functional properties of the fabricated nanostructures.

ALD on complicated surfaces is more challenging than that over flat surfaces. In the former case, a non uniform degree of saturation in the deeper surfaces is generally

produced, leading to thickness gradients of the deposited films from the top to bottom. Replication of high AR templates with full filling necessitates stringent kinetic control due to the continuously shrinking pore opening with the progress of deposition. Investigation of the mechanism of ALD in high aspect ratio surfaces is very complicated due to the difficulty of accessing the deeper surfaces. All the previous studies using high AR templates focused only on coating of few nanometers thickness to modify the actual surfaces. Understanding of infilling control and detailed ALD process optimization for high AR template replication accounting for shirking pore size with the progress of the deposition is still lacking. ALD operated in traditional continuous-flow process (pulse-purge) requires very long cycle times and gives lower control in high and ultra high AR surfaces. Stop-flow ALD process is believed to provide better control and obtain high step coverage for deposition in high AR substrates.[90, 104, 105]

In this chapter, systematic investigation of the effect of various kinetic parameters on the deposition uniformity of TiO_2 is presented based on infiltration in the porous framework of self-assembled opal photonic crystals. Deposition was performed in both continuous-flow process and stop-flow process. Transmittance spectra of the infiltrated opals were measured to determine photonic bandgaps (PBGs) of the TiO_2 infiltrated opals. Depth profiles of the deposition was evaluated by comparing the width and position of the PBGs with simulated band structures and correlating with the filling kinetics without the need for further ex-situ characterizations. This study also presents useful information for deposition in similar three-dimensional (3D) templates such as aerogels, trenches and anodic aluminum oxide membranes.

4.2 Experimental Details

Figure 4.1 illustrates the differences between stop-flow and continuous-flow processes. In stop-flow process, the pulse step of continuous-flow process is divided into *fill* and *hold* steps where the precursor gases are filled up to the set pressure and held at this pressure for set time. This additional *fill* step in stop-flow process builds up the chamber pressure and thus enables the deposition at higher precursor partial pressures, which improves the precursor transfer rates into the nanostructured surfaces.

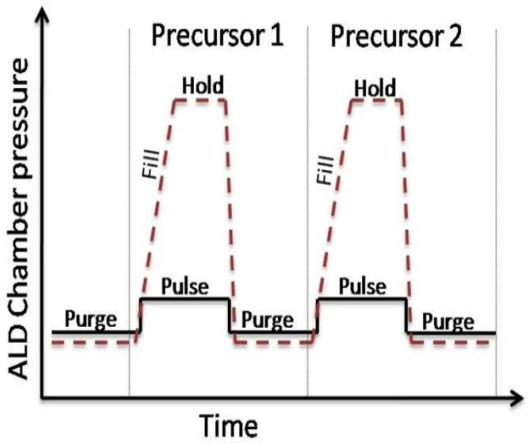

Figure 4.1 *Schematic comparison of one cycle of ALD process for continuous-flow (solid line) and stop-flow processes (dotted line). (Reproduced with permission from Ref. 103; Copyright: American Chemical Society 2010)*

For opal template preparation, carboxyl modified, monodispersed polystyrene particles (510 nm diameter) of 10% solid content were purchased from Duke scientific corporation. Microscopic glass slides were used as substrate as their transparent nature in the wavelength ranges under consideration permits the transmittance measurements. The opal template thickness was maintained at 30 μm and a relatively small surface area of 1×1 cm^2 free from imperfections was separated for the kinetic study by cleaving away the imperfect

surface. Self-made viscous flow reactor type of ALD was used to infiltrate the opal templates with TiO_2 at a constant temperature of 70 ^oC during the deposition. High resolution microstructural images of the opal templates were obtained using FESEM (JEOL JSM 6340F). Specular reflectance and transmittance measurements were performed using UV-Vis-NIR Cary 5000 spectrophotometer (from Varian Inc.). Refractive index values for TiO_2 films were approximated using specular reflectance and spectral ellipsometry measurements.

4.3 Results and Discussion

4.3.1 Depth profile evaluation based on photonic bandgap measurements: Opal templates in face centered cubic arrangement were prepared by self assembly of monodispersed polystyrene spherical particles using vertical self assembly technique (Figure 4.2).[106] Originating from the highly periodic arrangement of polystyrene spheres, opals exhibit photonic band gaps in (111) direction where propagation of light is prohibited within certain wavelength ranges. The size and the refractive index of the spheres dictate the wavelength position and widths of the photonic bandgaps once a close packed structure is fixed.[55] Transmittance or reflectance measurements were used to determine PBGs experimentally. Theoretical photonic band diagrams were predicted using the plane wave expansion method (MIT photonic-bands (MPB) package). Figure 4.3a presents the measured transmittance spectrum (lower part) for opal templates in comparison with its corresponding simulated band diagram (upper part). When void spaces of the opals are filled with ALD of TiO_2, PBGs of infiltrated opals shifts to higher wavelengths due to increased average refractive index. Figure 4.3b shows the bandwidth of PBG for opals

(510nm sphere size) with different filling fractions of TiO_2 from theoretical calculations. It can be noticed that the wavelength position of the PBG red-shifts to higher wavelengths with increase in filling fractions. The bandgap width gradually shrinks to a point where it disappears completely as the refractive index of the background of the photonic crystal (average the refractive index of TiO_2 and the remaining air space) becomes equal to that of the polystyrene spheres and then increases gradually with further TiO_2 filling. Therefore, by following the transmittance spectra of the infiltrated template and comparing Γ-L bands with simulated photonic band diagrams, the filling fractions of ALD infiltrated materials can be evaluated without any ex-situ characterizations.

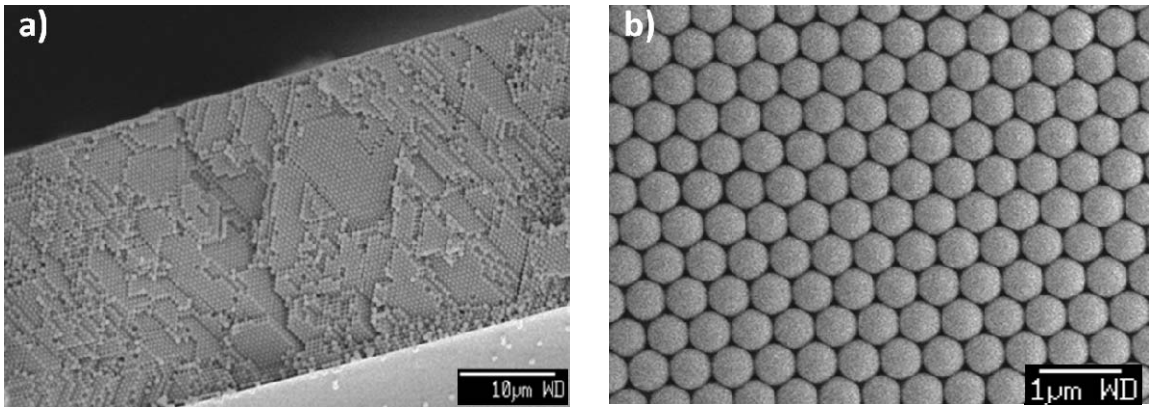

Figure 4.2 *Opal templates used for ALD infiltration kinetic study: (a) cross sectional view, (b) surface view. (Reproduced with permission from Ref. 103; Copyright: American Chemical Society 2010)*

In this study, number of ALD cycles for TiO_2 infiltration was fixed at 400 to ensure coating thickness that corresponds to the maximum possible filling of the opal templates. In the case of non-uniform ALD infiltration, filling fraction of TiO_2 varies with the template depth and maximum filling is expected at the top surface while the lowest filling (f_b) occurs in deeper layers near the substrate. Broadened and multiple peaks in the measured

transmittance spectra are anticipated in case of non-uniformly deposited templates due to the overlapping of peaks from different depths with different filling fractions. Figure 4.3c shows the overall width of bandgap with the extent of non-uniformity in the infiltrated opal template. Therefore, by measuring the width of the bandgaps from the transmittance spectra of the infiltrated opal, it is possible to estimate the depth profile, thereby able to investigate the infilling kinetics using photonic bandgap characterizations as a facile method.

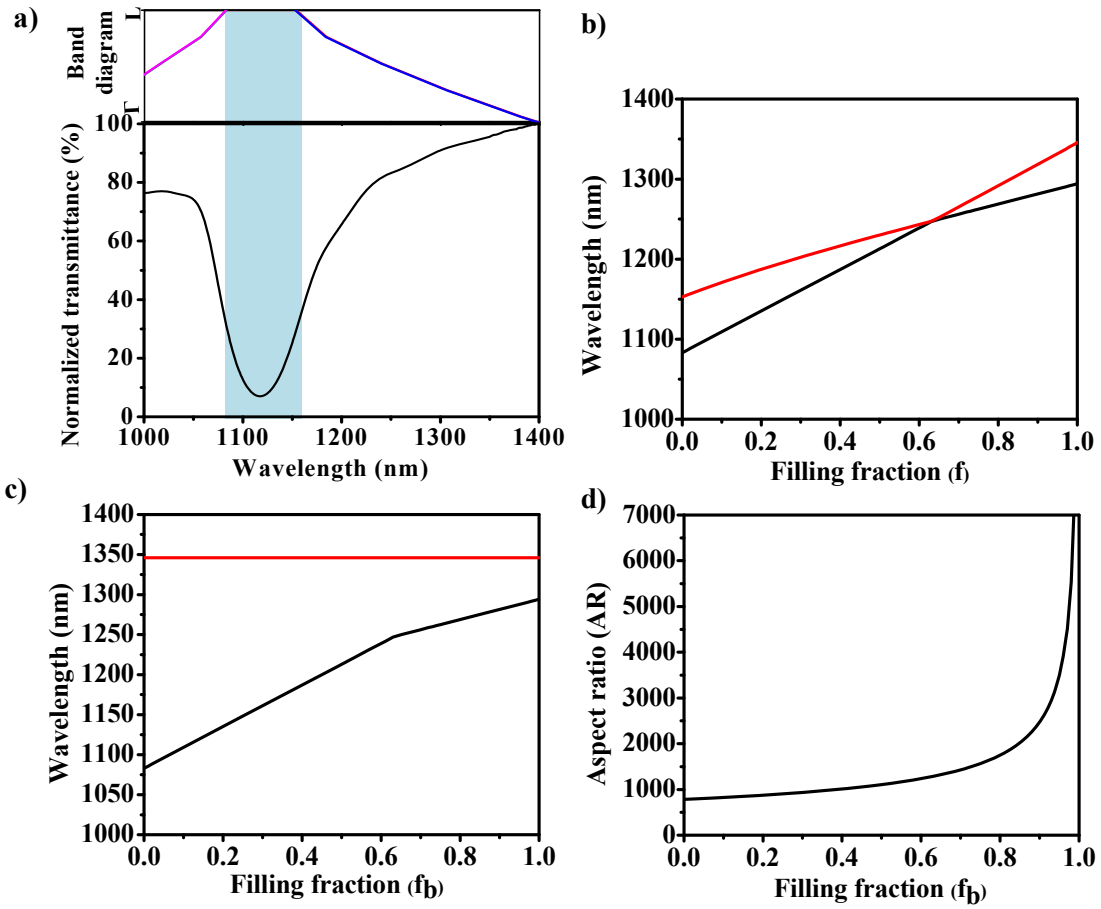

Figure 4.3 *(a) Transmittance spectrum of opal templates used for ALD infiltration (lower part) and simulated band diagram (upper part), (b) simulated band diagram at L for infiltrated opal templates with different filling fractions of TiO_2, showing closing and reopening of the bandgap, (c) simulated width of the bandgap versus lowest filling fraction f_b of the non-uniformly infiltrated template, with the red line indicating higher wavelength position of the bandgap with filling fraction 1.0 and the black line showing the lower wavelength position of the bandgap varying with different filling fractions and (d) aspect ratio of the infiltrated opal structure corresponding to the lowest filling fraction f_b. (Reproduced with permission from Ref. 103; Copyright: American Chemical Society 2010)*

Infilling kinetics are further quantified by correlating with structural parameters of the substrate based on aspect ratios (ratio of longest dimension to the smallest dimension) of the ALD infiltrated opal templates. Longest dimension was approximated as three times the thickness of the opal film (30 microns) as curvaceous paths in the opal structure presents tortuous flow of precursor gases.[107] Shortest dimension was approximated as the diameter of the spherical opening of area equal to the pore opening area between spheres in the FCC arrangement. With the progress of TiO_2 coatings on the spheres, pore size shrinks continuously. Deposited shell thickness and the reduced pore area were calculated using Monte Carlo simulations to estimate the shortest dimension corresponding to the filling fraction f_b. Thus, the calculated aspect ratio of ALD deposition based on the lowest filling fraction f_b (see Figure 4.3d) indicates the aspect ratio below which ALD occurs uniformly throughout the depths, above which non-uniformity sets up and no further deposition occurs at the deepest surfaces of the opal template.

4.3.2 Infiltration of opal templates using continuous (pulse-purge) process: First, ALD was carried out in pulse-purge mode by changing the $TiCl_4$ pulse time (15, 30,

45 and 60 sec) while keeping all other experimental parameters constant. Purge time was fixed at 60 sec for both H_2O and $TiCl_4$. Pulse time of H_2O was maintained at 30 sec. The partial pressure for H_2O was set at four times higher to that of $TiCl_4$. Chamber pressure during the deposition was around 0.35 mbar. In this scenario, it can be assumed that limiting factor to the deposition is the half reaction during $TiCl_4$ pulse considering much higher exposure of H_2O. To reveal the effect of pulse time of $TiCl_4$ on the deposition uniformity, transmittance measurements were carried out for TiO_2 infiltrated opals. As shown in Figure 4.4a, Γ-L bandgap for the infiltrated opal from the transmission spectra with 15 s pulse time is very broad spanning all the way from full infiltration at top (~1350 nm) to lowest infiltration at the bottom (~1100 nm), confirming highly non-uniform ALD infilling of TiO_2. Moreover, infiltration was insufficient in the deeper layers for infiltrated opals with all the exposure times (15, 30, 45 and 60 s). Improvement of deposition uniformity by extending the pulse time up to 60 sec was not good enough to achieve uniform full infiltrations.

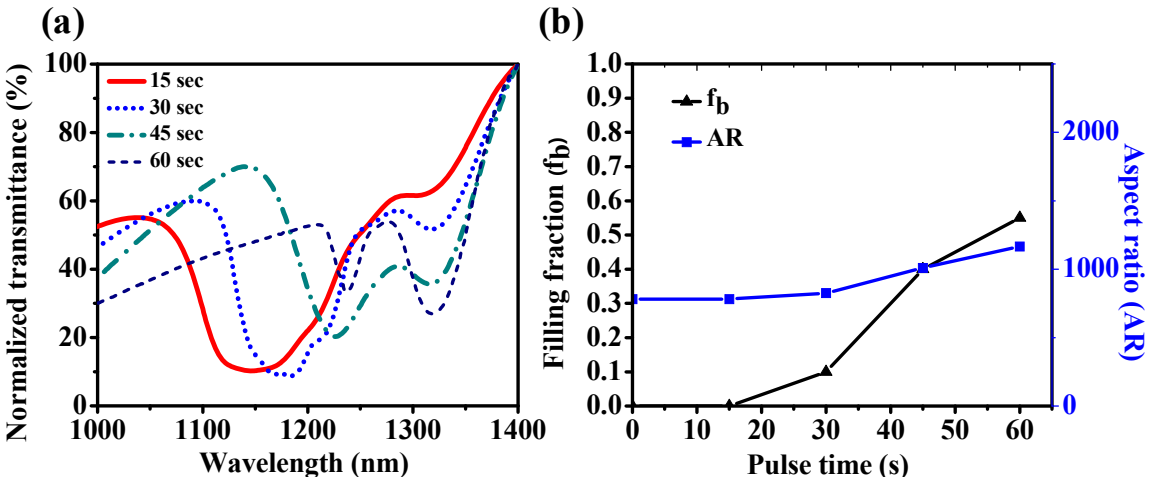

Figure 4.4 *ALD in continuous-flow (pulse-purge) process with varying pulse times of $TiCl_4$: (a) transmission spectra, (b) filling fraction at the bottom and aspect ratio. (Reproduced with permission from Ref. 103; Copyright: American Chemical Society 2010)*

Width of the PBGs measured from the transmission spectra were used to calculate the lowest filling fractions (f_b) and convert into aspect ratios as presented in Figure 4.4b. When the pulse time was doubled from 30s to 60s, AR is increased by nearly square root of two times from 820 to 1170, indicating square root dependence of ARs on exposure time, which is in accordance with the Knudsen diffusion theory.[98] It can also be observed that multiple peaks exist in all the transmission spectra, indicating graded deposition with the depth. With sufficient exposure of Titanium chloride (for pulse time > 30 s), deposition occurred uniformly in the beginning. As the TiO_2 coating thickness on the surface of the polystyrene spheres increases with the progress of the deposition, the pore opening shrinks continuously to cause an increase in aspect ratio, which makes it difficult for the precursor gases to diffuse into the deeper surfaces of the substrate. Deposition is expected to follow the gradient nature subsequently. This type of evolution of infiltrations further confirms the insufficient Knudsen diffusion of $TiCl_4$ precursor as the main cause for non-uniformity.

In accordance to the Knudsen diffusion theory (based on square root dependence of AR on exposure time), continuous-flow process requires about 700 sec of pulse time to realize 96% of the filling uniformly where the AR of the substrate would become 4000 (see Figure 4.3d). By calculating the exposure time for the other precursor based on similar exposure requirements, it can be concluded that the total cycle time becomes too long for a practicable deposition experiment. In addition, half life and reversibility of chemical reactions for several precursors may further exacerbate the quality of deposition.[95]

Lowering the evacuation rate from the chamber or increasing the precursor partial pressures using high temperature precursor vaporization may improve the aspect ratios of the deposition. However, the open vacuum method of deposition makes it very challenging to scale the exposures to achieve high AR infilling. Also, higher volumes of corrosive precursors such as $TiCl_4$ are detrimental to several components of the ALD equipment and pose environmental issues.

4.3.3 Infiltration of opal templates using stop-flow (fill-hold-purge) process: The fill-hold-purge method as illustrated in Figure 4.1 was used to infill the opal structures to achieve uniform filling at lower the cycle time. Systematic study of effect of various process parameters on deposition uniformity for Titanium chloride was carried out as shown in Table 4.1. For water precursor, optimized exposure (Row 1 in Table 4.1) was used in all the experiments to ensure ALD half reaction during the $TiCl_4$ exposure as the deposition uniformity limiting factor.

Table 4.1: Parameters used for opal infiltration using stop-flow ALD

Experiment type	Precursor	Fill pressure, [mbar]	Hold time, [s]	Purge time, [s]
	H_2O	4	20	60
Fill pressure	$TiCl_4$	0.5, 4, 8,12, 16	20	60
Hold time	$TiCl_4$	8	10, 20, 30, 40,50	60
Purge time	$TiCl_4$	12	20	30, 45, 60, 75, 90
Opal thickness	$TiCl_4$	2	10	60

First, infiltration of opal templates were carried out by varying the $TiCl_4$ fill pressure keeping all other deposition process parameters constant (Row 2 in Table 4.1). It can be noticed from Figure 4.5a that width of PBGs of the TiO_2 infiltrated opals with different fill pressures are smaller when compared to that of continuous-flow process (Figure 4.4a), showing improved control of high AR filling. Gradual improvement of uniformity of the deposition with fill pressures from 0.5 to 8 mbar is noticeable, but the trend reversed as the fill pressure increased further. Figure 4.5b indicates that when 8 mbar fill pressure was used for Titanium chloride, deposition uniformity improved significantly. At this pressure, the deeper most layers of the opal template were infiltrated with around 96% of the maximum possible filling. In addition, AR of the TiO_2 deposition is increased by almost 4 times for 8 mbar fill pressure when compared to that of 0.5 mbar.

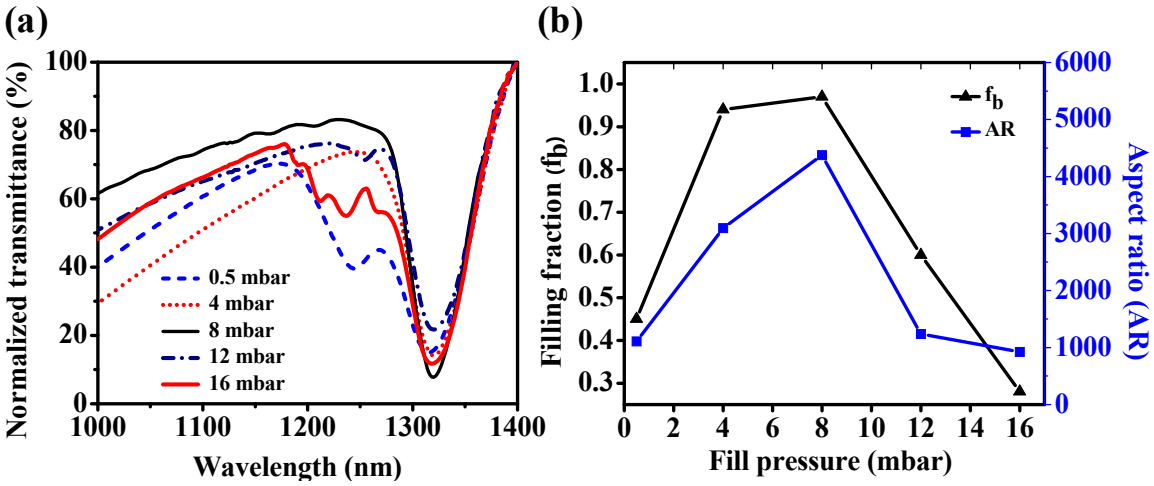

Figure 4.5 *ALD in stop-flow (Fill-hold-purge) process with varying fill pressures for $TiCl_4$: (a) transmission spectra, (b) filling fraction at the bottom and aspect ratio. (Reproduced with permission from Ref. 103; Copyright: American Chemical Society 2010)*

From Figure 4.5b, aspect ratio and precursor fill pressures are in square root dependence which is in accordance with the Knudsen diffusion theory.[98] However, AR of

the ALD infiltrations is anticipated to increase with increasing fill pressure continuously. Deterioration of deposition homogeneity due to reversibility of ALD surface reactions at higher filling pressures is insignificant, as the total cycle time almost remains constant for all experiments. One possible contribution to non-uniformity is that the deposition could have occurred outside the self-limiting reaction zone of ALD. The low deposition temperature (70 ^{o}C) used in this study to avoid the melting of the thermally sensitive polymer template might have caused the condensation of precursor gases on the substrate. If this is true, it would alter all the deposition reaction control during the successive steps and leads to the non-uniformity. To test such a possibility, we performed deposition at even lower temperature of 50 ^{o}C on flat substrates keeping all the experimental conditions the same. The growth rate from the results was found to be around 0.99 Å per cycle which is in accordance with self-limiting sequential ALD growth. Some of the previous work on ALD of TiO_2 conducted at low temperatures on heat sensitive substrates also agrees with our conclusion.[108, 109] Therefore, thermal effect on the deposition uniformity being eliminated, the cause for reversible trend with increasing fill pressures higher than 8 mbar can be hypothesized by the occurrence of chemical vapor deposition (CVD) reactions. Shrinking pore size with the increasing coating thickens makes it increasingly challenging for the excess precursor gases to escape from the internal void space under the limited purge time, which may result in CVD reactions in the subsequent second precursor exposure. Premature pore blocking may occur with this unwanted CVD deposition which may halt the further deposition in the deeper surfaces. In addition, PBGs from the transmittance spectrum for the highest fill pressure of 16 mbar show multiple peaks as against the graded evolution, suggesting the CVD nature of reactions.

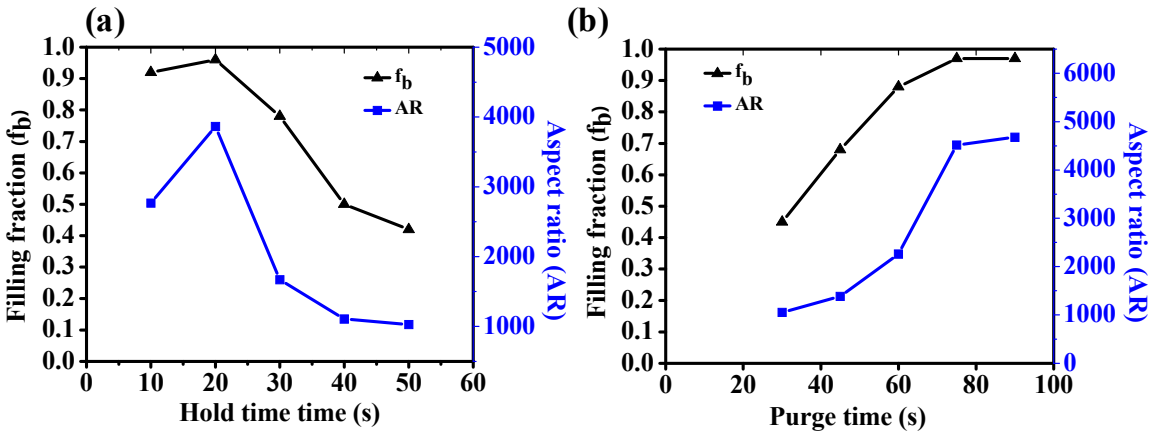

Figure 4.6 *Stop-flow process: filling fractions at the bottom and aspect ratios as a function of (a) the $TiCl_4$ hold time and (b) $TiCl_4$ purge time. (Reproduced with permission from Ref. 103; Copyright: American Chemical Society 2010)*

As shown in Table 4.1, filling experiments were performed by changing the hold time and purge time of $TiCl_4$ precursor in stop-flow process to test whether unwanted CVD reactions are a cause for deposition non-uniformity at higher precursor exposures. Hold time for $TiCl_4$ precursor was gradually varied from 10 to 50 s while maintaining all other parameters constant. An optimum hold time of 20 s from Figure 6a can be noticed. Hold times lower than 20 s resulted in lower infiltration as a result of insufficient Knudsen gas flow into the deeper surfaces. Hold times of 30 s or higher aggravated the uniformity, showing a similar trend with fill pressure experiments.

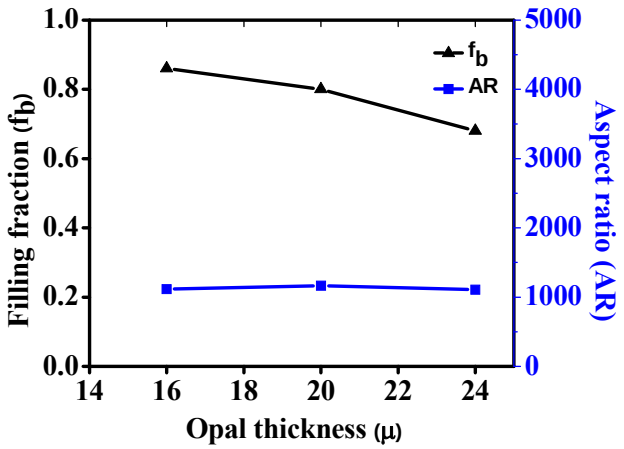

Figure 4.7 *Stop-flow process: filling fractions at the bottom and aspect ratios as a function of opal thickness. (Reproduced with permission from Ref. 103; Copyright: American Chemical Society 2010)*

Figure 4.6b shows the controlled deposition experiments with varying purge times. Filling fractions and aspect ratios of the ALD infiltrations increased continuously all through the purge time variations considered. From the results, purge time of 75 sec can be estimated as an optimum value. These infiltration experiments with varying hold time (Figure 4.6a) and purge time of $TiCl_4$ (Figure 4.6b) confirms that the non-uniformity is caused by the occurrence of CVD reactions from insufficient purge times at higher exposures. Therefore, the purge step in high AR template infiltrations must be optimized in order to allow the back transport of excess precursor gases out of the deep surfaces.

Full and uniform infiltration (> 96%) of the opal templates used in this study needed total cycle time of almost an order of magnitude lower for stop-flow process (filling time + hold time + purge time) in comparison to that of continuous-flow process (pulse time + purge time). Thus, extending the exposure time in continuous-flow process may improve the homogeneity of the high AR template infiltrations (Figure 4.4b), it is less practicable when compared to infiltration control realized in the stop-flow process. The latter not only

lowers the cycle time significantly, but also meets the stringent kinetics requirements for high AR template filling (Figure 4.5b). Finally, template infiltrations were performed for opals of different film thickness to validate the accuracy of PBG based characterizations for depth profiles. Deposition was performed in the Knudsen-diffusion limiting regime in stop-flow processes. Figure 4.7 shows that deposition aspect ratios (variation 5%) are the same for all the templates when infiltrated at the same deposition process conditions. This confirms the photonic bandgaps based characterizations used to quantify ALD deposition kinetics for high AR opal templates infilling are reasonably accurate.

4.4 Summary

In this chapter, investigation of the infilling kinetics of stop-flow ALD was carried out using self-assembled opal photonic crystal templates. For comparison, TiO_2 infiltrations were conducted in both stop-flow and continuous-flow processes. Depth profiles of the deposition experiments were evaluated directly by comparing the photonic bandgaps of the infiltrated opal templates measured from the transmittance spectra with simulated band diagrams. Photonic based characterization of the deposition accurately quantified the filling kinetics within the experimental error. Uniform infilling of opal templates with original AR of around 4000 was realized with precise spatial deposition control using stop-flow process. In summary, the following the key aspects of controlled template infilling by ALD are determined in this study.

1) The deposition in high aspect ratio templates is limited by the Knudsen flow of precursor gases into the nanostructure templates in contrast to the surface reaction limited deposition on flat surfaces.

2) Continuous-flow process demands impractical lengths of cycle times for obtaining full infiltrations due to the lower Knudsen flow rates of precursor gases. Stop-flow process enables the high aspect ratio deposition with cycle times of an order of magnitude lower in comparison to that of continuous-flow process. Hence, the stop-flow process is recommended for high aspect ratio template infilling to avoid the precursor decomposition at longer exposure times.
3) Kinetic investigations also showed that optimum process window for other parameters like purge time is required to eliminate unwanted CVD reactions and premature pore blocking.

Chapter 5

Photoelectrochemical Performance of TiO_2 Inverse Opal Photoanodes Fabricated by ALD

5.1 Introduction

Nanoarchitecture of the photoanode providing high surface area, improved electron transportation as well as reduced minority-carrier diffusion length and charge recombinations is very critical to the performance of photoelectrochemical (PEC) cell.[23, 111] In particular, inverse opal (IO) nanostructure presents very high interfacial area and porosity (74% void volume). In addition, the periodical three-dimensional (3D) IO provides additional avenues to enhance the light-matter interactions via photonic crystal bandgap effect by controlling the propagation of light through back reflections, light scattering, slow photons and surface resonant modes.[67, 87, 112] Therefore, 3D IO nanostructure is anticipated to be an ideal nanostructure design for energy conversion applications. In this chapter, TiO_2 IO are photosensitized with CdS quantum dots (QDs) and applied as a photoelectrode for PEC water splitting as shown in Figure 5.1.

While the CdS QDs acts as light antennas to improve the visible light harvesting, the type II band alignment of CdS QDs with TiO_2 also benefits the charge transfer and separation at the interface. The TiO_2 inverse opals used in this study were fabricated using

self-assembled polystyrene (PS) spheres as sacrificial templates and subsequent TiO_2 infiltration using stop-flow atomic layer deposition (ALD). In the previous chapter, it is showed that stop-flow ALD provides an exceptional filling control (close to a theoretical filling fraction)[103] which minimizes the volume shrinkage induced cracks in comparison to traditional sol-gel infiltration route. In this chapter, a systematic investigation has been carried out to understand the PEC performance of photoanodes based on TiO_2 inverse opals.

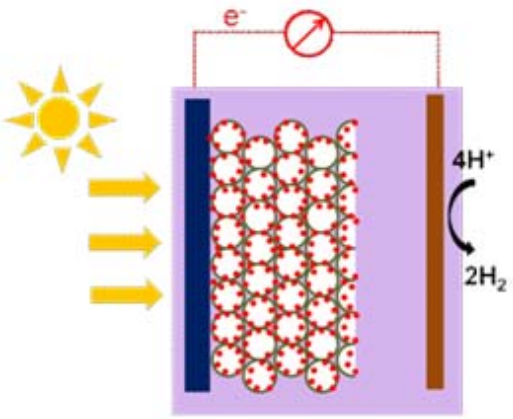

Figure 5.1 *Schematic of the photoelectrochemical cell made of CdS quantum dots sensitized TiO_2 inverse opal as a photoanode. (Reproduced with permission from Ref. 110; Copyright: John Wiley and Sons 2012)*

5.2 Experimental Details

Self-assembled opals were prepared using commercial monodispersed carboxylate-modified polystyrene (PS) particles with different sizes (Thermo Scientific, d = 288, 510 and 900 nm). The PS opals were infiltrated with TiO_2 using a custom designed stop-flow ALD system. Subsequently, the TiO_2 inverse opals were sensitized with CdS QDs using a modified SILAR method. The PEC performance of the electrodes and electrochemical

impedance spectra were obtained in a three-electrode configuration using a Potentiostat (CHI760D, CH instrument). Photocurrent stability tests were performed under chopped light irradiation (light-dark cycles of 50 s) at a fixed bias of 0 V vs Ag/AgCl. The incident-photon-to-electron conversion efficiency (IPCE) was measured using an IPCE system specially designed for solar cells (Zolix Solar cell Scan100), with two electrodes configuration under 0 V bias. Detailed description of the experimental methods can be found in chapter 3.

5.3 Results and Discussion

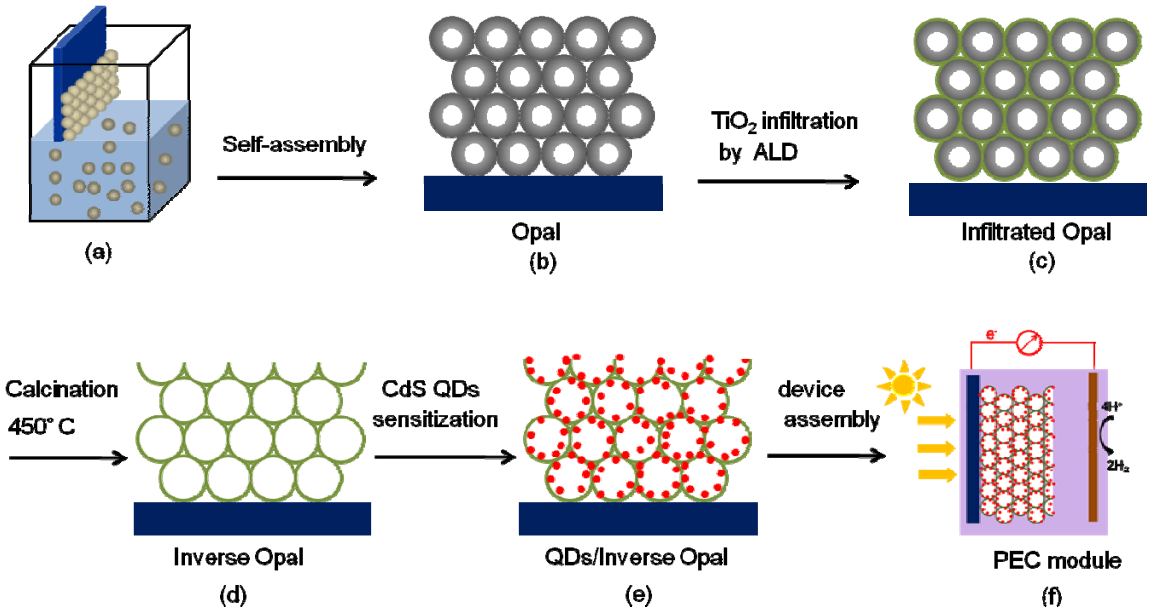

Figure 5.2 *Schematic illustration of the fabrication procedure for CdS quantum dots sensitized TiO_2 inverse opal photoanode (here, the opal films are made from PS particles of 288, 510, and 900 nm diameter and the size CdS QDs is ~7 nm). (Reproduced with permission from Ref. 110; Copyright: John Wiley and Sons 2012)*

5.3.1 Fabrication of photoanode nanostructures and microstructural characterizations: The experimental procedure for the preparation of CdS QDs sensitized TiO_2 IO photoanodes is illustrated by the schematic diagram in Figure 5.2. It consists of four simple fabrication steps: (*a*) PS spheres are self-assembled into close-packed multi-layer structures onto FTO glass substrate, (b) the opals are infiltrated with TiO_2 by stop-flow ALD, (*c*) PS sphere templates are removed by thermal decomposition at high temperature to obtain TiO_2 inverse opals and (*d*) the inverse opals are finally sensitized with CdS QDs using modified SILAR method.

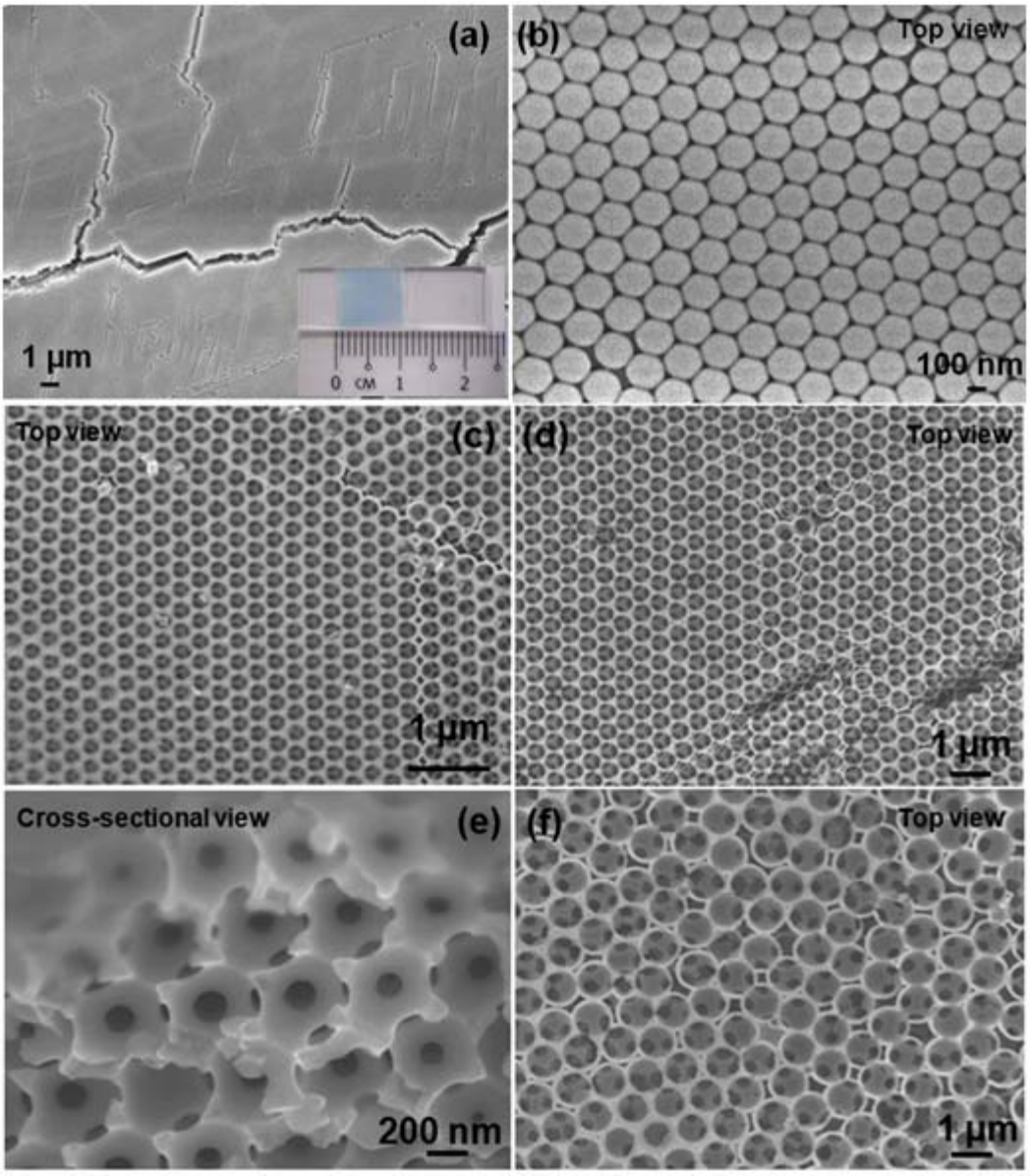

Figure 5.3 *(a-b) FESEM images of opal films taken at different magnifications; Inset in (a) shows the dimensions of the opal film on FTO substrate, (c-f) FESEM images of TiO_2 inverse opals prepared using different sizes of polystyrene spheres; (c) 288 nm, (d, e) 510 nm and (f) 900 nm. (Reproduced with permission from Ref. 110; Copyright: John Wiley and Sons 2012)*

Figure 5.3a and b presents typical FESEM images opal films prepared from 288 nm sized PS spheres, which clearly shows *fcc* arrangement of PS spheres. After the TiO_2 ALD

infiltration and thermal decomposition, TiO_2 inverse opals with 288 nm, 510 nm and 900 nm sizes possessing periodically ordered spherical voids and wide pore interconnectivity were obtained as shown in Figure 5.3c-f. It is noted that this interconnected pore connectivity is very beneficial towards the uniform CdS QDs coating and the unhindered electrolyte infiltration and interfacial contact throughout the entire thickness of the photoanode. The typical thickness of the IO films is measured to be around 6 μm as shown in Figure 5.4.

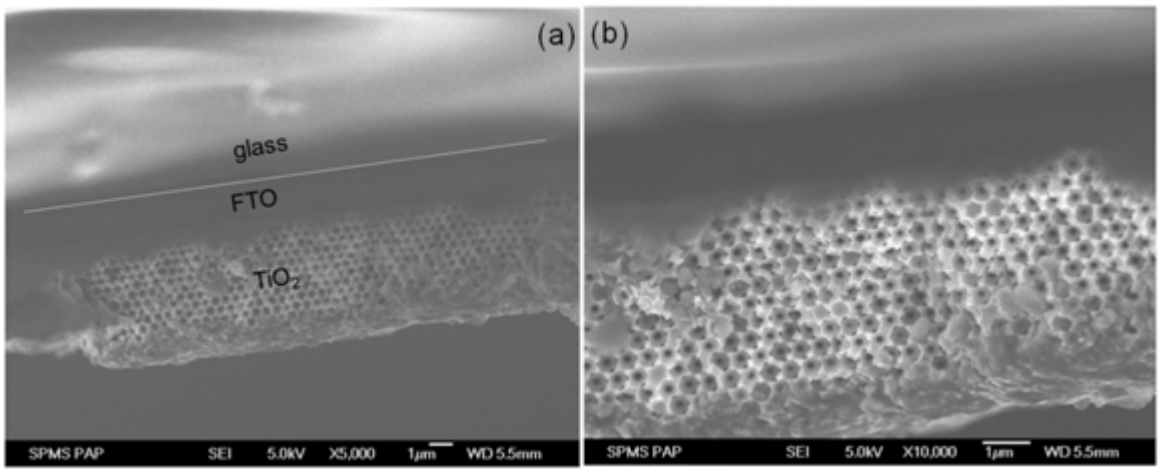

Figure 5.4 *Cross-sectional FESEM images of CdS QDs coated TiO_2 inverse opals of 288 nm pore diameter. (Reproduced with permission from Ref. 110; Copyright: John Wiley and Sons 2012)*

Figure 5.5a shows the FESEM image of the CdS QDs sensitized 288 nm TiO_2 inverse opals with well ordered structure preserved and a uniform coverage of the QDs layer without any aggregation or pore clogging. TEM image in Figure 5.5b gives more detailed perspective of the TiO_2/CdS interface, showing clearly the coverage of CdS on the surface of TiO_2 shells. Both the TiO_2 and CdS are highly crystalline, as seen from the HRTEM image in Figure 5.5c and X-ray diffraction patterns in Figure 5.6. The thickness of CdS

layer can be measured as approximately 7 nm. The fringe spacing of 0.35 nm and 0.26 nm for TiO_2 and CdS QDs in Figure 5.5c corresponds to the *d*-spacing of (101) planes of anatase crystal phase of TiO_2 and the (102) planes of hexagonal crystal phase of CdS, respectively.

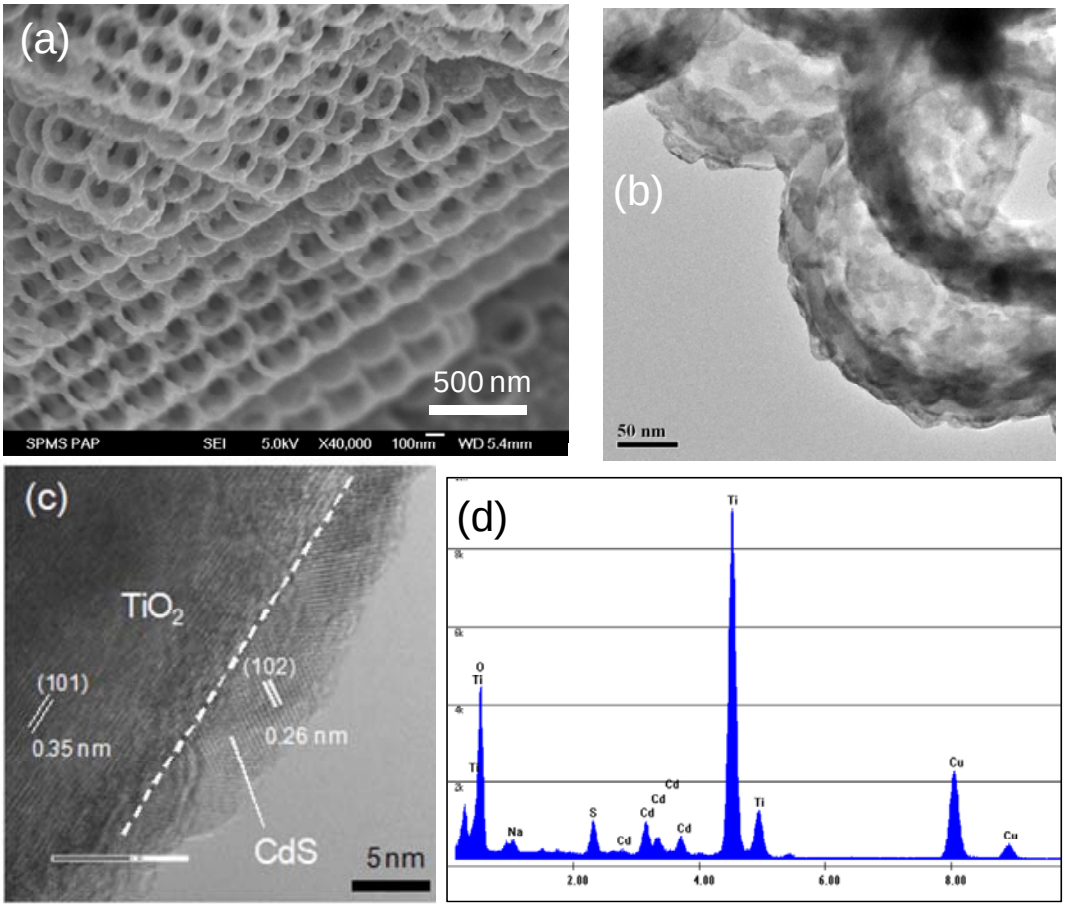

Figure 5.5 *FESEM and TEM images of CdS QDs sensitized TiO_2 inverse opals based on 288 nm polystyrene spheres: (a) cross-sectional image taken at the crack area from 20° tilted view, (b) TEM image of CdS QDs coated inverse TiO_2 shells and (c) TEM image of CdS-TiO_2 interface. (d) TEM-EDX spectrum showing the existence of CdS and TiO_2. (Reproduced with permission from Ref. 110; Copyright: John Wiley and Sons 2012)*

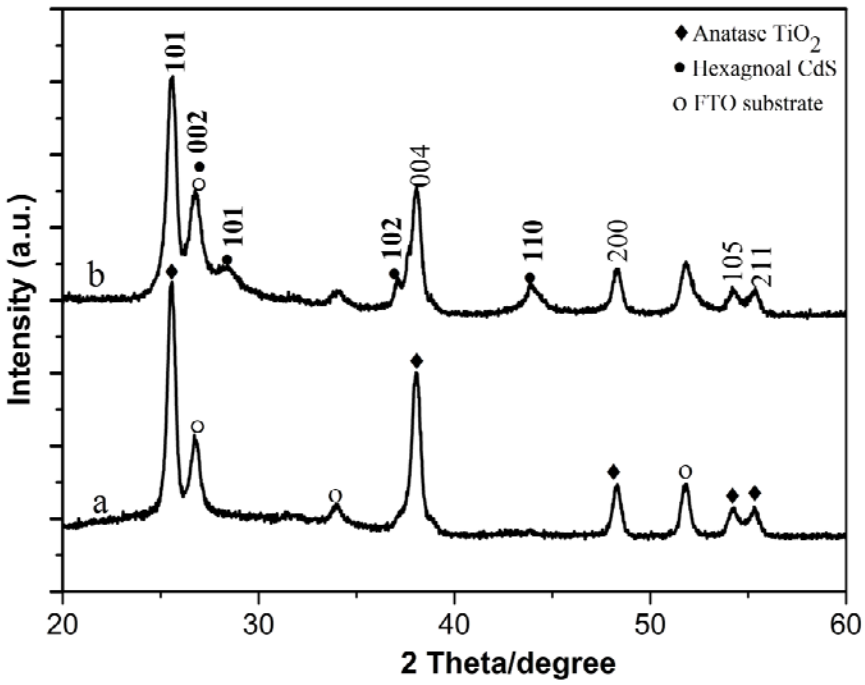

Figure 5.6 *X-ray diffraction patterns of (a) pristine TiO_2 inverse opal of 288 nm pore diameter, (b) CdS QDs sensitized TiO_2 inverse opal. (Reproduced with permission from Ref. 110; Copyright: John Wiley and Sons 2012)*

Highly periodic TiO_2 IO structures function as 3D photonic crystals prohibiting light of certain wavelengths from transmitting through, which correlates to the cavity sizes and the refractive index of periodic structure in accordance with the modified Bragg's law[113] as given in Equation 5.1:

$$\lambda_{\max} = 2\, d_{hkl}[n_{s_s}^2 f + n_f^2(1-f)]^{1/2} \sin\theta \qquad (5.1)$$

Where $\lambda_{\max}$ is the maximum wavelength position of the diffracted peak (the position of the photonic bandgap), d_{hkl} is the inter-planar spacing between *hkl* planes. In case of *fcc* (111) planes of opals, d_{hkl}=0.8165*D,* where *D* refers to the sphere diameter. The n_s and n_f are the refractive indices of the spheres and their surrounding medium, while *f* is the

volume fraction of the spheres. The θ represents the angle of incident beam to the planes (which is 70° in our case).

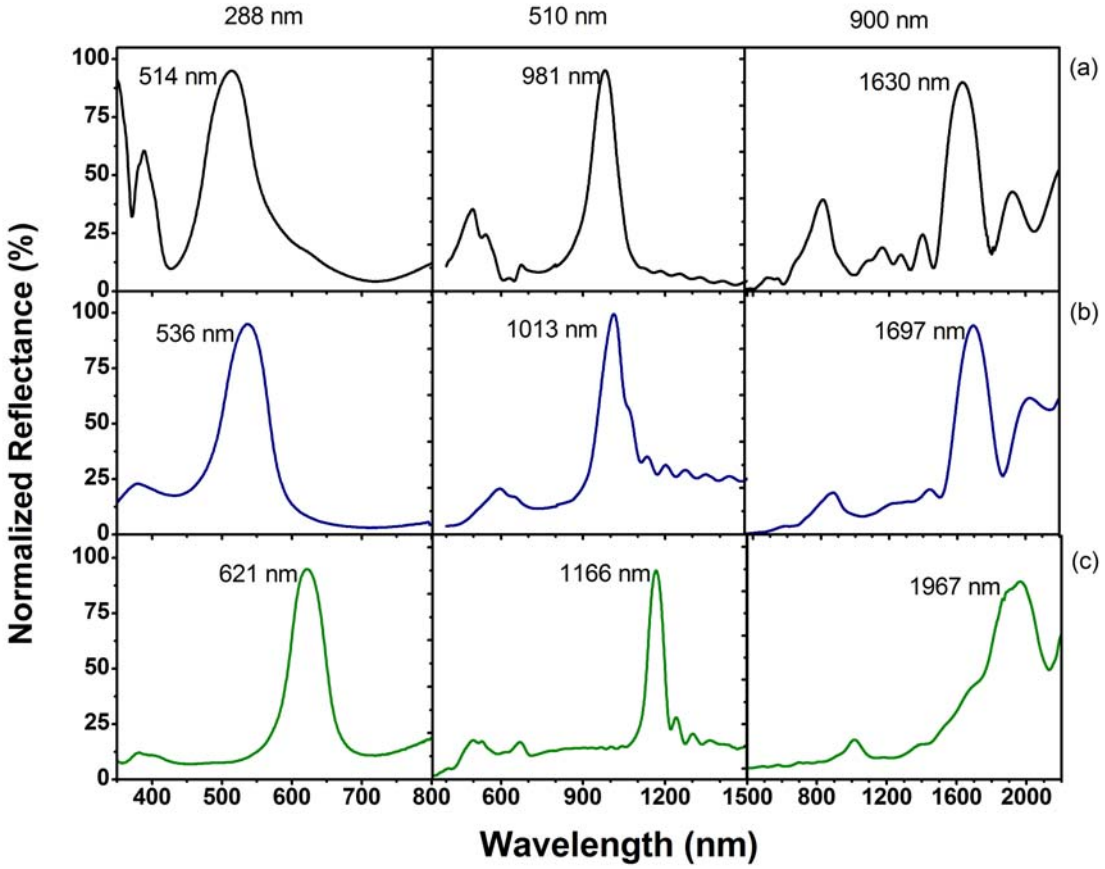

Figure 5.7 *Specular reflectance spectra measured at the 20° incidence to the normal for (a) TiO_2 inverse opals, (b) TiO_2 inverse opals coated with CdS QDs and (c) TiO_2/CdS inverse opals after electrolyte infiltration. (Reproduced with permission from Ref. 110; Copyright: John Wiley and Sons 2012)*

Figure 5.7a shows the specular reflectance measurements for TiO_2 IO from 288, 510 and 900 nm diameter PS spheres, respectively. The corresponding stop band reflectance peaks at 514, 981 and 1630 nm indicates the highly ordered lattice structure in these samples. After the CdS QDs coating, the peak wavelength positions are red-shifted because of the increased refractive index (n_{CdS} = ~2.5, n_{TiO2}= 2.2~2.4, n_{air} = 1). The reflectance

peaks remained sharp in intensity and highly symmetrical with almost unchanged bandwidth, which implies that the uniform coverage of CdS is achieved without causing any damage to the structural order of TiO_2 inverse opal. Further, Bragg peak calculations using Eq. 5.1 after the CdS sensitization indicate that inverse opals of all sizes are sensitized with ~8 nm thickness of CdS QDs, which agrees well with the FESEM and TEM observations. When infiltrated with sulfide electrolyte, the photonic bandgap peaks further red-shifted to a higher wavelength, indicating the complete filling of electrolytes within the air voids of TiO_2.

5.3.2 Photoelectrochemical performance measurements: The current density vs potential measurements were conducted in a three-electrode system under dark and simulated sunlight illumination (AM 1.5, 100 mW cm^{-2}). As shown in Figure 5.8a, all the three photoanodes show negligible photocurrent density in the dark condition, while pronounced photocurrent density values can be observed under light illumination, implying efficient light absorption, charge separation and transport. The photocurrent increases from the typical onset potential of around -1.0 V vs Ag/AgCl and reaches a plateau at around -0.5 V vs Ag/AgCl. It is noted that the photocurrent density is enhanced by ~200 times through CdS QDs sensitization in comparison to that of pristine TiO_2 IO photoanode (Figure 5.9). This indicates that the efficient CdS sensitization has been realized which enhanced the light harvesting efficiency greatly. It can be observed that the photocurrent density at 0 V vs Ag/AgCl increases from 3.02 mA cm^{-2} for photoanode based on 900 nm PS to 4.84 mA cm^{-2} for the one based on 288 nm diameter. The enhancement in efficiency with the decrease of the pore size can be attributed to the higher total surface area for smaller pore

photoelectrode per unit thickness, which leads to higher CdS QDs loading and corresponding light absorptions. Fast photoresponse and good photostability for all the three electrodes is shown in transient photocurrent curves (Figure 5.8b).

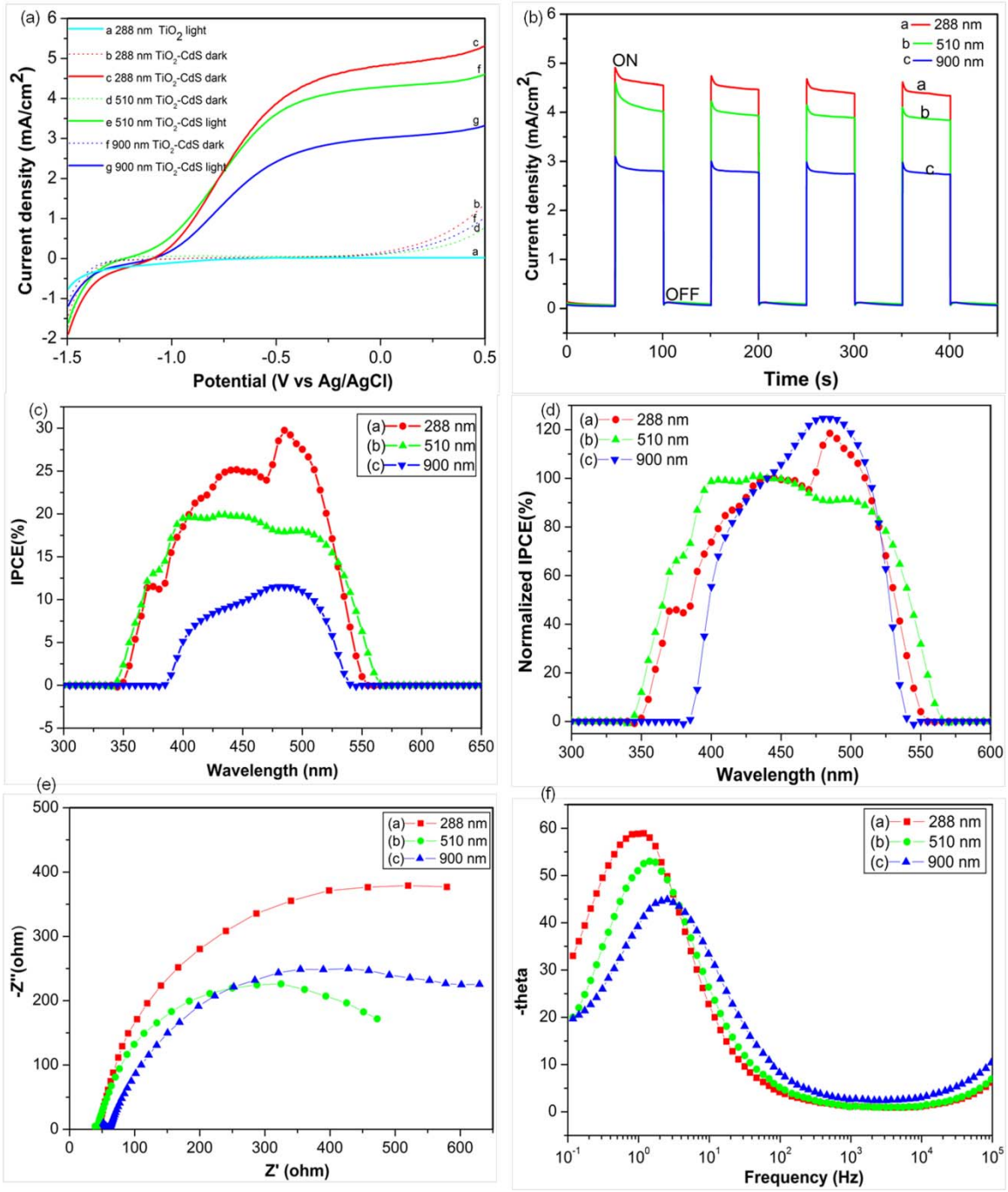

Figure 5.8 *(a) Linear sweep voltammetry measurements of different photoanodes both in the dark and simulated sunlight (100 mW cm^{-2}) illumination, (b) amperometric I-t curves vs AgCl/Ag at an applied potential of 0 V and 100 mW cm^{-2} illumination with 50 s light on-off cycles, (c, d) incident photon to electron conversion efficiency (IPCE) measurements; (c) original IPCE spectra, (d) normalized IPCE spectra at 440 nm and (e, f) electrochemical impedance spectra of the CdS-sensitized TiO_2 inverse opal electrodes; (e) Nyquist plots, (f) Bode phase plots. (Reproduced with permission from Ref. 110; Copyright: John Wiley and Sons 2012)*

In order to understand the wavelength dependent light harvesting of different photoanodes, the incident-photon-to-electron conversion efficiency (IPCE) tests were performed from 300 nm to 650 nm wavelengths. The IPCE spectra as shown in Figure 5.8c presents a strong photoresponse for all the electrodes from 350 to 550 nm, which corresponds to the absorption characteristics of TiO_2 and CdS. The maxima IPCE values of 30%, ~20% and 11% can be observed for 288 nm, 510 nm and 900 nm diameter CdS QDs sensitized TiO_2 IO photoanodes, respectively. This result is consistent to the corresponding photocurrent density measurements as in Figure 5.8a. However, varying photoresponse behavior for different photoanodes relative to the incident light wavelength can be noticed by a closer inspection of the IPCE curves. The IPCE spectra are normalized to reveal the photonic crystal effect. The IPCE spectra were normalized at the wavelength position of 440 nm where all the three electrodes (288, 510 and 900 nm sizes) do not possess any photonic bandgap reflectance characteristics. As shown in Figure 5.8d, the 900 nm photoanode exhibits the highest IPCE value in the range of 440–525 nm, reaching the maxima at around 490 nm in correspondence to the absorption band edge of CdS QDs. From the reflectance spectra in Figure 5.7c, the photoanodes of 288 nm and 510 nm pore

sizes possess higher order photonic reflection bands in the wavelength ranges of 360–430 nm and 450–550 nm, respectively. This can be reasoned for the lower efficiency in these corresponding wavelength regions due to the reflection losses of photons. On the other hand, 900 nm pore photoanode presents the lowest efficiency below 400 nm though it does not show reflectance peaks in this region, which may be due to its lowest surface area, resulting in very low UV light harvesting by TiO_2 and thus low absolute IPCE values.

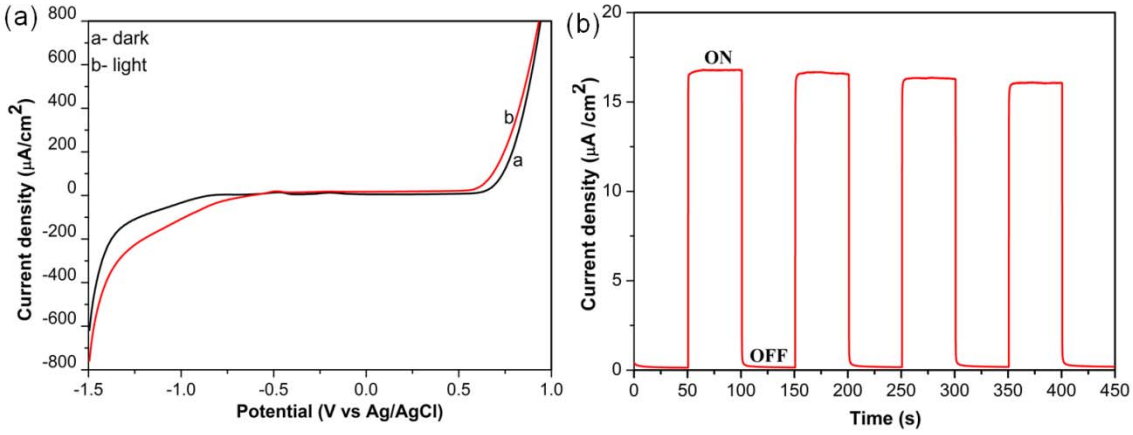

Figure 5.9 *(a) Linear sweep voltammetry characterization of the pristine TiO_2 inverse-opal (288 nm) photoanode, measured both in the dark and simulated sunlight (100 mW cm^{-2}) illumination, (b) amperometric I-t curve vs Ag/AgCl at an applied bias of 0 V and 100 mW cm^{-2} illumination with 50 s light on-off cycles. (Reproduced with permission from Ref. 110; Copyright: John Wiley and Sons 2012)*

The charge transport and transfer processes were investigated using electrochemical impedance spectroscopy (EIS). Figure 5.8e shows the Nyquist plots of the obtained EIS data performed at open-circuit condition under simulated solar light illumination. The diameter of high frequency (> 10^4 Hz) semicircle portion of the curve in the Nyquist plots corresponds to the reduction reaction at the Pt counter electrode. Whereas, the diameter of the second semicircle in the middle frequency range (1~10^3 Hz) indicates the charge

transfer processes occurring at the TiO_2/CdS/electrolyte interface. Using an equivalent circuit with Zsimpwin software, the measured EIS data is fitted well with the diffusion-recombination mode for a porous electrode[38]. With the decreasing pore size, the TiO_2 inverse-opal electrode shows increased charge transfer resistance in the cells with smaller pore sized electrodes. The characteristic frequency peaks in the Bode phase plots as presented in Figure 5.8f can be correlated with the electron life time (τ_n), i.e., $\tau_n = 1/(2\pi f_{max})$. The frequency values decreases with the decrease in pore size, from ~2.6 to ~1 Hz, which suggests a lower recombination occurring in the smaller-pore sized electrode.

5.4 Summary

In this chapter, CdS QDs sensitized, optically and electrically active TiO_2 inverse opals were investigated as a novel nanoarchitectured electrode design for PEC hydrogen production. The highly ordered and percolated 3D pore structures are shown very beneficial for efficient and fast electron transport pathways. A promising IPCE maxima of 30% and photocurrent density of 4.84 mA cm^{-2} has been demonstrated for the 288 nm IO as photoanode at 0 V vs Ag/AgCl bias under simulated solar light illumination. Photocurrent density and IPCE maxima were found to increase with decreasing pore size due to the increase in QDs loading.

Chapter 6

Optical and Electrical Coupling of ZnO Nanowires with TiO_2 Inverse Opals

6.1 Introduction

In the last chapter, CdS quantum dots (QDs) sensitized TiO_2 inverse opals (IO) were applied as a photoanode for photoelectrochemical (PEC) hydrogen production demonstrating a promising photocurrent density of 4.84 mA cm^{-2} with an IPCE maximum of 30% based on 288 nm inverse opals. Increasing the surface area of IO films (by either lowering the pore size or increasing the film thickness) to realize higher QDs loading would further improve light harvesting efficiency. However, this may also contribute to increased charge transfer resistance. One possible way to improve the light harvesting efficiency of TiO_2 IO electrodes is to utilize the spectrally-selective reflectance characteristics of TiO_2 IO electrodes. In this chapter, design of photonic crystal bilayer photoanodes (see Figure 6.1) by coupling TiO_2 IO with 1D ZnO nanowires (NW) is studied in order to improve the light harvesting efficiency through mirrors reflections and light localization within the photoanode. Utilizing photonic crystal optical amplifications, some work has been paid in the past few years to TiO_2 nanoparticle film/photonic crystals bilayer structures to enhance the conversion efficiency of dye sensitized solar cells.[17, 48, 68-70, 115] However, it is still a

great challenge to integrate TiO_2 IO with other nanostructured films with robust electrical contacts and strong optical coupling to realize the dual benefits, i.e. photonic crystal light localizations and photoanode contribution of TiO_2 IO nanostructures.

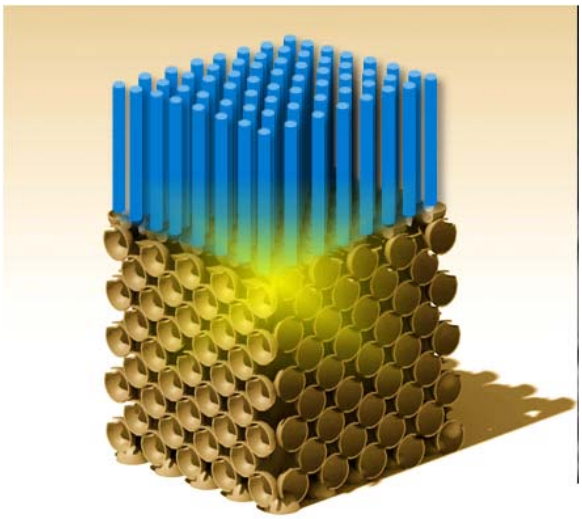

Figure 6.1 *Schematic illustration of bilayer photoanode based on ZnO nanowires coupled TiO_2 inverse opal. (Reproduced with permission from Ref. 114; Copyright: Elsevier 2012)*

1D nanostructures such as nanowires and nanotubes attracted greater attention, as they possess several beneficial characteristics for light harvesting such as direct electron transport paths, shorter carrier diffusion length and lower charge recombinations.[34-40] However, the inadequate specific surface area of the 1D nanostructure in comparison to the nanoparticle electrodes limits the overall energy conversion efficiency to lower levels. Thus, judicious tailoring of the morphology of such 1D nanostructured photoanodes is critical to the further improvement of energy conversion efficiency. The limitation of 1D-based PEC photoanode nanostructures can be addressed by coupling with the optically and electrically active TiO_2 IO photonic crystals, which is expected to enhance the light

harvesting as well as the specific surface area. Mihi *et al*. recently presented a method to transfer IOs onto ZnO nanowires and demonstrated performance enhancement of nanowires for dye-sensitized solar cells through light trapping effect of photonic crystals.[116] However, the efficiency improvement in this work was still limited due to the absence of electrical coupling arising from the lack of physical contacts between the two layers. Considering the low internal surface area of 1D nanostructures, it is essential to couple them with the IO photonic crystals through intimate physical contacts and thereby achieve the dual advantages of light trapping and surface area enhancement.

In this chapter, we present a facile strategy based on atomic layer deposition (ALD) to fabricate high quality semiconductor nanowires/photonic crystals bilayer nanoarchitectures in which ZnO NW are directly integrated atop TiO_2 IOs to achieve both electrical and optical coupling. With appropriately tuned photonic bandgaps by varying the opal size and sensitizing with CdS QDs, such bilayer nanostructures demonstrate a positive optical coupling, in addition to their individual contributions to photocurrents for PEC solar-to-hydrogen generation.

6.2 Experimental Details

Opals were synthesized using the suspensions of monodispersed carboxylate-modified polystyrenes (PS) spheres (Thermo Scientific, with diameters of 200, 250 and 288 nm) via solvent-evaporation-induced convective self-assembly method.[99] Opal templates of all PS sizes were infiltrated by TiO_2 at 70 ^oC using custom designed ALD reactor. Stop-flow ALD process as discussed in chapter 4 was employed to obtain close to theoretical maximum fillings of opal pores by conformal infilling.[117] Further, all the TiO_2 infiltrated

opals were deposited with 70 ALD cycles of ZnO seed layer on the top (~15 nm thickness) at 75 ^{o}C. ZnO NW were grown on the surface of the TiO_2 inverse opals using a standard solution growth method.[102] All the nanostructured photoanodes were sensitized with CdS QDs using modified SILAR method.[40] The PEC performance of the electrodes was measured in a three-electrode configuration using a Potentiostat (CHI760D, CH instrument). Photocurrent stability tests were performed under chopped light irradiation (light-dark cycles of 50 s) at a fixed bias of 0 V vs Ag/AgCl. The incident-photon-to-electron conversion efficiency (IPCE) was measured using a specially designed IPCE system for solar cells (Zolix Solar cell Scan100), with two electrodes configuration under 0 V bias. Detailed description of the experimental methods can be found in chapter 3.

6.3 Results and Discussion

6.3.1 Fabrication and characterization of bilayer photoanodes: Fabrication procedure for ZnO NW coupled TiO_2 IO bilayer structures is schematically illustrated the Figure 6.2.

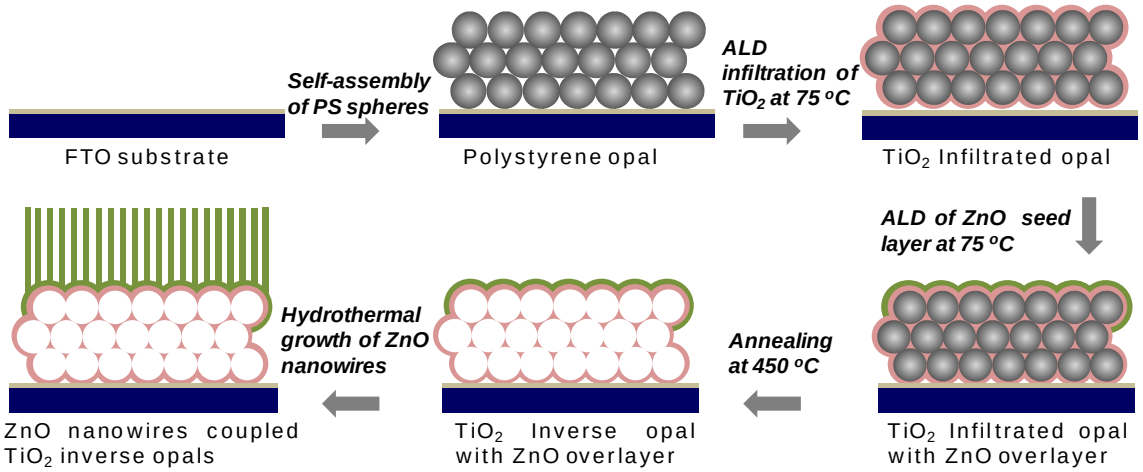

Figure 6.2 *Schematic of the fabrication procedure of bilayer photoanodes in which TiO_2 inverse opal is coupled with ZnO nanowires. (Reproduced with permission from Ref. 114; Copyright: Elsevier 2012)*

Monodispersed PS spheres were first self-assembled on FTO glass substrates to form opal templates as shown in Figure 6.3a. These templates were then infiltrated by TiO_2 using stop-flow ALD until reaching full filling by conformal deposition as discussed in chapter 4. Figure 6.3b shows the tilted FESEM image of the as-infiltrated opal. The conformal and highly controllable ALD growth ensured that the TiO_2 film was deposited conformally on PS spheres with very low roughness. Subsequently, ~15 nm thick ZnO seed layer was deposited using ALD on the top surface of the TiO_2 infiltrated opals. Note here that, due to the full infiltration of TiO_2 in the void spaces of the PS sphere template, the ZnO ALD was restricted only to the top surface of the opal, except for the crack surfaces. The FESEM image in Figure 6.3c indicates the large area surface uniformity after the coating of ZnO seed film. These ZnO seed layer coated infiltrated opals were then calcined at 450 °C to thermally decompose the PS spheres and improve the crystallinity of TiO_2 and ZnO. Finally, ZnO nanowires were grown atop TiO_2 IO using a standard solution growth process. It is noted that the diameters and lengths of the ZnO nanowires can be conveniently tuned by changing the growth reaction conditions. Dense ZnO NW grown over a large area with excellent uniformity can be seen in Figure 6.3d and e. The cross-sectional image in Figure 6.3f confirms the robust interface between the ZnO NW and TiO_2 IO without any pore clogging in the TiO_2 IO layer from ZnO solution growth. The length of ZnO nanowires in this study was maintained at ~2 μm.

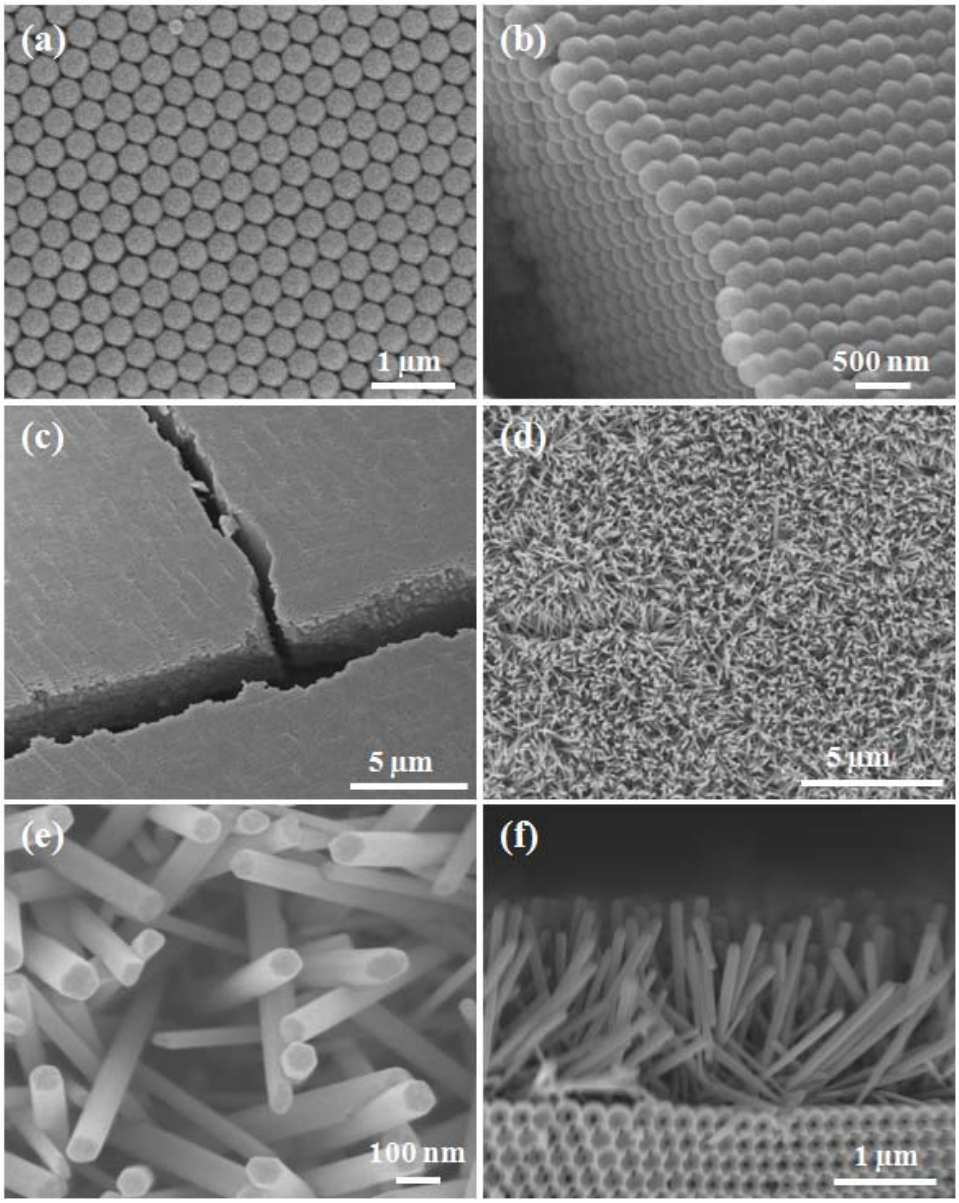

Figure 6.3 *FESEM images of various nanostructures based on 288 nm diameter polystyrene spheres. (a) Top-view of opal, (b) TiO_2 infiltrated opals from 20^o tilted view, (c) TiO_2 infiltrated opal coated with ZnO seed layer atop and (d-f) ZnO nanowires coupled TiO_2 inverse opal bilayer nanostructures: (d) top-view showing ZnO nanowires, (e) magnified view of ZnO nanowires and (f) cross-sectional view of the bilayer nanostructure. (Reproduced with permission from Ref. 114; Copyright: Elsevier 2012)*

The specular reflectance spectra measurements of the photonic nanostructures at various fabrication stages are shown in Figure 6.4. Due to the highly periodic arrangement, the opal based nanostructures exhibits photonic band gaps (PBGs) in (111) direction according to Eq. 5.1.[118] As shown in Figure 6.4, the 288 nm opal exhibits photonic bandgap at 585 nm (curve a), which can be indexed to its Bragg diffraction wavelength position in accordance with Eq. 5.1. The position of the peak is red-shifted to 684 nm (curve b) when infiltrated with TiO_2, due to the increased refractive index. The photonic bandgap positions of the infiltrated opal remained at 684 nm (curve c) even after the deposition of ZnO over layer. This demonstrates the advantage of the ALD method to confine the seed layer and as the subsequent ZnO NW growth, only onto the top surface of the infiltrated opal. After heat treatment at 450 ^{o}C, Bragg peak position blue-shifted to 508 nm (curve d). The Bragg peak of the bilayer nanostructures shifted slightly to 498 nm (curve e) because of the increased structure shrinkage after repeated annealing. Uniform photonic reflective colors across the whole sample area are showed by the corresponding photographs of the samples.

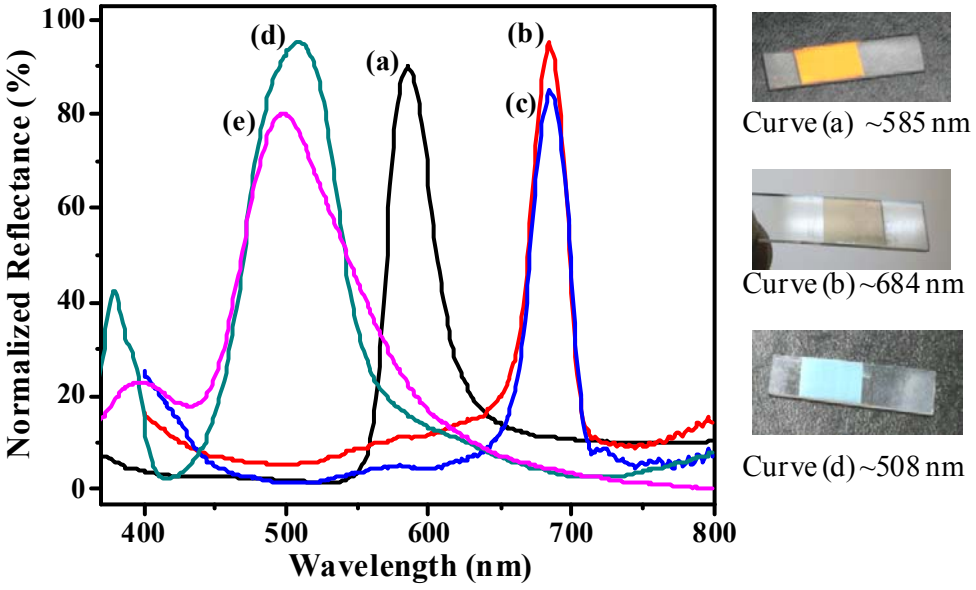

Figure 6.4 *Specular reflectance spectra measured at 20^o to the normal for various nanoarchitectures based on 288 nm diameter polystyrene particles. (a) Self-assembled opal, (b) TiO_2 infiltrated opal, (c) TiO_2 infiltrated opal with ZnO seed layer coated atop, (d) TiO_2 inverse opal and (e) ZnO nanowires coupled TiO_2 inverse opal bilayer nanostructures. Photographs of the three corresponding samples (FTO/glass substrates) are shown on the right side. (Reproduced with permission from Ref. 114; Copyright: Elsevier 2012)*

The bilayer nanostructures were photosensitized with CdS QDs to carry out the investigation as PEC photoanodes. The average IO film thicknesses were measured as 3, 4 and 4.5 μm for 200, 250 and 288 nm diameter TiO_2 IOs, respectively. The FESEM image in Figure 6.5a clearly shows the uniformly coated CdS QDs on the ZnO nanowire surface. The TEM and HR-TEM images (Figure 6.5b and c) further demonstrate the uniform coating of CdS QDs successfully on both ZnO nanowires and TiO_2 IO. The thickness of CdS film is found to be around 8 nm. Good interfacial contact and crystallinity of CdS is confirmed in Figure 6.5d. TEM image of CdS QDs sensitized ZnO nanowire in Figure 6.5e shows that it is imaged in the zone axis [100]. The corresponding electron diffraction (ED) indicates the growth of ZnO nanowires in preferential c-axis (001) direction. The selected area electron diffraction (SAED) patterns in Figure 6.5e reveals hexagonal phase of the adsorbed CdS QD layer and wurtzite phase of ZnO in [100]. This is also confirmed by the simulations which are matched well with the observed ED patterns. XRD measurements (Figure 6.6) also reveal that the crystal structures of ZnO nanowires, TiO_2-IO and CdS QDs as hexagonal, anatase and hexagonal phase, respectively.

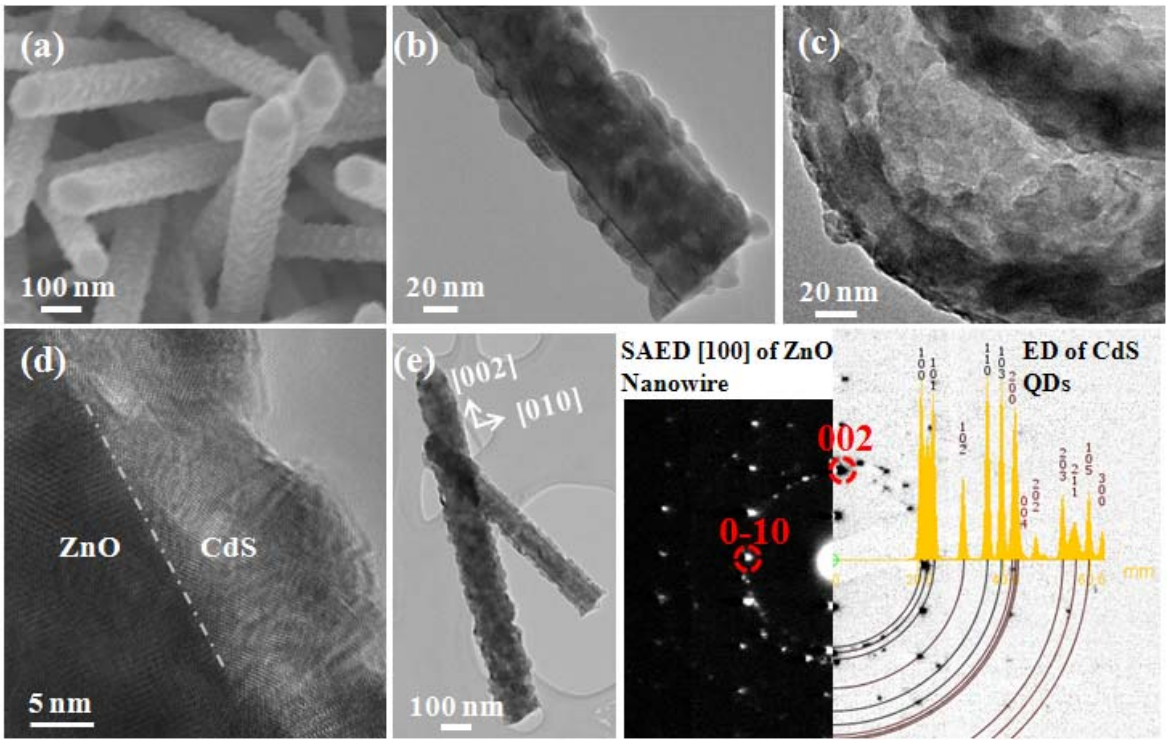

Figure 6.5 *(a) FESEM and (b) TEM images of the CdS QDs coated ZnO nanowires. (c) TEM image of CdS QD sensitized 288 nm void size TiO_2 inverse shells, (d) HRTEM image of ZnO nanowire and CdS film interface and (e) electron diffraction (ED) analysis of the CdS QDs coated ZnO nanowires. The simulated ones are shown in correspondence with the observed electron diffraction patterns (red refers to ED pattern of ZnO; rings refer to CdS QDs). (Reproduced with permission from Ref. 114; Copyright: Elsevier 2012)*

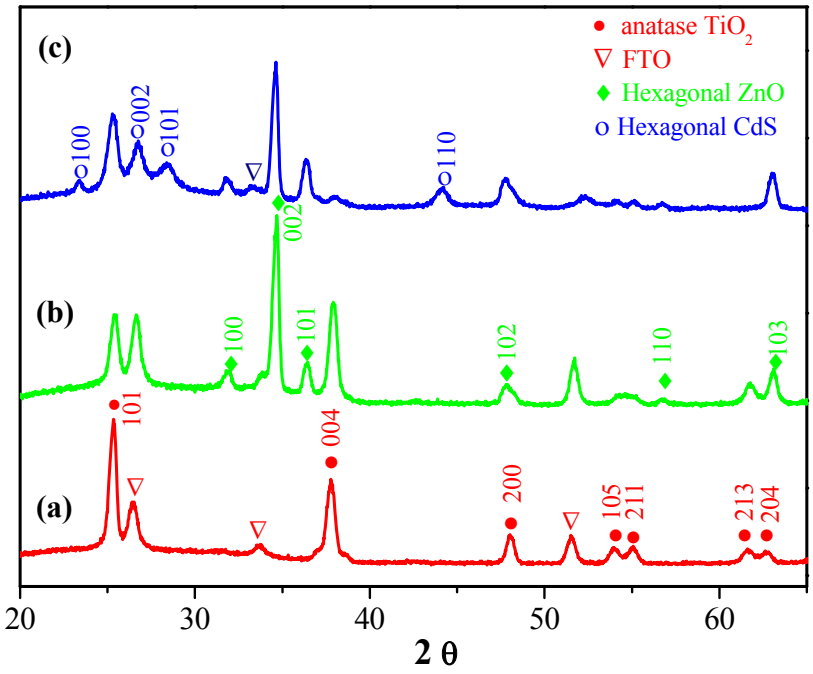

Figure 6.6 *X-ray diffraction patterns for (a) TiO_2 inverse opal (b) ZnO nanowires coupled TiO_2 inverse opal and (c) CdS QDs sensitized ZnO nanowires coupled TiO_2 inverse opal. (Reproduced with permission from Ref. 114; Copyright: Elsevier 2012)*

6.3.2 Photoelectrochemical performance measurements: The PEC performance of the photoelectrodes was evaluated in a three-electrode configuration with front-side illumination.[119] Current density vs potential measurements measured from different photoanodes in both dark and simulated one Sun illumination are shown Figure 6.7a. As expected, all the electrodes show very low dark currents. Upon light illumination, higher photocurrents from all the photoanodes are evident in the range of -0.5 to +0.75 V. The highest photocurrent density of ~5 mA/cm^2 at +0.75 V is observed for 250 nm opal size bilayer photoanode, which is twice that of the photoanode based on single-layer ZnO NW. No saturation of photocurrents is observed in all the bilayer electrodes, demonstrating efficient charge separation upon illumination. The amperometric *i-t* curves (Figure 6.8) shows that all the electrodes possess fast photoresponse and good photostability.

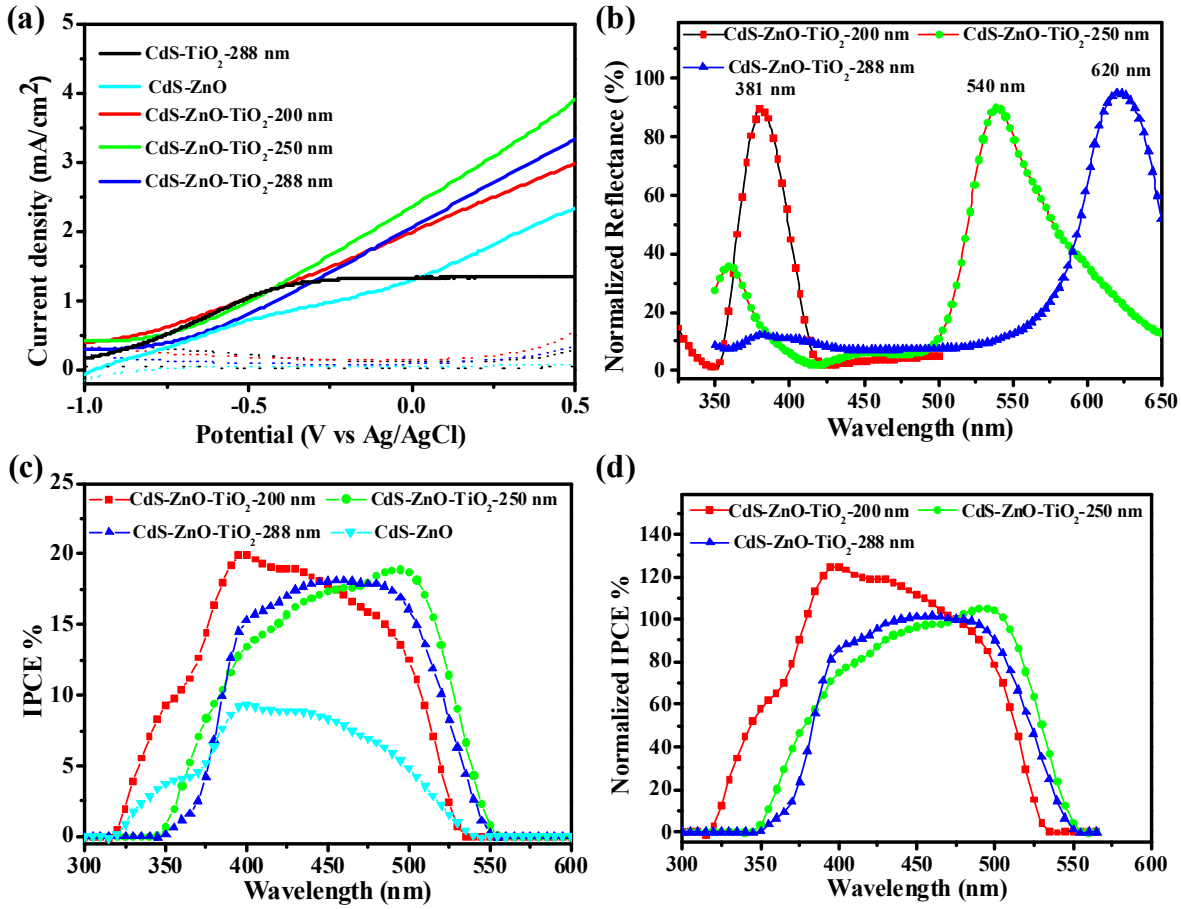

Figure 6.7 *(a) Linear sweep voltammetry measurements of different photoanodes both in the dark and simulated sunlight illumination (100 mW cm^{-2}). Here, the measurements under light are indicated by solid lines while dark measurements are indicated by dotted lines. (b) Specular reflectance spectra measurements of the various bilayer photoanodes after QDs sensitization and electrolyte infiltration. The photonic bandgap positions of the 200, 250 and 288 nm diameter TiO_2 inverse opal films are shown on top of the curves. (c) IPCE spectra for different photoanodes. (d) IPCE spectra normalized at 475 nm. (Reproduced with permission from Ref. 114; Copyright: Elsevier 2012)*

The photocurrent improvements due to the TiO_2 IO layer can be attributed to its dual role. First, the TiO_2 IO films acting as a "dielectric mirror" can diffract part of the incoming light transmitted through the ZnO NW film, resulting in an increased optical path

and improved light absorptions. Second, the electrically active CdS-sensitized TiO_2 IO layer can also partly harvest the non-reflected light and contribute to the photocurrent improvements. After the QDs sensitization and sulfide electrolyte infiltration, the 200, 250 and 288 nm diameter TiO_2 IO films exhibit their stop band peaks at 381, 540 and 620 nm, respectively (see Figure 6.7b). For the bilayer photoanode based on 288 nm TiO_2 IO, it can be observed that the photonic stopband is formed outside the region of CdS QD absorptions. In order to clarify the role of photoanode contributions of IO films in the bilayer structure, the PEC performance can be compared for single layer of ZnO NW photoelectrode, single layer of 288 nm TiO_2 IO photoelectrode and their corresponding bilayer photoelectrode. The photocurrent density values are 1.3, 2.3 and 3.25 mA/cm^2 at +0.5 V for single layer 288 nm TiO_2 IO electrode, single layer ZnO NW electrode and their corresponding bilayer electrode, respectively as shown in Figure 6.7a. The significant improvement of photocurrent density for the bilayer photoelectrode in comparison to both the single layered electrodes confirms the electrical coupling of two films in the bilayer structure.

Incident photon to electron conversion efficiency (IPCE) measurements were carried out as shown in Figure 5c to further reveal the wavelength dependent light harvesting ability of the bilayer photoanodes. The bilayer photoanodes based on 200 nm and 250 nm TiO_2 IO films exhibit enhancement in their respective photonic stop band the zones. The IPCE spectra are normalized at 475 nm to better understand the photonic bandgap effect by normalizing the role of surface area for different photoanodes. The normalization bilayer photoanodes is performed at 475 nm to eliminate the interference of photonic reflections and ensure the accuracy of surface area normalization. It is known that the photonic

crystals can increase the optical path length of the photons in the nanostructure through back reflections and wide angle scattering of light wavelength.[115] At 405 nm, bilayer photoanode based on 200 nm TiO_2 IO film presents the highest IPCE values as shown in Figure 6.7d, which is 46% higher in comparison to that of photoanode based on 250 nm TiO_2 IO films, for which no observable photonic bandgap features are present at this wavelength. At the same wavelength, bilayer photoanode based on 288 nm TiO_2 IO film exhibits 11% enhancement due to the presence of higher order photonic bandgaps. For photoanode based on 200 nm TiO_2 IO films, the photocurrent enhancement is extended over a wide wavelength region overlapped with the red-edge of its bandgap till 450 nm. This enhancement outside the region of stop band can be attributed to the slow-photons effect in the IO.[48] In the same way, bilayer photoanode based on 250 nm TiO_2 IO film shows 20% higher IPCE value at 495 nm in comparison to that of photoanode based on 250 nm sized TiO_2-IO films due to the partial overlap of its photonic bandgap with the absorption edge. This improvement demonstrates that photonic light trapping is very effective to enhance the longer wavelength absorption of the CdS sensitizer with low extinction coefficient.

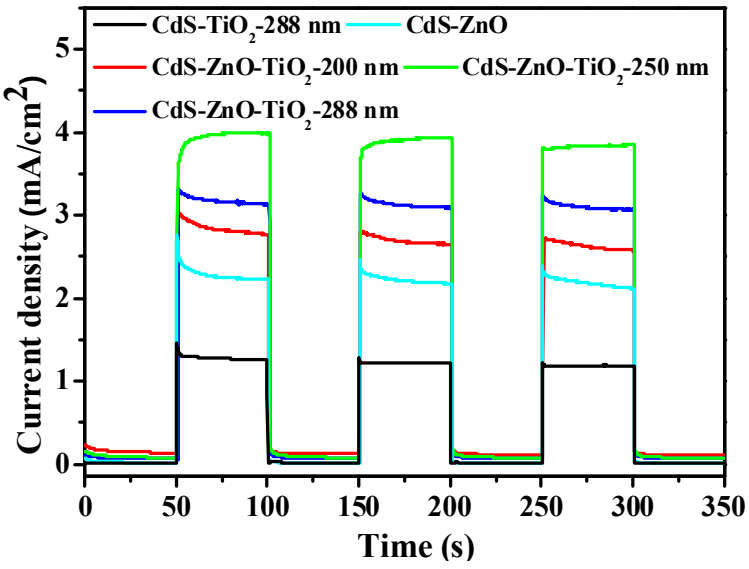

Figure 6.8 *Amperometric i-t curves for the photoanodes based on different configurations measured at an applied bias of 0.5 V under simulated sunlight illumination (100 mW cm^{-2}) with 50 s light on/off cycles. (Reproduced with permission from Ref. 114; Copyright: Elsevier 2012)*

6.4 Summary

In summary, a simple strategy based on ALD is demonstrated to couple the ZnO nanowire (NW) with IO structures towards improved PEC solar energy harvesting. FESEM, TEM and optical characterizations further confirmed that the bilayer nanostructures possess robust physical contacts, high crystallinity and well-defined morphological features. As the wide range of materials for both the nanowires and IO are available, our strategy based on ALD offers a new approach to the fabrication of various nanowires-photonic crystal coupled structures for diverse applications.

The PEC performance investigations of the CdS QDs sensitized ZnO NW/TiO_2-IO bilayer nanostructures as photoanode showed greatly improved photocurrents in comparison to that of single layer ZnO NW photoanode, which is attributed to positive

coupling effects from the TiO_2 IO layer, i.e, light harvesting enhancement through back reflections and slow-photon effect, as well as increased surface area for sensitizer loading. The length (~2 μm) of the ZnO NW in this bilayer photoanode demonstrated in this work is relatively low, so that light harvesting enhancement due to the increased optical path might be limited. Further tuning of the length of nanowires and position of the photonic bandgaps may enable higher conversion efficiencies.

Chapter 7

Three-Dimensional Hierarchical Integration of ZnO Nanowires with TiO_2 Inverse Opals

7.1 Introduction

To achieve highly efficient photoelectrochemical (PEC) cells, nanostructured photoanode should possess several favourable intrinsic characteristics such as adequate specific surface area to permit higher photosensitizer loading, direct electron transport pathways for longer electron diffusion length and light scattering to promote the light harvesting ability by confining the light within the cell.[42-45] It is thus highly desirable to develop the photoanode that meet all the above requirements. Towards this objective, we demonstrated in the previous chapter three-dimensional (3D) inverse opal (IO) based nanostructures possessing highly ordered interconnected shells, high porosity and photonic crystal light localization as very promising for PEC cells.[17, 46-52] Highest IPCE of 30% and 20% have been realized based on quantum dots (QDs) sensitized TiO_2 IO and ZnO nanowires coupled TiO_2 IO bilayer photoanodes, respectively.[46, 49] The promise of these 3D IO photoanodes can be further fulfilled when the substantial proportion of pore volume (~75%) is carefully exploited to resolve the issue of surface area shortage.

In this chapter, we demonstrate a novel nanoarchitecture consisting of 3D ordered hierarchical nanobushes, using TiO_2 IO on Fluorine-doped SnO_2 (FTO) glass substrate as the host template for the facile solution growth of ZnO nanowire networks. The TiO_2 IO-ZnO nanowire hybrid nanostructure is sensitized with CdS QDs and studied as the PEC photoanode. The key idea here is to hierarchically integrate the ZnO nanowires with the TiO_2 IO using ALD to achieve higher sensitizer loading and contact interface area with the electrolyte and enhanced light scattering.

7.2 Experimental Details

Carboxylate-modified, monodispersed polystyrene (PS) particles of 500 nm diameter purchased from Duke scientific corporation were self-assembled onto the FTO coated glass substrates via a vertical deposition method.[121] Afterwards, the self-assembled opals were infiltrated with TiO_2 using a self-made stop-flow-reactor type of ALD system as described in chapter 4. Finally, TiO_2 IO structures were developed by thermally decomposing original polystyrene spheres template at 450 °C for 2 h. A conformal ZnO seed layer of ~10 nm thickness (50 cycles of ALD) was coated on the internal surface of TiO_2 inverse opals using ALD. Subsequently, ZnO nanowires were grown based on the conformably deposited ZnO seed layer within the IO structure using a standard solution growth method.[102] All the nanostructured electrodes on FTO glass were photosensitized with CdS QDs under the same experimental conditions using a modified SILAR route.[40] The PEC performance of the photoanodes was measured in a three-electrode configuration using a Potentiostat (CHI760D, CH instrument). Photocurrent stability tests were performed under chopped light irradiation (light-dark cycles of 50 s) at a fixed bias of 0 V vs Ag/AgCl. The

incident-photon-to-electron conversion efficiency (IPCE) was measured using a specially designed IPCE system for solar cells (Zolix Solar cell Scan100), with two electrodes configuration under 0 V bias. Detailed description of the experimental methods can be found in chapter 3.

7.3 Results and Discussion

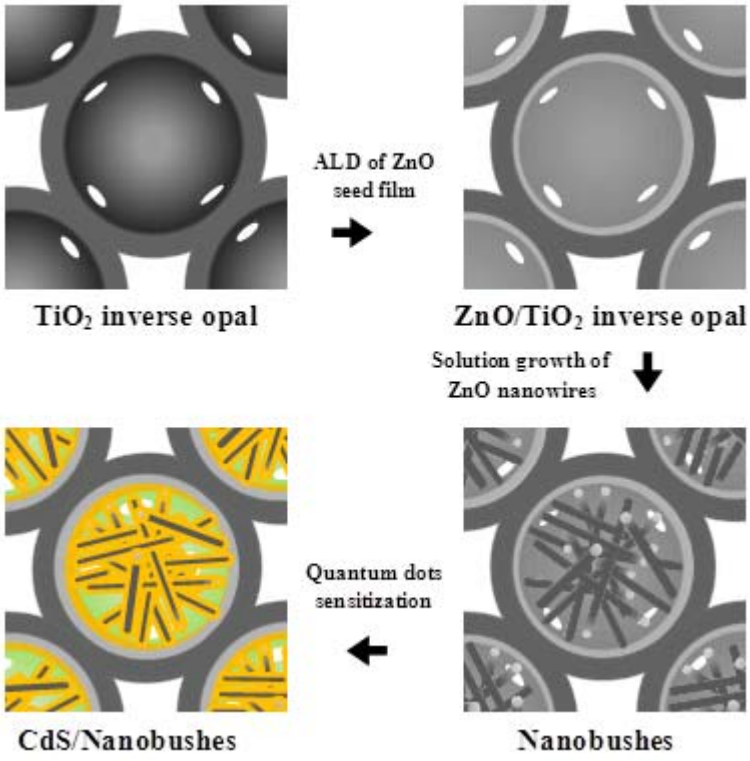

Figure 7.1 *Schematic illustration of fabrication procedure for nanobushes photoanode. (Reproduced with permission from Ref. 120; Copyright: John Wiley and Sons)*

7.3.1 Nanostructure fabrications and microstructural characterizations: Figure 7.1 outlines the fabrication procedure for the nanobushes photoanode. First, self-assembled opal templates with close packed *fcc* structure were developed and infiltrated with TiO_2 ALD with close to full infiltrations. After heat treating the infiltrated opal templates, TiO_2

IOs were obtained as shown in Figure 7.2a, b. The obtained TiO_2 IOs of ~6 μm thickness were coated with ~10 nm thick conformal ZnO film which serves as the seed layer for subsequent solution growth of ZnO nanowires, forming a 3D ordered nanobushes structure. Nanowire diameter and length are controlled through the optimization of growth conditions.

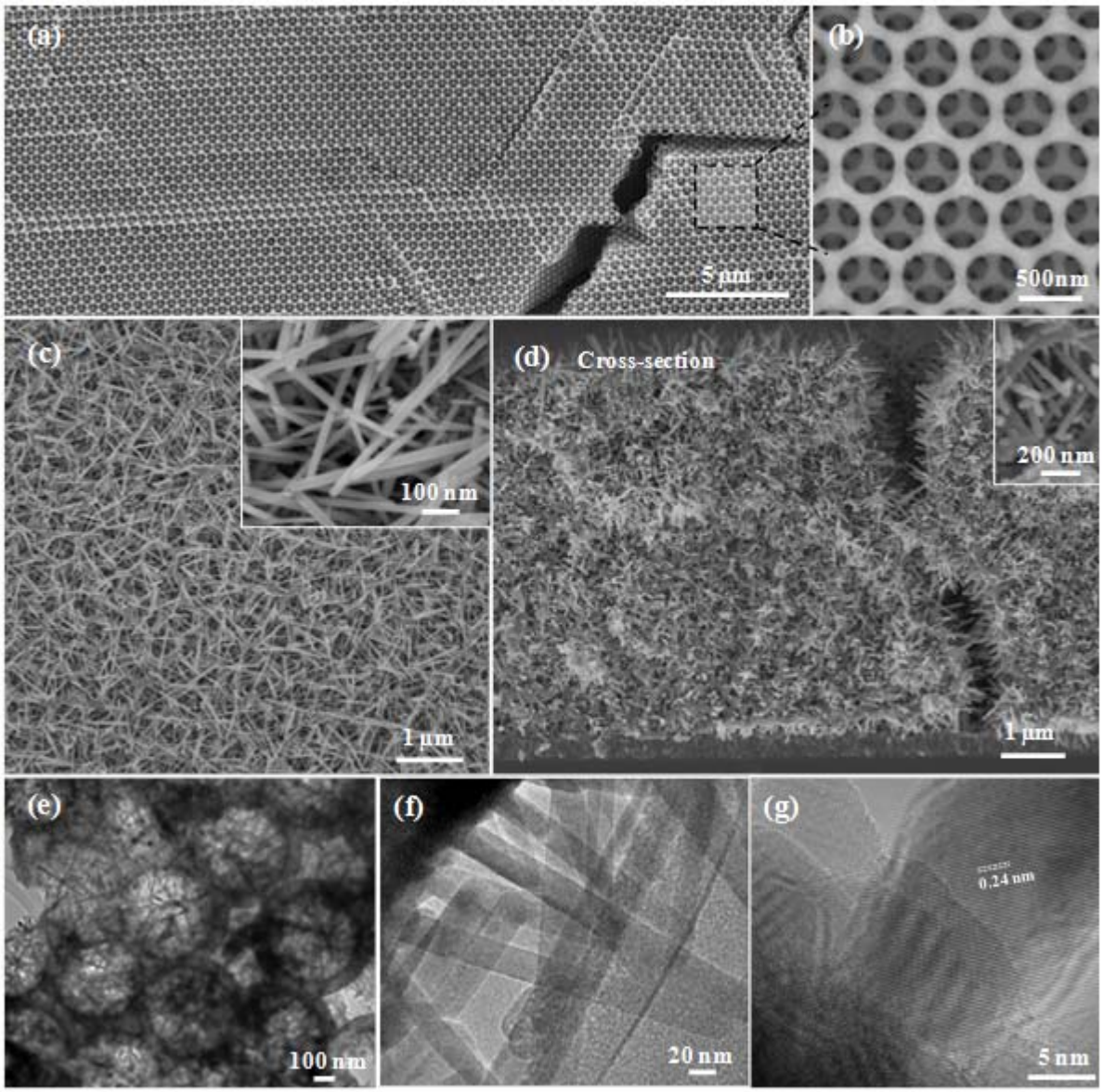

Figure 7.2 *FESEM images of (a, b) top-view of TiO_2 inverse opal at different magnifications, (c, d) nanobushes structure; (c) top view and (d) cross-sectional view. The magnified top view and cross-sectional view of a nanobush structure are shown in the insets of (c, d), respectively. (e-g) TEM images showing nanobushes structure at different magnifications. (Reproduced with permission from Ref. 120; Copyright: John Wiley and Sons)*

Top-view FESEM image in Figure 7.2c shows the resulting nanobushes structure after 9 h solution growth of ZnO nanowires. Inset of Figure 7.2c shows FESEM image of single nanobush within an IO pore at higher magnification, which comprises of multiple number of ZnO nanowires randomly aligned with in TiO_2 shells covering the entire pore space. Figure 7.2d shows the cross-sectional view of the nanobushes structure confirming the hierarchical organization of nanobushes. This kind of 3D hierarchical growth of nanobushes is noticed in the entire high aspect ratio IO template. Although the growth of 9 h was used herein to achieve the longest nanowires based on 500 nm diameter IO films, the wire length can be conveniently controlled by changing the reaction conditions. Moreover, size of the nanobushes can also be modulated by simply changing the pore size as exemplified in Figure 7.3.

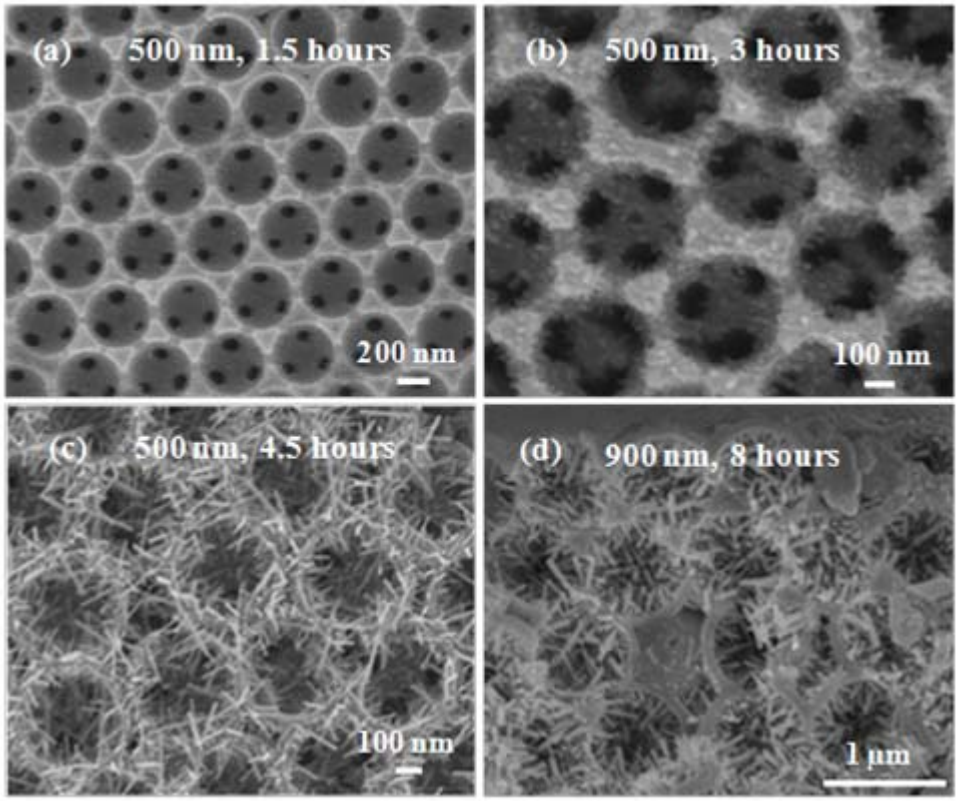

Figure 7.3 *FESEM images of (a-c) top-view of TiO_2 inverse opals based on 500 nm polystyrene spheres with ZnO nanowires grown; (a) 1.5 hrs of solution growth, (b) 3 hrs of solution growth and (c) 4.5 hrs of solution growth, (d) cross-section of TiO_2 inverse opals based on 900 nm polystyrene spheres with 8 hrs solution growth of ZnO nanowires.* *(Reproduced with permission from Ref. 120; Copyright: John Wiley and Sons)*

The nanoscale features of the nanobushes were further scrutinized using TEM. Figure 7.2e shows the dense growth of nanobushes in the IO template. From Figure 7.2f, the diameter of the nanowires can be estimated as ~30 nm. At higher magnification, Figure 7.2g reveals the interface between the nanowires and IO shells. Crystallinity of the ZnO nanowires can be confirmed as hexagonal from the inter-plane spacing (0.24 nm) that matches with the d-spacing of (101) plane. Generally, one disadvantage inherent to the growth of vertically aligned ZnO nanowires on flat substrates is the fusion of nanowires at

their roots which limits the optical transparency of the nanostructured films.[122] Hierarchical growth of ZnO nanowires in case of nanobushes seemingly eliminated this issue. In addition, the interfacial surface area of nanobushes can be easily adjusted by tuning diameters of the PS spheres and extending thickness of opal templates, which fulfills the high interfacial area requirement (see appendix A1) for PEC cells.

7.3.2 Optical characterizations: Originating from the highly periodic arrangement, TiO_2 IOs exhibits photonic bandgaps, where the propagation of light of certain wavelengths is prohibited. TiO_2 IOs possess pseudo photonic bandgaps centered at 934 nm (Figure 7.4a (i)) and low intense higher order bands in the visible wavelengths (~450 nm). After growing the ZnO nanowires to form nanobushes, peak wavelength position red-shifted to 1086 nm (Figure 7.5 (iii)) because of the increased index from the growth of ZnO nanowires. The exhibition of photonic bandgaps even after the growth of ZnO nanowires confirms that the long range structural order is preserved. Considering the general interest in optical properties of ZnO nanowires, it is anticipated that nanobushes may be useful in various optoelectronic applcations.[123, 124]

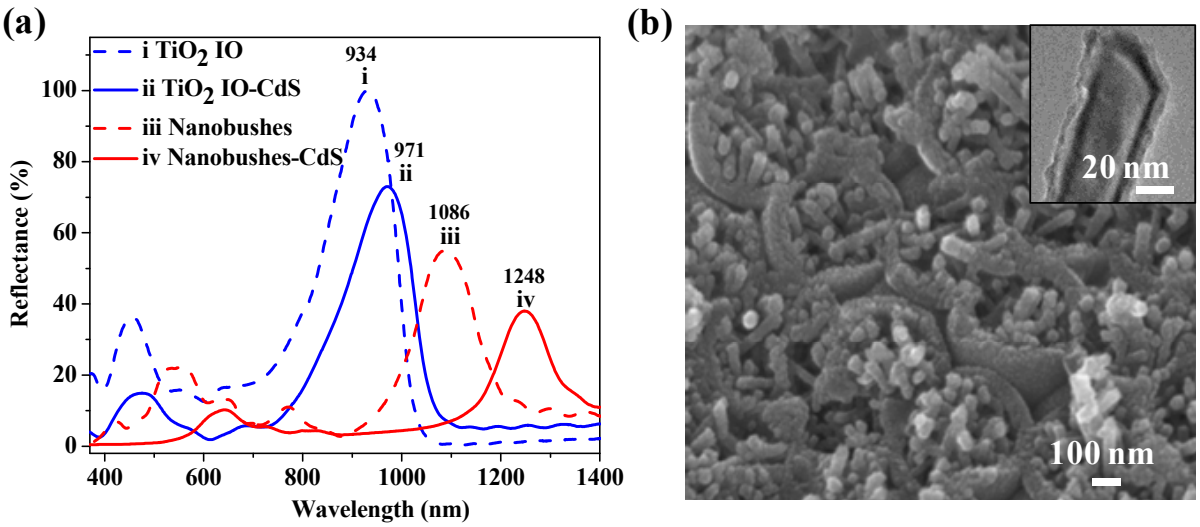

Figure 7.4 *(a) Specular reflectance spectra of i) TiO_2 inverse opals, ii) CdS QDs sensitized TiO_2 inverse opals, iii) nanobushes and iv) CdS QDs sensitized nanobushes, (b) FESEM image of cross-section of CdS QDs sensitized nanobushes structure; inset of (b) shows the HRTEM image of a single nanowire from nanobushes structure sensitized with CdS. (Reproduced with permission from Ref. 120; Copyright: John Wiley and Sons)*

Photosensitization with CdS QDs was carried out for the three nanostructured photoanodes, namely, TiO_2 IO, ZnO/TiO_2 nanobushes and ZnO nanowires to comparatively investigate the PEC performance. The thickness for all the nanostructured photoanodes was maintained at ~6 μm (Figure 7.4). Photonic bandgap of the photoanodes after the CdS sensitization are shown by curves ii and iv in Figure 7.5a. Photonic bandgap shift by 162 nm and 37 nm can be noticed for the nanobushes and TiO_2 IO, respectively. The loading amount of CdS QDs increased for nanobushes by several times due to the greatly increased specific surface from the networks of nanowires within each pore. Cross-sectional image of QDs sensitized nanobushes photoanode in Figure 7.5b shows the distinct CdS/ZnO core-shell nanowires without any aggregation. Interconnected TiO_2 shells that facilitate the direct electron transport can also be noticed. From the inset in Figure 7.5b, CdS QDs of ~7 nm coated on the entire ZnO nanowire in the nanobush structure is observed.

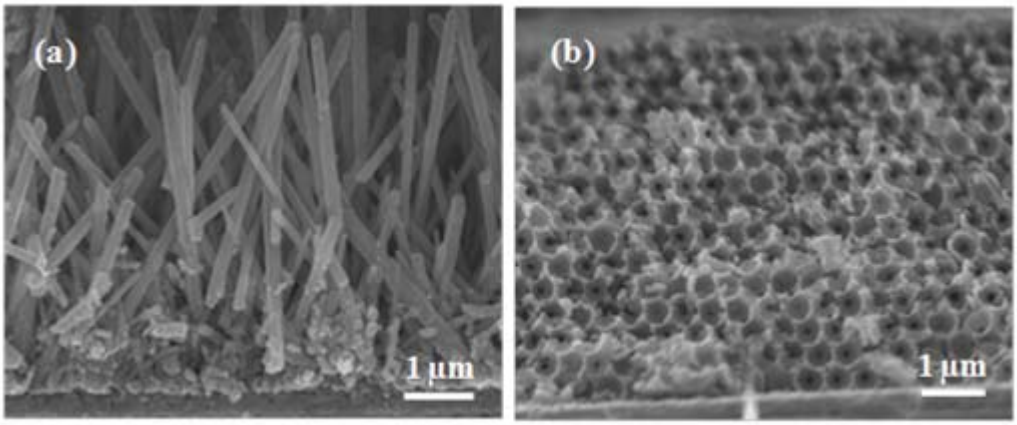

Figure 7.5 *(a, b) Cross-sectional FESEM images of (a) CdS QDs sensitized ZnO nanowires and (b) CdS QDs sensitized TiO_2 inverse opals. (Reproduced with permission from Ref. 120; Copyright: John Wiley and Sons)*

The light scattering ability of different electrodes is investigated using the UV-Vis diffuse reflectance measurements before (Figure 7.6a) and after (Figure 7.6b) CdS QDs photosensitization. In case of pristine nanostructures without CdS, the highest scattering was observed in nanobushes, closely followed by TiO_2 IO. As the Mie scattering arises from the particles with the diameters comparable to the wavelength of the incident light, void size of IO in this work (~500 nm) contributed towards strong visible photon scattering.[125] This result demonstrates the advantages of the 3D structured photoanodes over the 1D ZnO nanowires. Previous studies reported that disorder in photonic crystals increases the broadband diffuse scattering.[66, 126, 127] The higher disorder in the nanobushes from the growth of ZnO nanowires may have contributed to the higher diffuse scattering in comparison to IO films. Typically, all the nanostructured photoanodes after CdS QDs sensitization exhibit lower diffuse reflectance up to 550 nm due to the strong light absorption by CdS QDs. It is worth noting that nanobushes photoanode presents lowest diffuse reflectance in after sensitization. This can be attributed to the much higher loading

of CdS anchored to the ZnO nanowire networks in comparison to TiO_2 IO-CdS, promoting stronger absorption of the scattered light. Moreover, presence of higher order bands for TiO_2 IO-CdS photoanode (Figure 7.4a (ii)) cab be reasoned towards higher specular reflections.

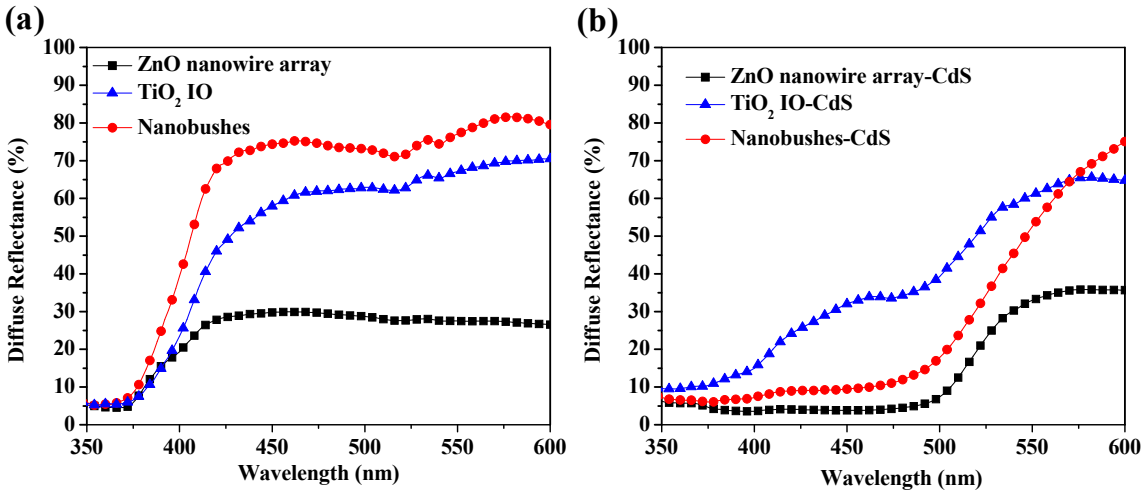

Figure 7.6 *(a, b) UV-Vis diffuse reflectance spectra; (a) before CdS QDs sensitization and (b) after CdS QDs sensitization. Strong light scattering exhibited by the 3D photoanodes is expected to increase the path length travelled by the light within the photoanode and thus the PEC light harvesting.*[45, 125] *(Reproduced with permission from Ref. 120; Copyright: John Wiley and Sons)*

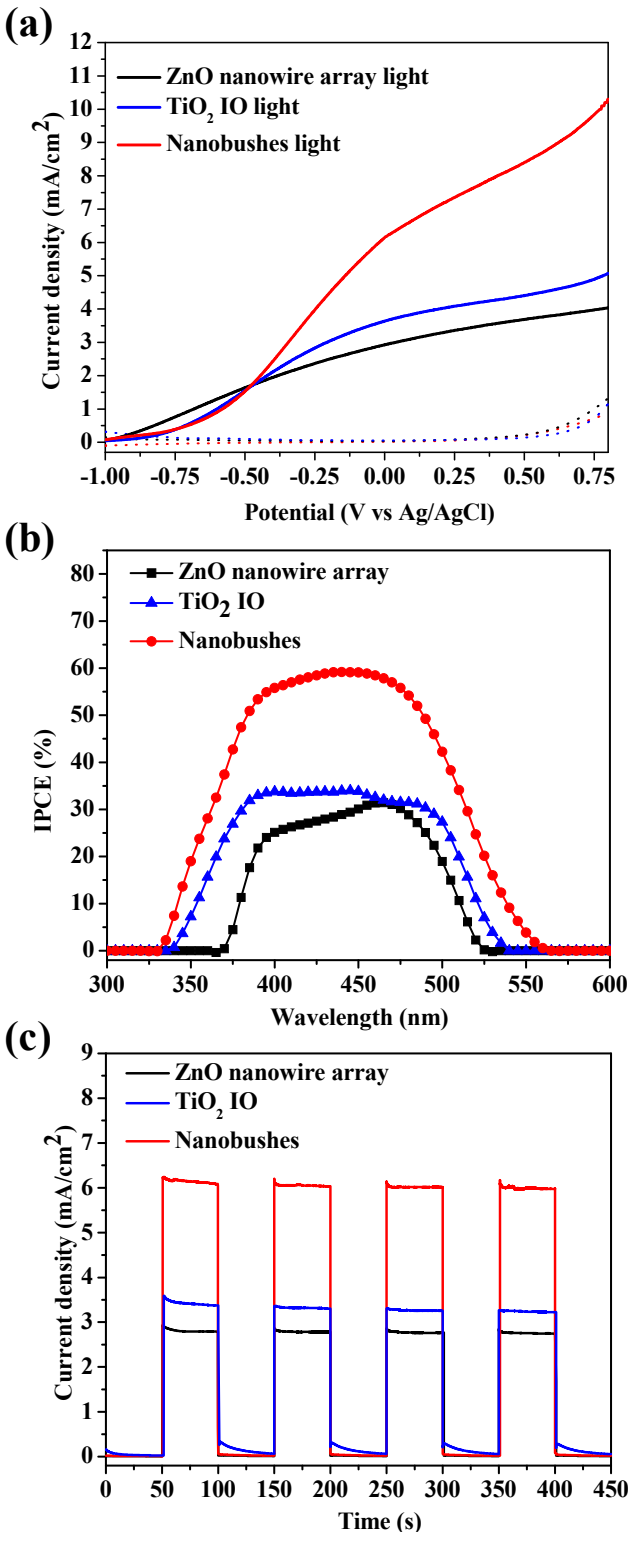
(a)
ZnO nanowire array light
TiO2 IO light
Nanobushes light
Current density (mA/cm2)
Potential (V vs Ag/AgCl)
(b)
ZnO nanowire array
TiO2 IO
Nanobushes
IPCE (%)
Wavelength (nm)
(c)
ZnO nanowire array
TiO2 IO
Nanobushes
Current density (mA/cm2)
Time (s)

Figure 7.7 *(a) Linear sweep voltammetry characterizations of different photoanodes; dotted lines indicate the measurements collected in dark while the solid lines represent the measurements taken under simulated sunlight illumination (100 mW cm^{-2}), (b) IPCE spectra and (c) Amperometric I-t curves vs AgCl/Ag at an applied potential of 0 V under 100 mW cm^{-2} simulated sunlight illumination with 50 s light on/off cycles. (Reproduced with permission from Ref. 120; Copyright: John Wiley and Sons)*

7.3.3 Photoelectrochemical performance measurements: The current density vs potential (I-V) measurements were conducted under the dark and simulated sunlight illumination to evaluate the PEC performance of different photoanodes. All the nanostructured photoanodes exhibit evident photocurrent density after illumination, manifesting efficient light absorptions and charge separation. All the photoanodes presents same onset potential with gradually increasing current density with increasing bias voltage. The current density for nanobushes photoanode reached 6.2 mA cm^{-2} at 0 V vs Ag/AgCl, which is very high in comparison to 3.6 and 2.9 mA cm^{-2} for the single layer nanostructured photoanodes based on TiO_2 IO and ZnO nanowires, respectively.

To investigate the spectral light harvesting efficiency of different photoanode structures, IPCE measurements for all the three photoanodes were carried out in the wavelengths ranging from 300 nm to 600 nm as shown in Figure 7.7b. Strong photoactivity is noticed for all the photoanodes in the visible wavelengths. In comparison to the ZnO nanowires, both the 3D structured photoanodes presents broader photoresponse indicating the beneficial role of light scattering to improve the light harvesting. IPCE maxima for nanobushes and ZnO nanowires can be determined to be 60% and 30% respectively at the wavelength of around 460 nm. IPCE maxima of 60% emphasize the great potential of the nanobushes for PEC cell applications considering the transmission losses through FTO and

the PEC cell. To our knowledge, this represents the highest performance for CdS QDs coated TiO_2 photoanodes. For the TiO_2 IO photoanode, the maxima IPCE of 36% can be measured at around 405 nm with almost flat profile in the photoactive region. This can be attributed to the reflection light losses at wavelengths above 420 nm due to the presence of higher order reflective bands (see Figure 7.4a (ii)). IPCE measurements for all the nanostructured photoanodes are also consistent with their corresponding photocurrent density measurements as in Figure 7.7a. Amperometric *I-t* curves in Figure 7.7c show the fast photoresponse and good photostability for all the photoanodes. Moreover, the conformal ZnO ALD film deposited on the electron transporting TiO_2 inverse shells may act as an energy barrier which suppresses the recombination of photoinjected electrons and redox ions of the electrolyte, thereby contributing to the improved the performance for nanobushes photoanode.[46, 128, 129]

7.4 Summary

We demonstrated for the first time a fabrication strategy to hierarchically integrate dense networks of ZnO nanowires with TiO_2 inverse opals to form 3D ordered nanobushes. Justified by several favorable attributes such as high specific surface area, direct electron transport networks and strong light scattering, the promise of the novel nano-hierarhicial photoanode is unambiguously demonstrated for PEC cells based on CdS QDs sensitization. A photocurrent density of 8.3 mA cm^{-2} at + 0.5 V vs Ag/AgCl under AM1.5 simulated solar light illumination is achieved, which is the highest reported value for CdS sensitized TiO_2 nanostructured photoanodes for PEC hydrogen generation.

Chapter 8

Conclusions and Recommendations

8.1 Conclusions

Controlled infilling of opal templates with close to theoretical fillings was demonstrated using stop-flow atomic layer deposition (ALD). It was observed that the deposition in opal templates is limited by the Knudsen flow of precursor gases into the nanostructure templates in contrast to the surface reaction limited deposition on flat surfaces. Stop-flow process enabled the high aspect ratio deposition with cycle time an order of magnitude lower in comparison to that of continuous-flow process. Investigation of the effect of kinetic parameters such as fill pressure, hold time and purge time on homogeneity of the template infiltrations showed that optimum process window for these parameters is required to eliminate unwanted chemical vapor deposition reactions and premature pore blocking.

The high quality TiO_2 inverse opals of different pore sizes (288 nm, 510 nm and 900 nm) developed using ALD were photosensitized with CdS quantum dots (QDs) and applied as a photoanode for visible light driven photoelectrochemical (PEC) hydrogen generation. Interconnected pore structure of inverse opal (IO) enabled the uniform CdS QDs coating and close interfacial contacts with the electrolyte throughout the entire thickness of the photoanode. Controlled and conformal template infilling using stop-flow ALD enabled the synthesis of high quality IO nanostructures with superior electron transport properties for

PEC cell applications. Fast photoresponse and good photostability for the IO photoanodes of all the pore sizes was observed. A promising photocurrent density of 4.84 mA cm^{-2} and a IPCE maxima of 30% was demonstrated for the 288 nm IO (~6 μm thickness) as photoanode at 0 V vs Ag/AgCl bias under simulated solar light illumination. Photocurrent density and IPCE maxima were found to increase with decreasing pore size due to the increase in QDs loading. However, charge transfer resistance was observed to increase with decreasing pore size.

To improve the light absorptions in the photoanode, a bilayer photoanode was fabricated by coupling the ZnO nanowires on top of TiO_2 inverse opal. Successful electrical and optical coupling has been established by confining the ZnO seed film (~15 nm thickness) and the subsequent ZnO nanowires growth atop of TiO_2 infiltrated opals using ALD. The PEC performance of the CdS QDs sensitized ZnO nanowires coupled TiO_2 IO bilayer nanostructure as photoanode showed greatly improved photocurrents in comparison to that of single layer ZnO nanowires and single layer of TiO_2 IO photoanodes, which is attributed to positive coupling effects from the TiO_2 IO layer, i.e. light harvesting enhancement through back reflections and slow-photon effect, as well as increased surface area for sensitizer loading.

Finally, a fabrication strategy was designed to hierarchically integrate the ZnO nanowires with the TiO_2 IO to form novel nanobushes structures using ALD to address the high surface area requirements. A comparative PEC performance study demonstrated the promise of the nanobushes photoanode for photoelectrochemical cells as supported by greatly improved specific surface area and strong light scattering. An IPCE maxima of ~ 60% and a photocurrent density of 8.3 mA cm^{-2} at + 0.5 V vs Ag/AgCl under AM1.5

simulated solar light illumination was realized using nanobushes photoanode. These results established high quality three-dimensional IO based nanostructures developed using ALD as promising material platform for PEC solar energy harvesting.

8.2 Recommendations

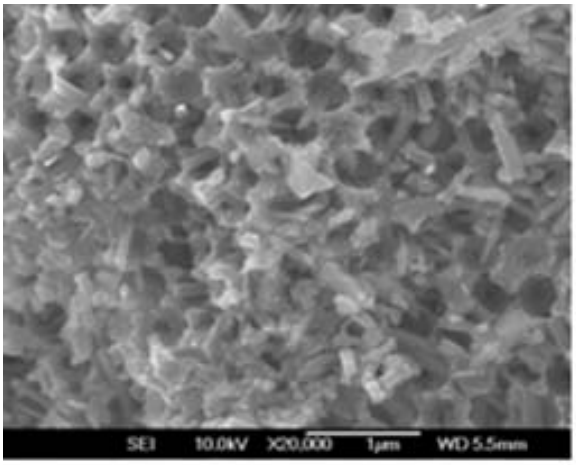

Figure 8.1 *FESEM image showing the growth of TiO_2 nanowires inside TiO_2 inverse opals using hydrothermal synthesis method.*

8.2.1 Hierarchical integration of TiO_2 nanowires with TiO_2 inverse opals: In chapter 7, we showed that hierarchical integration of ZnO nanowires with TiO_2 inverse opals to form nanobushes promotes the surface area of the nanostructures comparable to that of mesoporous nanoparticles films while retaining the beneficial attributes of the three-dimensional IO nanostructures. Further, heterojunctions of ZnO/TiO_2 can be eliminated by integrating TiO_2 nanowires with TiO_2 IO which will in turn lower the charge transfer resistance and reduce the charge recombinations. In our preliminary experiments, we carried out the growth of TiO_2 nanowires inside the IO with partial success as shown in

Figure 8.1. The diameter of the TiO_2 nanowire by hydrothermal growth was more than 100 nm. The growth of TiO_2 nanowires in hydrothermal method is harder to control compared to that of ZnO nanowires growth, usually in strong acidic conditions. Further efforts in this direction should be continued by systematic investigation of the growth parameters to control the dimensions of TiO_2 nanowires inside TiO_2 inverse opals.

8.2.2 ALD based photosensitization of three-dimensional nanostructures: Photosensitization of nanostructures using CdS QDs was performed in this work using modified SILAR method. The size of the QDs plays a critical role in light harvesting and charge transfer due to the quantum confinement effect and charge diffusions. The poor control of QDs sensitizations in high aspect ratio nanostructures using conventional methods causes high charge recombination losses. By employing ALD for photosensitization, controlled infiltration thickness and step coverage could be achieved. The size of QDs could be varied simply by designing the number of deposition cycles. In our group, ALD of ZnO thin films were deposited on various high aspect ratio TiO_2 nanostructures as the sacrificial templates to convert to CdSe QDs by ion exchange reaction.[130] The thickness and the size of the sensitizer were controlled by tuning the thickness of the ALD ZnO layer and the condition of ion exchange reaction. Further improvements in this approach are anticipated by developing others short bandgap semiconductor sensitizers based on nanobushes photoanode platform.

References

1. Zhou, Y.; King, D. M.; Li, J.; Barrett, K. S.; Goldfarb, R. B.; Weimer, A. W., Synthesis of Photoactive Magnetic Nanoparticles with Atomic Layer Deposition. *Industrial & Engineering Chemistry Research* **2010,** 49, (15), 6964-6971.

2. Nozik, A. J., Advanced Concepts for Photovoltaic Cells, NCPV and Solar Program Review Meeting Proceedings, National Renewable Energy Laboratory: Golden, 2003, pp 422-426.

3. Bruton, T.; Luthardt, G.; Rasch, K. D.; Roy, K.; Dorrity, I.; Garrard, B.; Teale, L.; Alonso, J.; Ugalde, U.; Declerq, K.; Nijs, J.; Szlufcik, J.; Rauber, A.; Wettling, W.; Vallera, A., A study on the manufacture at 500MWp p.a. of crystalline silicon photovoltaic modules, 14th European Photovoltaic Solar Energy Conference, Barcelona, June/July, 1997; Barcelona, 1997; pp 11-16.

4. Gratzel, M., Photoelectrochemical cells. *Nature* **2001,** 414, (6861), 338-344.

5. Bak, T.; Nowotny, J.; Rekas, M.; Sorrell, C. C., Photo-electrochemical hydrogen generation from water using solar energy. Materials-related aspects. *International Journal of Hydrogen Energy* **2002,** 27, (10), 991-1022.

6. Kamat, P. V.; Tvrdy, K.; Baker, D. R.; Radich, J. G., Beyond photovoltaics: Semiconductor nanoarchitectures for liquid-junction solar cells. *Chemical Reviews* **2010,** 110, (11), 6664-6688.

7. Lin, Y.; Yuan, G.; Liu, R.; Zhou, S.; Sheehan, S. W.; Wang, D., Semiconductor nanostructure-based photoelectrochemical water splitting: A brief review. *Chemical Physics Letters* **2011,** 507, (4-6), 209-215.

8. Zhou, H.; Li, X.; Fan, T.; Osterloh, F. E.; Ding, J.; Sabio, E. M.; Zhang, D.; Guo, Q., Artificial Inorganic Leafs for Efficient Photochemical Hydrogen Production Inspired by Natural Photosynthesis. *Advanced Materials* **2010,** 22, (9), 951-956.

9. George, S. M., Atomic Layer Deposition: An Overview. *Chemical Reviews* **2009,** 110, (1), 111-131.

10. Kamat, P. V., Meeting the clean energy demand: Nanostructure architectures for solar energy conversion. *Journal of Physical Chemistry C* **2007,** 111, (7), 2834-2860.

11. Armaroli, N.; Balzani, V., The future of energy supply: Challenges and opportunities. *Angewandte Chemie - International Edition* **2007,** 46, (1-2), 52-66.

12. Crabtree, G. W.; Dresselhaus, M. S.; Buchanan, M. V., The hydrogen economy. *Physics Today* **2004,** 57, (12), 39-44.

13. Hagfeldt, A.; Boschloo, G.; Sun, L.; Kloo, L.; Pettersson, H., Dye-sensitized solar cells. *Chemical Reviews* **2010,** 110, (11), 6595-6663.

14. Mora-Sera, I.; Bisquert, J., Breakthroughs in the development of semiconductor-sensitized solar cells. *Journal of Physical Chemistry Letters* **2010,** 1, (20), 3046-3052.

15. Bard, A. J., Photoelectrochemistry. *Science* **1980,** 207, (4427), 139-144.

16. O'Regan, B.; Grätzel, M., A low-cost, high-efficiency solar cell based on dye-sensitized colloidal TiO_2 films. *Nature* **1991,** 353, (6346), 737-740.

17. Nishimura, S.; Abrams, N.; Lewis, B. A.; Halaoui, L. I.; Mallouk, T. E.; Benkstein, K. D.; Van de Lagemaat, J.; Frank, A. J., Standing wave enhancement of red absorbance and photocurrent in dye-sensitized titanium dioxide photoelectrodes coupled to photonic crystals. *Journal of the American Chemical Society* **2003,** 125, (20), 6306-6310.

18. Rodriguez, I.; Atienzar, P.; Ramiro-Manzano, F.; Meseguer, F.; Corma, A.; Garcia, H., Photonic crystals for applications in photoelectrochemical processes: Photoelectrochemical solar cells with inverse opal topology. *Photonics and Nanostructures - Fundamentals and Applications* **2005,** 3, (2-3), 148-154.

19. Shockley, W.; Queisser, H. J., Detailed balance limit of efficiency of p-n junction solar cells. *Journal of Applied Physics* **1961,** 32, (3), 510-519.

20. Chang, J. A.; Rhee, J. H.; Im, S. H.; Lee, Y. H.; Kim, H. J.; Seok, S. I.; Nazeeruddin, M. K.; Gratzel, M., High-performance nanostructured inorganic-organic heterojunction solar cells. *Nano Letters* **2010,** 10, (7), 2609-2612.

21. Hossain, M. A.; Jennings, J. R.; Koh, Z. Y.; Wang, Q., Carrier generation and collection in CdS/CdSe-sensitized SnO_2 Solar cells exhibiting unprecedented photocurrent densities. *ACS Nano* **2011,** 5, (4), 3172-3181.

22. Canovas, E.; Moll, P.; Jensen, S. r. A.; Gao, Y.; Houtepen, A. J.; Siebbeles, L. D. A.; Kinge, S.; Bonn, M., Size-Dependent Electron Transfer from PbSe Quantum Dots to SnO_2 Monitored by Picosecond Terahertz Spectroscopy. *Nano Letters* **2011**, DOI: 10.1021/nl202550v.

23. Li, Y.; Zhang, J. Z., Hydrogen generation from photoelectrochemical water splitting based on nanomaterials. *Laser & Photonics Reviews* **2009,** 4, (4), 517-528.

24. Sun, J.; Zhong, D. K.; Gamelin, D. R., Composite photoanodes for photoelectrochemical solar water splitting. *Energy and Environmental Science* **2010,** 3, (9), 1252-1261.

25. Fujishima, A.; Honda, K., Electrochemical photolysis of water at a semiconductor electrode. *Nature* **1972,** 238, (5358), 37-38.

26. Boettcher, S. W.; Spurgeon, J. M.; Putnam, M. C.; Warren, E. L.; Turner-Evans, D. B.; Kelzenberg, M. D.; Maiolo, J. R.; Atwater, H. A.; Lewis, N. S., Energy-Conversion Properties of Vapor-Liquid-Solid-Grown Silicon Wire-Array Photocathodes. *Science* **2010,** 327, (5962), 185-187.

27. Khan, S. U. M.; Al-Shahry, M.; Ingler, W. B., Efficient Photochemical Water Splitting by a Chemically Modified n-TiO_2. *Science* **2002,** 297, (5590), 2243-2245.

28. Walter, M. G.; Warren, E. L.; McKone, J. R.; Boettcher, S. W.; Mi, Q.; Santori, E. A.; Lewis, N. S., Solar Water Splitting Cells. *Chemical Reviews* **2010,** 110, (11), 6446-6473.

29. Maeda, K.; Domen, K., Solid Solution of GaN and ZnO as a Stable Photocatalyst for Overall Water Splitting under Visible Light. *Chemistry of Materials* **2009,** 22, (3), 612-623.

30. Chen, H. M.; Chen, C. K.; Chang, Y. C.; Tsai, C. W.; Liu, R. S.; Hu, S. F.; Chang, W. S.; Chen, K. H., Quantum dot monolayer sensitized ZnO nanowire-array photoelectrodes: True efficiency for water splitting. *Angewandte Chemie - International Edition* **2010,** 49, (34), 5966-5969.

31. Meng, Q. Q.; Wang, J. G.; Xie, Q.; Dong, H. Q.; Li, X. N., Water splitting on TiO_2 nanotube arrays. *Catalysis Today* **2011,** 165, (1), 145-149.

32. Shi, J.; Hara, Y.; Sun, C.; Anderson, M. A.; Wang, X., Three-Dimensional High-Density Hierarchical Nanowire Architecture for High-Performance Photoelectrochemical Electrodes. *Nano Letters* **2011,** 11, (8), 3413-3419.

33. Lee, Y. L.; Chi, C. F.; Liau, S. Y., CdS/CdSe Co-Sensitized TiO_2 photoelectrode for efficient hydrogen generation in a photoelectrochemical cell. *Chemistry of Materials* **2010,** 22, (3), 922-927.

34. Hensel, J.; Wang, G.; Li, Y.; Zhang, J. Z., Synergistic effect of CdSe quantum dot sensitization and nitrogen doping of TiO_2 nanostructures for photoelectrochemical solar hydrogen generation. *Nano Letters* **2010,** 10, (2), 478-483.

35. Wang, G.; Yang, X.; Qian, F.; Zhang, J. Z.; Li, Y., Double-sided CdS and CdSe quantum dot co-sensitized ZnO nanowire arrays for photoelectrochemical hydrogen generation. *Nano Letters* **2010,** 10, (3), 1088-1092.

36. Bang, J. H.; Kamat, P. V., Solar cells by design: Photoelectrochemistry of TiO_2 nanorod arrays decorated with CdSe. *Advanced Functional Materials* **2010,** 20, (12), 1970-1976.

37. Law, M.; Greene, L. E.; Johnson, J. C.; Saykally, R.; Yang, P., Nanowire dye-sensitized solar cells. *Nature Materials* **2005,** 4, (6), 455-459.

38. Xu, C.; Wu, J.; Desai, U. V.; Gao, D., Multilayer Assembly of Nanowire Arrays for Dye-Sensitized Solar Cells. *Journal of the American Chemical Society* **2011,** 133, (21), 8122-8125.

39. Sauvage, F.; Di Fonzo, F.; Li Bassi, A.; Casari, C. S.; Russo, V.; Divitini, G.; Ducati, C.; Bottani, C. E.; Comte, P.; Graetzel, M., Hierarchical TiO2 photoanode for dye-sensitized solar cells. *Nano Letters* **2010,** 10, (7), 2562-2567.

40. Baker, D. R.; Kamat, P. V., Photosensitization of TiO_2 nanostructures with CdS quantum dots: Particulate versus tubular support architectures. *Advanced Functional Materials* **2009,** 19, (5), 805-811.

41. Tvrdy, K.; Frantsuzov, P. A.; Kamat, P. V., Photoinduced electron transfer from semiconductor quantum dots to metal oxide nanoparticles. *Proceedings of the National Academy of Sciences of the United States of America* **2011,** 108, (1), 29-34.

42. Varghese, O. K.; Paulose, M.; Grimes, C. A., Long vertically aligned titania nanotubes on transparent conducting oxide for highly efficient solar cells. *Nature Nanotechnology* **2009,** 4, (9), 592-597.

43. Chen, D.; Huang, F.; Cheng, Y. B.; Caruso, R. A., Mesoporous anatase TiO_2 beads with high surface areas and controllable pore sizes: A superior candidate for high-performance dye-sensitized solar cells. *Advanced Materials* **2009,** 21, (21), 2206-2210.

44. Luo, Y.; Li, D.; Meng, Q., Towards optimization of materials for dye-sensitized solar cells. *Advanced Materials* **2009,** 21, (45), 4647-4651.

45. Zhang, Q.; Chou, T. P.; Russo, B.; Jenekhe, S. A.; Cao, G., Aggregation of ZnO nanocrystallites for high conversion efficiency in dye-sensitized solar cells. *Angewandte Chemie - International Edition* **2008,** 47, (13), 2402-2406.

46. Kwak, E. S.; Lee, W.; Park, N. C.; Kim, J.; Lee, H., Compact inverse-opal electrode using non-aggregated TiO_2 nanoparticles for dye-sensitized solar cells. *Advanced Functional Materials* **2009,** 19, (7), 1093-1099.

47. Liu, L.; Karuturi, S. K.; Su, L. T.; Tok, A. I. Y., TiO_2 inverse-opal electrode fabricated by atomic layer deposition for dye-sensitized solar cell applications. *Energy and Environmental Science* **2011,** 4, (1), 209-215.

48. Guldin, S.; Huttner, S.; Kolle, M.; Welland, M. E.; Muller-Buschbaum, P.; Friend, R. H.; Steiner, U.; Tetreault, N., Dye-sensitized solar cell based on a three-dimensional photonic crystal. *Nano Letters* **2010,** 10, (7), 2303-2309.

49. Diguna, L. J.; Shen, Q.; Kobayashi, J.; Toyoda, T., High efficiency of CdSe quantum-dot-sensitized TiO_2 inverse opal solar cells. *Applied Physics Letters* **2007,** 91, (2).

50. Zhang, L.; Baumanis, C.; Robben, L.; Kandiel, T.; Bahnemann, D., Bi_2WO_6 Inverse Opals: Facile Fabrication and Efficient Visible-Light-Driven Photocatalytic and Photoelectrochemical Water-Splitting Activity. *Small* **2011,** 7, (19), 2714-2720.

51. Tetreault, N.; Arsenault, E.; Heiniger, L.-P.; Soheilnia, N.; Brillet, J.; Moehl, T.; Zakeeruddin, S.; Ozin, G. A.; Gratzel, M., High-Efficiency Dye-Sensitized Solar Cell with Three-Dimensional Photoanode. *Nano Letters* **2011**.

52. Chen, X.; Ye, J.; Ouyang, S.; Kako, T.; Li, Z.; Zou, Z., Enhanced incident photon-to-electron conversion efficiency of tungsten trioxide photoanodes based on 3d-photonic crystal design. *ACS Nano* **2011,** 5, (6), 4310-4318.

53. Yablonovitch, E., Inhibited spontaneous emission in solid-state physics and electronics. *Physical Review Letters* **1987,** 58, (20), 2059-2062.

54. John, S., Strong localization of photons in certain disordered dielectric superlattices. *Physical Review Letters* **1987,** 58, (23), 2486-2489.

55. Busch, K.; von Freymann, G.; Linden, S.; Mingaleev, S. F.; Tkeshelashvili, L.; Wegener, M., Periodic nanostructures for photonics. *Physics Reports* **2007,** 444, (3-6), 101-202.

56. Shin, J.-H.; Moon, J. H., Bilayer Inverse Opal TiO_2 Electrodes for Dye-Sensitized Solar Cells via Post-Treatment. *Langmuir* **2011,** 27, (10), 6311-6315.

57. Seo, Y. G.; Woo, K.; Kim, J.; Lee, H.; Lee, W., Rapid Fabrication of an Inverse Opal TiO_2 Photoelectrode for DSSC Using a Binary Mixture of TiO_2 Nanoparticles and Polymer Microspheres. *Advanced Functional Materials* **2011,** 21, (16), 3094-3103.

58. Park, S. H.; Gates, B.; Xia, Y., Three-dimensional photonic crystal operating in the visible region. *Advanced Materials* **1999,** 11, (6), 462-466.

59. Mihi, A.; Calvos, M. E.; Anta, J. A.; Míguez, H., Spectral response of opal-based dye-sensitized solar cells. *Journal of Physical Chemistry C* **2008,** 112, (1), 13-17.

60. Mihi, A.; Míguez, H., Origin of light-harvesting enhancement in colloidal-photonic-crystal-based dye-sensitized solar cells. *Journal of Physical Chemistry B* **2005,** 109, (33), 15968-15976.

61. Mihi, A.; López-Alcaraz, F. J.; Míguez, H., Full spectrum enhancement of the light harvesting efficiency of dye sensitized solar cells by including colloidal photonic crystal multilayers. *Applied Physics Letters* **2006,** 88, (19).

62. Lee, B.; Hwang, D.-K.; Guo, P.; Ho, S.-T.; Buchholtz, D. B.; Wang, C.-Y.; Chang, R. P. H., Materials, Interfaces, and Photon Confinement in Dye-Sensitized Solar Cells. *The Journal of Physical Chemistry B* **2011,** 114, (45), 14582-14591.

63. Zhang, Y.; Wang, J.; Zhao, Y.; Zhai, J.; Jiang, L.; Song, Y.; Zhu, D., Photonic crystal concentrator for efficient output of dye-sensitized solar cells. *Journal of Materials Chemistry* **2008,** 18, (23), 2650-2652.

64. Chen, X.; Ye, J.; Ouyang, S.; Kako, T.; Li, Z.; Zou, Z., Enhanced Incident Photon-to-Electron Conversion Efficiency of Tungsten Trioxide Photoanodes Based on 3D-Photonic Crystal Design. *ACS Nano* **2011,** 5, (6), 4310–4318.

65. Liu, J.; Liu, G.; Li, M.; Shen, W.; Liu, Z.; Wang, J.; Zhao, J.; Jiang, L.; Song, Y., Enhancement of photochemical hydrogen evolution over Pt-loaded hierarchical titania photonic crystal. *Energy and Environmental Science* **2010,** 3, (10), 1503-1506.

66. Chen, J. I. L.; Von Freymann, G.; Kitaev, V.; Ozin, G. A., Effect of disorder on the optically amplified photocatalytic efficiency of titania inverse opals. *Journal of the American Chemical Society* **2007,** 129, (5), 1196-1202.

67. O'Brien, P. G.; Kherani, N. P.; Zukotynski, S.; Ozin, G. A.; Vekris, E.; Tetreault, N.; Chutinan, A.; John, S.; Mihi, A.; Miguez, H., Enhanced photoconductivity in thin-film semiconductors optically coupled to photonic crystals. *Advanced Materials* **2007,** 19, (23), 4177-4182.

68. Colodrero, S.; Mihi, A.; Anta, J. A.; Ocan, M.; Miguez, H., Experimental demonstration of the mechanism of light harvesting enhancement in Photonic-Crystal-Based Dye-Sensitized solar cells. *Journal of Physical Chemistry C* **2009,** 113, (4), 1150-1154.

69. Lee, S. H. A.; Abrams, N. M.; Hoertz, P. G.; Barber, G. D.; Halaoui, L. I.; Mallouk, T. E., Coupling of titania inverse opals to nanocrystalline titania layers in dye-sensitized solar cells. *Journal of Physical Chemistry B* **2008,** 112, (46), 14415-14421.

70. Calvo, M. E.; Miguez, H., Flexible, adhesive, and biocompatible Bragg mirrors based on polydimethylsiloxane infiltrated nanoparticle multilayers. *Chemistry of Materials* **2010,** 22, (13), 3909-3915.

71. Suntola, T.; Antson, J., Method for Producing Compound Thin Films. *U.S. Patent: 4,058,430* Issued Nov. 25, 1977.

72. Lee, S.-M.; Pippel, E.; Gösele, U.; Dresbach, C.; Qin, Y.; Chandran, C. V.; Bräuniger, T.; Hause, G.; Knez, M., Greatly Increased Toughness of Infiltrated Spider Silk. *Science* **2009,** 324, (5926), 488-492.

73. Zhou, Y.; King, D. M.; Li, J.; Barrett, K. S.; Goldfarb, R. B.; Weimer, A. W., Synthesis of Photoactive Magnetic Nanoparticles with Atomic Layer Deposition. *Industrial & Engineering Chemistry Research* **2010**, 49, (15), 6964-6971.

74. Ras, R. H. A.; Kemell, M.; de Wit, J.; Ritala, M.; ten Brinke, G.; Leskelä, M.; Ikkala, O., Hollow Inorganic Nanospheres and Nanotubes with Tunable Wall Thicknesses by Atomic Layer Deposition on Self-Assembled Polymeric Templates. *Advanced Materials* **2007,** 19, (1), 102-106.

75. Fan, H. J.; Knez, M.; Scholz, R.; Nielsch, K.; Pippel, E.; Hesse, D.; Gosele, U.; Zacharias, M., Single-crystalline $MgAl_2O_4$ spinel nanotubes using a reactive and removable MgO nanowire template. *Nanotechnology* **2006,** 17, (20), 5157-5162.

76. Peng, Q.; Sun, X. Y.; Spagnola, J. C.; Saquing, C.; Khan, S. A.; Spontak, R. J.; Parsons, G. N., Bi-directional Kirkendall Effect in Coaxial Microtuble Nanolaminate Assemblies Fabricated by Atomic Layer Deposition. *Acs Nano* **2009,** 3, (3), 546-554.

77. Qin, Y.; Liu, L. F.; Yang, R. B.; Gosele, U.; Knez, M., General Assembly Method for Linear Metal Nanoparticle Chains Embedded in Nanotubes. *Nano Letters* **2008,** 8, (10), 3221-3225.

78. Fan, H. J.; Yang, Y.; Zacharias, M., ZnO-based ternary compound nanotubes and nanowires. *Journal of Materials Chemistry* **2009,** 19, (7), 885-900.

79. Yang, Y.; Kim, D. S.; Knez, M.; Scholz, R.; Berger, A.; Pippel, E.; Hesse, D.; Gosele, U.; Zacharias, M., Influence of temperature on evolution of coaxial ZnO/Al_2O_3 one-dimensional heterostructures: From core-shell nanowires to spinel nanotubes and porous nanowires. *Journal of Physical Chemistry C* **2008,** 112, (11), 4068-4074.

80. Yang, Y.; Scholz, R.; Fan, H. J.; Hesse, D.; Gosele, U.; Zacharias, M., Multitwinned Spinel Nanowires by Assembly of Nanobricks via Oriented Attachment: A Case Study of Zn_2TiO_4. *ACS Nano* **2009,** 3, (3), 555-562.

81. Yang, Y.; Yang, R. B.; Fan, H. J.; Scholz, R.; Huang, Z. P.; Berger, A.; Qin, Y.; Knez, M.; Gosele, U., Diffusion-Facilitated Fabrication of Gold-Decorated Zn_2SiO_4 Nanotubes by a One-Step Solid-State Reaction. *Angewandte Chemie-International Edition* **2010,** 49, (8), 1442-1446.

82. Fan, H. J.; Gosele, U.; Zacharias, M., Formation of nanotubes and hollow nanoparticles based on Kirkendall and diffusion processes: A review. *Small* **2007,** 3, (10), 1660-1671.

83. Leskela, M.; Kemell, M.; Kukli, K.; Pore, V.; Santala, E.; Ritala, M.; Lu, J., Exploitation of atomic layer deposition for nanostructured materials. *Materials Science and Engineering C* **2007,** 27, (5-8 SPEC. ISS.), 1504-1508.

84. Knez, M.; Nielsch, K.; Niinisto, L., Synthesis and surface engineering of complex nanostructures by atomic layer deposition. *Advanced Materials* **2007,** 19, (21), 3425-3438.

85. Ritala, M.; Leskela, M., Atomic layer epitaxy - a valuable tool for nanotechnology? *Nanotechnology* **1999,** 10, (1), 19-24.

86. Kim, H.; Lee, H. B. R.; Maeng, W. J., Applications of atomic layer deposition to nanofabrication and emerging nanodevices. *Thin Solid Films* **2009,** 517, (8), 2563-2580.

87. Wijnhoven, J. E. G. J.; Vos, W. L., Preparation of photonic crystals made of air spheres in titania. *Science* **1998,** 281, (5378), 802-804.

88. Subramania, G.; Constant, K.; Biswas, R.; Sigalas, M. M.; Ho, K. M., Optical photonic crystals fabricated from colloidal systems. *Applied Physics Letters* **1999,** 74, (26), 3933-3935.

89. Rugge, A.; Park, J. S.; Gordon, R. G.; Tolbert, S. H., Tantalum(V) nitride inverse opals as photonic structures for visible wavelengths. *Journal of Physical Chemistry B* **2005,** 109, (9), 3764-3771.

90. Graugnard, E.; Chawla, V.; Lorang, D.; Summers, C. J., High filling fraction gallium phosphide inverse opals by atomic layer deposition. *Applied Physics Letters* **2006,** 89, (21).

91. King, J. S.; Graugnard, E.; Summers, C. J., TiO_2 Inverse Opals Fabricated Using Low-Temperature Atomic Layer Deposition. *Advanced Materials* **2005,** 17, (8), 1010-1013.

92. Kucheyev, S. O.; Biener, J.; Baumann, T. F.; Wang, Y. M.; Hamza, A. V.; Li, Z.; Lee, D. K.; Gordon, R. G., Mechanisms of atomic layer deposition on substrates with ultrahigh aspect ratios. *Langmuir* **2008,** 24, (3), 943-948.

93. Perez, I.; Robertson, E.; Banerjee, P.; Henn-Lecordier, L.; Son, S. J.; Lee, S. B.; Rubloff, G. W., TEM-based metrology for HfO_2 layers and nanotubes formed in anodic aluminum oxide nanopore structures. *Small* **2008,** 4, (8), 1223-1232.

94. Elam, J. W.; Routkevitch, D.; Mardilovich, P. P.; George, S. M., Conformal coating on ultrahigh-aspect-ratio nanopores of anodic alumina by atomic layer deposition. *Chemistry of Materials* **2003,** 15, (18), 3507-3517.

95. Reijnen, L.; Feddes, B.; Vredenberg, A. M.; Schoonman, J.; Goossens, A., Rutherford backscattering spectroscopy study of TiO_2/$Cu_{1.8}S$ nanocomposites obtained by atomic layer deposition. *Journal of Physical Chemistry B* **2004,** 108, (26), 9133-9137.

96. Andrew, B.; Ying-Chieh, C.; Pierre, W.; Paul V, B., Complex three-dimensional conformal surfaces formed by atomic layer deposition: computation and experimental verification. *Journal of Material Chemistry* **2009**, (19), 9126 - 9130.

97. Berland, B. S.; Gartland, I. P.; Ott, A. W.; George, S. M., In situ monitoring of atomic layer controlled pore reduction in alumina tubular membranes using sequential surface reactions. *Chemistry of Materials* **1998,** 10, (12), 3941-3950.

98. Gordon, R. G.; Hausmann, D.; Kim, E.; Shepard, J., A kinetic model for step coverage by atomic layer deposition in narrow holes or trenches. *Chemical vapor deposition* **2003,** 9, (2), 73-78.

99. Jiang, P.; Bertone, J. F.; Hwang, K. S.; Colvin, V. L., Single-crystal colloidal multilayers of controlled thickness. *Chemistry of Materials* **1999,** 11, (8), 2132-2140.

100. Elam, J. W.; Groner, M. D.; George, S. M., Viscous flow reactor with quartz crystal microbalance for thin film growth by atomic layer deposition. *Review of Scientific Instruments* **2002,** 73, (8), 2981.

101. Aarik, J.; Aidla, A.; Mändar, H.; Uustare, T., Atomic layer deposition of titanium dioxide from $TiCl_4$ and H_2O: Investigation of growth mechanism. *Applied Surface Science* **2001,** 172, (1-2), 148-158.

102. Cheng, C.; Yan, B.; Wong, S. M.; Li, X.; Zhou, W.; Yu, T.; Shen, Z.; Yu, H.; Fan, H. J., Fabrication and SERS performance of silver-nanoparticle-decorated Si/ZnO nanotrees in ordered arrays. *ACS Applied Materials and Interfaces* **2010,** 2, (7), 1824-1828.

103. Karuturi, S. K.; Liu, L.; Su, L. T.; Zhao, Y.; Fan, H. J.; Ge, X.; He, S.; Yoong, A. T. I., Kinetics of Stop-Flow Atomic Layer Deposition for High Aspect Ratio Template Filling through Photonic Band Gap Measurements. *The Journal of Physical Chemistry C* **2010,** 114, (35), 14843-14848.

104. Sundaram, G. M.; Deguns, E. W.; Bhatia, R.; Dalberth, M. J.; Sowa, M. J.; Becker, J. S., Thin films for 3D: ALD for non-planar topographies. *Solid State Technology* **2009,** 52, (6), 14-17.

105. Hausmann, D. M.; Kim, E.; Becker, J.; Gordon, R. G., Atomic layer deposition of hafnium and zirconium oxides using metal amide precursors. *Chemistry of Materials* **2002,** 14, (10), 4350-4358.

106. Norris, D. J.; Arlinghaus, E. G.; Meng, L.; Heiny, R.; Scriven, L. E., Opaline photonic crystals: How does self-assembly work?. *Advanced Materials* **2004,** 16, (16).

107. Newton, M. R.; Morey, K. A.; Zhang, Y.; Snow, R. J.; Diwekar, M.; Shi, J.; White, H. S., Anisotropic diffusion in face-centered cubic opals. *Nano Letters* **2004,** 4, (5), 875-880.

108. Knez, M.; Kadri, A.; Wege, C.; Gösele, U.; Jeske, H.; Nielsch, K., Atomic layer deposition on biological macromolecules: Metal oxide coating of tobacco mosaic virus and ferritin. *Nano Letters* **2006,** 6, (6), 1172-1177.

109. King, J. S.; Graugnard, E.; Roche, O. M.; Sharp, D. N.; Scrimgeour, J.; Denning, R. G.; Turberfield, A. J.; Summers, C. J., Infiltration and inversion of holographically defined polymer photonic crystal templates by atomic layer deposition. *Advanced Materials* **2006,** 18, (12), 1561-1565.

110. Cheng, C.; Karuturi, S. K.; Liu, L.; Liu, J.; Li, H.; Su, L. T.; Tok, A. I. Y.; Fan, H. J., Quantum-Dot-Sensitized TiO_2 Inverse Opals for Photoelectrochemical Hydrogen Generation. *Small* **2011**, 10.1002/smll.201101660

111. Nozik, A. J., Nanoscience and Nanostructures for Photovoltaics and Solar Fuels. *Nano Letters* **2010,** 10, (8), 2735-2741.

112. Stein, A.; Li, F.; Denny, N. R., Morphological Control in Colloidal Crystal Templating of Inverse Opals, Hierarchical Structures, and Shaped Particles. *Chemistry of Materials* **2007,** 20, (3), 649-666.

113. Nishimura, S.; Shishido, A.; Abrams, N.; Mallouk, T. E., Fabrication technique for filling-factor tunable titanium dioxide colloidal crystal replicas. *Applied Physics Letters* **2002,** 81, (24), 4532-4534.

114. Karuturi, S. K.; Cheng, C.; Liu, L.; Tat Su, L.; Fan, H. J.; Tok, A. I. Y., Inverse opals coupled with nanowires as photoelectrochemical anode. *Nano Energy* **2012,** 1, (2), 322-327.

115. Lee, B.; Hwang, D.-K.; Guo, P.; Ho, S.-T.; Buchholtz, D. B.; Wang, C.-Y.; Chang, R. P. H., Materials, Interfaces, and Photon Confinement in Dye-Sensitized Solar Cells. *The Journal of Physical Chemistry B* **2011,** 114, (45), 14582-14591.

116. Mihi, A.; Zhang, C.; Braun, P. V., Transfer of Preformed Three-Dimensional Photonic Crystals onto Dye-Sensitized Solar Cells. *Angewandte Chemie International Edition* **2011,** 50, (25), 5712-5715.

117. Karuturi, S. K.; Liu, L.; Su, L. T.; Zhao, Y.; Fan, H. J.; Ge, X.; He, S.; Yoong, A. T. I., Kinetics of stop-flow atomic layer deposition for high aspect ratio template filling through photonic band gap measurements. *Journal of Physical Chemistry C* **2010,** 114, (35), 14843-14848.

118. John, S.; Busch, K., Photonic Bandgap Formation and Tunability in Certain Self-Organizing Systems. *Journal of Lightwave Technology* **1999,** 17, (11), 1931.

119. Cheng, C. W.; Tay, Y. Y.; Hng, H. H.; Fan, H. J., Solution heteroepitaxial growth of dendritic SnO_2/TiO_2 hybrid nanowires. *Journal of Materials Research* **2011,** 26, (17), 2254-2260.

120. Karuturi, S. K.; Luo, J.; Cheng, C.; Liu, L.; Su, L. T.; Tok, A. I. Y.; Fan, H. J., A Novel Photoanode with Three-Dimensionally, Hierarchically Ordered Nanobushes for

Highly Efficient Photoelectrochemical Cells. *Advanced Materials* **2012,** 24, (30), 4157-4162.

121. Marlow, F.; Muldarisnur; Sharifi, P.; Brinkmann, R.; Mendive, C., Opals: Status and prospects. *Angewandte Chemie - International Edition* **2009,** 48, (34), 6212-6233.

122. Xu, C.; Shin, P.; Cao, L.; Gao, D., Preferential growth of long ZnO nanowire array and its application in dye-sensitized solar cells. *Journal of Physical Chemistry C* **2010,** 114, (1), 125-129.

123. Lodahl, P.; Van Driel, A. F.; Nikolaev, I. S.; Irman, A.; Overgaag, K.; Vanmaekelbergh, D.; Vos, W. L., Controlling the dynamics of spontaneous emission from quantum dots by photonic crystals. *Nature* **2004,** 430, (7000), 654-657.

124. Vanmaekelbergh, D.; Van Vugt, L. K., ZnO nanowire lasers. *Nanoscale* **2011,** 3, (7), 2783-2800.

125. Zhang, Q.; Chou, T. P.; Russo, B.; Jenekhe, S. A.; Cao, G., Polydisperse aggregates of ZnO nanocrystallites: A method for energy-conversion-efficiency enhancement in dye-sensitized solar cells. *Advanced Functional Materials* **2008,** 18, (11), 1654-1660.

126. Neale, N. R.; Lee, B. G.; Kang, S. H.; Frank, A. J., Near-infrared light trapping in disordered inverse opals. *Journal of Physical Chemistry C* **2011,** 115, (29), 14341-14346.

127. Galisteo-Lopez, J. F.; Palacios-Lidon, E.; Castillo-Martinez, E.; Lopez, C., Optical study of the pseudogap in thickness and orientation controlled artificial opals. *Physical Review B - Condensed Matter and Materials Physics* **2003,** 68, (11), 1151091-1151098.

128. Palomares, E.; Clifford, J. N.; Haque, S. A.; Lutz, T.; Durrant, J. R., Control of charge recombination dynamics in dye sensitized solar cells by the use of conformally deposited metal oxide blocking layers. *Journal of the American Chemical Society* **2003,** 125, (2), 475-482.

129. Chen, C.; Xie, Y.; Ali, G.; Yoo, S. H.; Cho, S. O., Improved conversion efficiency of CdS quantum dots-sensitized TiO_2 nanotube array using ZnO energy barrier layer. *Nanotechnology* **2011,** 22, (1), 015202.

130. Luo, J.; Karuturi, S. K.; Liu, L.; Su, L. T.; Tok, A. I. Y.; Fan, H. J., Homogeneous Photosensitization of Complex TiO_2 Nanostructures for Efficient Solar Energy Conversion. *Scientific Reports* **2012,** 2.

Appendix

A1 Surface Area Approximations

The following rough estimates compare the internal surface areas of different photoanodes.

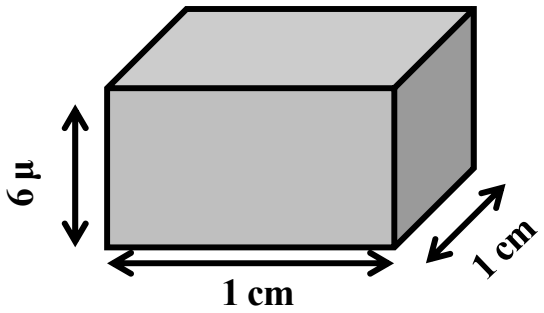

Figure A1. *Schematic of the confinement cell.*

1. **Inverse Opals**

   Volume of confinement cell of 1×1 cm^2 substrate area, $V_{cell} = 6 \times 10^{-3}$ cm $\times$ 1 cm $\times$ 1 cm $= 6 \times 10^{-3}$ cm^3

   Radius of the spherical particles in the present case, $R_{sphere} = 250$ nm $= 250 \times 10^{-6}$ cm

   For FCC structure, opals occupy 74% of the volume.

   Number of spherical particles in the confinement cell $= 0.74 \, . V_{cell} / V_{particle} = 0.74 \times 6 \times 10^{-3} / (4/3 \times \pi \times (R_{sphere})^3)$

   Total surface area = Number of spherical particles in the confinement cell $\times$ Surface area of each particle

$= 0.74 \times 6 \times 10^{-3}\ cm^3 / (4/3 \times \pi \times (R_{sphere})^3) \times (4 \times \pi \times (R_{sphere})^2)$

$= 53.28\ cm^2/cm^2$ of planar substrate

2. Nanobushes

Radius and length of ZnO nanowires in nanobushes are R_{NW} = 10 nm, L_{NW} = 200 nm

Based on FCC structure, void volume of inverse opal is 74% of the cell volume = $0.74 . V_{cell}$

Assuming 50% of the void volume is occupied by nanowires, so number of ZnO nanowires in the confinement cell = $0.5 \times 0.74 \times V_{cell} / V_{NW} = 0.5 \times 0.74 \times 6 \times 10^{-3} / (\pi \times (R_{NW})^2 \times L_{NW})$

Additional surface area created by nanowires growth = Number of nanowires in the confinement cell × Surface area of each nanowire

$= 0.5 \times 0.74 \times 6 \times 10^{-3} / (\pi \times (R_{NW})^2 \times L_{NW}) \times (2 \times \pi \times R_{NW} \times L_{NW})$

$= 444\ cm^2/cm^2$ of planar substrate

3. Nanowires

Radius and length of ZnO nanowires in the nanowires are R_{NW} = 150 nm, L_{NW} = 6 μm

Assuming 50% of the cell volume is occupied by nanowires,

Number of ZnO nanowires in the confinement cell = $0.5 \times V_{cell} / V_{NW} = 0.5 \times 6 \times 10^{-3} / (\pi \times (R_{NW})^2 \times L_{NW})$

Total surface area of nanowires = Number of nanowires in the confinement cell × Surface area of each nanowire

$$= 0.5 \times 6 \times 10^{-3} / (\pi \times (R_{NW})^2 \times L_{NW}) \times (2 \times \pi \times R_{NW} \times L_{NW})$$

$= 40\ cm^2/cm^2$ of planar substrate

A2 Crystal structure comparison with the data base from ICSD

1. TiO_2 Inverse Opal

```
*data for    ICSD #172916
CopyRight    Š2012 by Fachinformationszentrum Karlsruhe, and the U.S. Secretary of
             Commerce on behalf of the United States.  All rights reserved.
Coll Code    172916
Rec  Date    2008/02/01
Chem Name    Titanium Oxide
Structured   Ti O2
Sum          O2 Ti1
ANX          AX2
Min Name     Anatase
D(calc)      3.89
Title        Structural characterization of the hollandite host lattice for the
             confinement of radioactive cesium: Quantification of the amorphous
             phase taking into account the incommensurate modulated character of
             the crystallized part
Author(s)    Leinekugel-le-Cocq-Errien, A.Y.;Deniard, P.;Jobic, S.;Gautier,
             E.;Evain, M.;Aubin, V.;Bart, F.
Reference    Journal of Solid State Chemistry
             (2007), 180(1), 322-330
Unit Cell    3.78500(7) 3.78500(7) 9.5133(2) 90. 90. 90.
Vol          136.28
Z            4
Space Group  I 41/a m d Z
SG Number    141
Cryst Sys    tetragonal
Pearson      tI12
Wyckoff      e b
R Value      0.0869
Red Cell     I  3.785 3.785 5.457 110.288 110.288 89.999 68.145
Trans Red    1.000 0.000 0.000 / 0.000 -1.000 0.000 / -0.500 0.500 -0.500
Comments     Hollandite/anatase mixture with 47.2 % hollandite, for
             hollandite phase see coll-code=172915
             Hollandite synthesized by dry route
             Compound with mineral name: Anatase
             Rietveld profile refinement applied
             Temperature in Kelvin: 293
             Temperature factors available
             Structure type : TiO2(tI12)
             X-ray diffraction (powder)
Atom  #   OX   SITE      x           y           z           SOF      H        ITF(U)
 Ti   1  +4    4 b   0           0.25        0.375       1.         0           .007
 O    1  -2    8 e   0           0.25        0.1663(3)   1.         0           .013
Std. Notes   Transformation Method: Tidy
Std. Cell    3.7850 3.7850 9.5133 90 90 90 136.29
Std. Vol.    136.29
Std. Z       4
Std. SG      I41/AMDZ
Std. Atom
Atom  #   OX   SITE      x           y           z           SOF
 Ti   1  +4    4 b   0           .25         .375        1.
 O    1  -2    8 e   0           .25         .16630      1.
*end for     ICSD #172916
```

2. ZnO Nanowires

```
*data for   ICSD #154486
CopyRight   Š2012 by Fachinformationszentrum Karlsruhe, and the U.S. Secretary of
            Commerce on behalf of the United States.  All rights reserved.
Coll Code   154486
Rec  Date   2007/04/01
Chem Name   Zinc Oxide - Lp
Structured  Zn O
Sum         O1 Zn1
ANX         AX
Min Name    Zincite
D(calc)     5.68
Title       High-pressure X-ray investigation of zincite Zn O single crystals
            using diamond anvils with an improved shape
Author(s)   Sowa, H.;Ahsbahs, H.
Reference   Journal of Applied Crystallography
            (2006), 39, 169-175
Unit Cell   3.2494(2) 3.2494(2) 5.2054(2) 90. 90. 120.
Vol         47.6
Z           2
Space Group P 63 m c
SG Number   186
Cryst Sys   hexagonal
Pearson     hP4
Wyckoff     b2
R Value     0.0149
Red Cell    P  3.249 3.249 5.205 90 90 120 47.598
Trans Red   1.000 0.000 0.000 / 0.000 1.000 0.000 / 0.000 0.000 1.000
Comments    Compound with mineral name: Zincite
            Temperature factors available
            Structure type : ZnS(2H)
            X-ray diffraction from single crystal
Atom  #   OX   SITE      x           y           z           SOF      H
 Zn   1  +2    2 b   0.3333      0.6667      0             1.         0
 O    1  -2    2 b   0.3333      0.6667      0.382(1)      1.         0
Lbl  Type      U11         U22         U33         U12         U13         U23
Zn1  Zn2+  0.0068(4)   0.0068(4)   0.0061(4)   0.0034(2)   0.0000      0.0000
O1   O2-   0.007(2)    0.007(2)    0.008(2)    0.0035(10)  0.0000      0.0000
Std. Notes  Transformation Method: Tidy
Std. Cell   3.2494 3.2494 5.2054 90 90 120 47.6
Std. Vol.   47.6
Std. Z      2
Std. SG     P63MC
Std. Atom
Atom  #   OX   SITE      x           y           z           SOF
 Zn   1  +2    2 b   .33333      .66667      .00000        1.
 O    1  -2    2 b   .33333      .66667      .38200        1.
*end for    ICSD #154486
```

3. CdS Quantum Dots

```
*data for    ICSD #154188
CopyRight    Ś2012 by Fachinformationszentrum Karlsruhe, and the U.S. Secretary of
             Commerce on behalf of the United States.  All rights reserved.
Coll Code    154188
Rec  Date    2007/04/01
Chem Name    Cadmium Sulfide
Structured   Cd S
Sum          Cd1 S1
ANX          AX
D(calc)      4.99
Title        On the mechanism of the pressure-induced wurtzite- to (Na Cl)-type
             phase transition in Cd S : an X-ray diffraction study
Author(s)    Sowa, H.
Reference    Solid State Sciences
             (2005), 7, 73-78
Unit Cell    4.0907(4) 4.0907(4) 6.6411(4) 90. 90. 120.
Vol          96.24
Z            2
Space Group  P 63 m c
SG Number    186
Cryst Sys    hexagonal
Pearson      hP4
Wyckoff      b2
R Value      0.0175
Red Cell     P  4.090 4.090 6.641 90 90 120 96.242
Trans Red    1.000 0.000 0.000 / 0.000 1.000 0.000 / 0.000 0.000 1.000
Comments     Lattice constants at 2280 MPa: 4.0893(3),6.6407(4); at 2580
             MPa: 4.0838(9), 6.6314(10)
             There is a transition to a NaCl-type structure at around
             2500 MPa
             Pressure in MPa: 2290
             Temperature factors available
             Structure type : ZnS(2H)
             X-ray diffraction from single crystal
Atom  #   OX   SITE      x           y           z           SOF      H
 Cd   1  +2    2 b   0.3333      0.6667      0             1.         0
 S    1  -2    2 b   0.3333      0.6667      0.3770(2)     1.         0
Lbl  Type      U11          U22          U33          U12          U13          U23
Cd1  Cd2+  0.0184(2)   0.0184(2)   0.0190(2)   0.0092(1)   0.0000      0.0000
S1   S2-   0.0150(6)   0.0150(6)   0.0143(6)   0.0075(3)   0.0000      0.0000
Std. Notes   Transformation Method: Tidy
Std. Cell    4.0907 4.0907 6.6411 90 90 120 96.24
Std. Vol.    96.24
Std. Z       2
Std. SG      P63MC
Std. Atom
Atom  #   OX   SITE      x           y           z           SOF
 Cd   1  +2    2 b    .33333      .66667      .00000        1.
 S    1  -2    2 b    .33333      .66667      .37700        1.
*end for     ICSD #154188
```